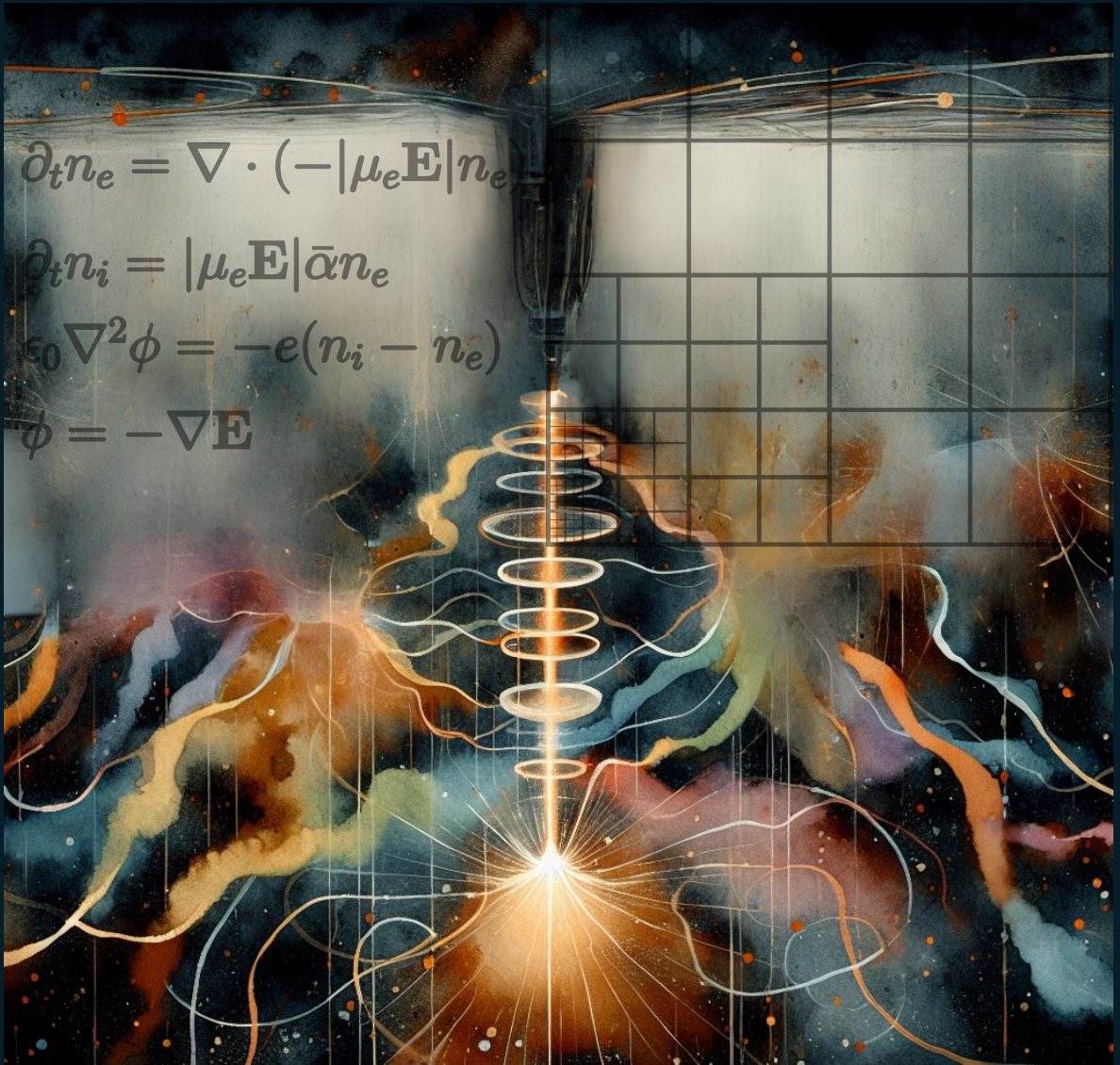


STREAMER DISCHARGE SIMULATIONS: REPETITIVE PULSES, REACTION DATA, AND RADIO EMISSIONS



HEMADITYA MALLA

Streamer discharge simulations: Repetitive Pulses, Reaction Sets, and Radio Emissions

PROEFSCHRIFT

ter verkrijging van de graad van doctor aan de Technische Universiteit Eindhoven, op gezag van de rector magnificus, prof.dr. S. K. Lenaerts, voor een commissie aangewezen door het College voor Promoties, in het openbaar te verdedigen op donderdag 13 Juni 2023 om 16:00 uur

door

Hemaditya Malla

geboren te Visakhapatnam, India

Dit proefschrift is goedgekeurd door de promotoren en de samenstelling van de promotiecommissie is als volgt:

Voorzitter: prof.dr.ir. R. Tuinier

Promotor: prof.dr. U. M. Ebert

Copromotor: dr. H. J. Teunissen (Centrum Wiskunde & Informatica)

Leden: dr.ir. J. van Dijk

prof.dr.ir. G. M. W. Kroesen

prof.dr.ir. G. J. van Rooij (Universiteit Maastricht)

prof.dr. O. Scholten (Rijksuniversiteit Groningen)

Het onderzoek of ontwerp dat in dit proefschrift wordt beschreven is uitgevoerd in overeenstemming met de TU/e Gedragscode Wetenschapsbeoefening.



Centrum Wiskunde & Informatica

The research in this thesis was conducted at Centrum Wiskunde & Informatica (CWI) in Amsterdam, which is the national research institute for mathematics and computer science in the Netherlands.

This research was funded by the NWO project no. 17183 ‘Plasma for Plants’ and the STW project no. 15052 ‘Let CO₂ Spark!’.

This thesis was typeset using L^AT_EX.

The cover was designed by the author with the help of generative AI. It is a watercolor image remotely resembling a streamer simulation with the equations typically used to simulate streamers in the background.

Printed by: Ipskamp Printing

ISBN: 978-94-6473-508-6

Copyright © 2024 Hemaditya Malla
All rights reserved.

Acknowledgements

Here I express my love and gratitude to all the people who have supported me during my PhD journey.

First and foremost, I would like to thank my supervisors Ute Ebert and Jannis Teunissen for giving me the opportunity, guiding me, and finally, helping me finish this thesis. Ute, thank you very much giving me the freedom to pursue topics that interested me. I always left our discussions having learnt something new. Jannis, I am really thankful to have had an amazing supervisor such as you. You were quite patient with me whenever I had difficulties, and always had the time to brainstorm different ideas. I will cherish the co-coding and writing sessions we had. I was able to learn a lot about doing computational research from you. We will surely stay in touch!

To the Multiscale Dynamics group members (and former members): Andy, Dennis, Hani, Baohong, Xiaoran, Ajay, Andong, Zhen, Bas, Rakesh, Carl, Alejandro, and Behnaz, thank you all for making my PhD journey really memorable. Special thanks to my office-mate Dennis for all the trips to the ‘better’ library coffee and all the fun times we’ve had during the many conferences we’d attended together. Thank you very much, Andy, for being the initial guide at the start of my PhD journey.

I would like to thank the support staff at CWI: Nada, Duda, Minne, Bikkie, Remco, Irma, and Karima for making life at CWI much easier.

I would also like to thank the (former) members of the Scientific Computing group: Benjamin, Jurriaan, Laurent, Ki Wai, Sangeetika, Prashant, Beatrice, Daan, Luis, Nikolaj, Syver, and Henrik. I appreciate the interactions we’ve had during my master’s thesis project and PhD. Special thanks to Barry Koren and Benjamin Sanderse for giving me the opportunity to pursue my master’s thesis at CWI without which I would not have been able to pursue this PhD.

I was happy have been a part of the PhD activity committee: Mark, Mathé, Isabella, Ruben, Muriel, Arjan, Vlad(yslav), Sanne, Sebastian, Max(imillian). I have fond memories of organizing fun events with you guys!

Mathé, Nikolaj and Robin M., we were the only few people to get permission to work at CWI during the Covid lockdowns. It was a difficult time for all of us, but I really appreciated your company at CWI during those days. Mathé, thank you for all chats, the Overcooked gaming sessions and the special hamburger

lunches from the CWI canteen. Nikolaj, thank you for the coffee conversations about the various audiobooks each of us was listening to at that time. Robin M., I cherish our evening walks, the sport sessions at the USC, and Ultimate frisbee training sessions.

The *three Muskeaters* gang: Subha and Mande, we met and became good friends towards the end of my PhD. Our cooking and comedy sessions after a long day at work never ceased to help me unwind.

To all my friends in Amsterdam: Daniel, Robin F., Vasoula, Matteo, Sanjeev, Maureen and the rest of the gang, my team the at Amsterdam Ultimate Club, Lori, Rowdy, Robin M., Wilhelm, Mamta, Kenia, and Tarteel, thank you for all the support. I could not have done it without you guys.

Tobias, our friendship started in Singapore in 2016 and is continuing till this day. thank you for helping me adjust to my new life in the Netherlands and being my sports buddy. Our swim sessions, bike rides and other sport sessions consistently motivated me to stay fit despite the stress during the past four years.

To the *BITS Boys*: An(-urad)iruddh , Sir John, Kushal, Amrut, Regy, Shar(dewl), Siddhant (Chacha), Vamsi and George, thank you for everything. I really appreciate how we all supported each other during the past four years. Aniruddh, I enjoyed our daily morning phonecall rants/discussions.

Sanath, Anmol Monica, Bini, and Prafful, thane you being my really close friends since 2016. Sanath, my dude, its amazing how similar our PhD experiences are, and that gave me the courage to hang in there since I knew I was not alone!

Special thanks to Dr. Rajarm Lakkaraju, Dr. Shibu Clement who gave me various opportunities and laid the groundwork for my journey into computational sciences.

To the *Cartoon Network* gang: Hanut, Mango, Sanki, Vijay and Vishnu. thank you for being a part of my life since high school! The long phone calls and the quirky rants were a source of energy for me during my PhD struggles.

Special thanks to Patel 'sir', it was your physics lectures that have put me on the path I am on today.

To Maura, my sweet girlfriend. thank you for all the support during the last phase of my PhD journey.

I would like to thank all my family members (too many to be named here) for the constant patience and support they have shown me throughout this journey. Finally, my parents and little brother, Uma, Gayatri and Sashi, thank you for being there for me all throughout this journey. Mum and dad, without your hard work and many sacrifices, I would not have been able to achieve any of this. Dad, I can say that you worked harder than me to get me to where I am today. Thank you very much for always taking the time to talk to me despite your busy schedules.

Hemaditya Malla, Amsterdam, June 2024

Summary

In this work, we look at a specific type of electrical discharge called streamer discharges (or streamers). They usually occur as precursors to other discharges or as sprites in the earth's upper atmosphere. Streamer discharges are composed of numerous thin, finger-like channels that propagate leaving a trail of ionized gas in their wake. We study them in order to better understand our upper atmosphere, and to develop eco-friendly industrial technologies like, efficient combustion engines, and non-polluting agricultural fertilizers. We commonly study them as low-temperature plasmas since they are composed of ionized and energetic molecules and the 'average' temperature is relatively low. In this thesis, the focus is on three topics related to streamers: 1) their physics under repetitive pulses, 2) the sensitivity of simulated streamer properties to input reaction sets, and 3) estimation of their radio frequency emissions. We study these topics in the simplified setting of the simulation of a single streamer.

Repetitive voltage sources with identical pulse shapes are commonly used to generate streamers or streamer-like discharges in laboratory and industrial settings. Such sources have the advantage that they prevent the transition to a hotter discharge and minimize energy consumption. Repetition frequency of the voltage source affects the energy deposition rate and the composition of ionized and excited molecules and hence, it is an important control parameter. As a first step, we perform double-pulse simulations to study how the second-pulse streamer discharge is affected by the first pulse. We found that electron density inside the streamer channel depends on the waiting time between the two pulses, which in turn affected the second-pulse streamer behavior. We also identified certain chemical reactions (specifically, electron detachment reactions) that are necessary for maintaining streamer channel conductivity for timescales longer than 100 ns. Next, we extend our simulations to multiple pulses (> 2) coupled with gas dynamics in order to study how repetitively pulsed streamers increased the gas temperature and caused an airflow. We found that depending on the applied voltage and the pulse-repetition frequency the gas is heated to different temperatures. We try to relate the change in the gas temperature to the change in streamer physical and chemical properties.

When studying streamer-like discharges in the context of plasma medicine or plasma agriculture applications, we need to take into account the effect water

vapor in air has on streamers. In order to perform streamer simulations, we need relevant humid air input data. However, there is quite some uncertainty in such input data available in literature. Hence, we study the sensitivity of such simulations to the choice of input data, focusing on positive streamers in air close to standard temperature and pressure and at different humidity levels. We first consider different H₂O cross-section data and determine their effect on electron transport coefficients and streamer properties. Next, we investigate the effect of humidity on photoionization by comparing two humid-air photoionization models proposed in literature. Finally, we study how the use of different chemical reaction sets affects streamer properties. Three reaction sets from the literature are used, and a sensitivity analysis is performed to identify important reaction processes. We observed that reaction sets that differ in these reactions, especially electron-ion recombination reactions with positive-ion water clusters give rise to different streamer properties.

Lightning in our upper atmosphere is typically studied by measuring the resulting radio emissions using radio telescopes (e.g., LOFAR telescope in the north of the Netherlands). However, such measurements of positive streamers are not fully understood. We here study radio emissions from positive streamers in air using three-dimensional simulations. To this end, we developed an open-source code that can be used to compute the radiated electric field and its frequency due to a moving space-charge distribution. We consider cases of single streamers with different photoionization methods, streamer branching, streamers interacting with preionization and streamer-streamer encounters. Some of these are commonly occurring cases during lightning storms. We observed that the stochastic fluctuations in streamer propagation due to stochastic photoionization led to emission frequencies of 100 MHz and above. There was no strong VHF radio signal during or after branching, indicating that the current inside a streamer discharge evolves approximately continuously during branching. Another process that leads to such high-frequency emission is the interaction of a streamer with a weakly preionized region, for example present due to a previous discharge. We observed the strongest and highest-frequency emission from streamer encounters, which is in agreement with previous works.

Contents

Acknowledgements	v
Summary	vii
1 Introduction	1
1.1 Motivation to study electrical gas discharges	2
1.2 Microscale physics	3
1.3 Streamer discharges	4
1.4 Introduction to the computational model	7
1.4.1 Model equations	7
1.4.2 Domain and boundary conditions	9
1.4.3 Computational algorithms	9
1.5 Research questions	12
2 Double pulse streamer simulations with varying interpulse times in air	15
2.1 Introduction	17
2.2 Model	18
2.2.1 Equations	18
2.2.2 Geometry	19
2.2.3 Voltage waveform and initial conditions	19
2.2.4 Reaction Set	20
2.3 Results	21
2.3.1 Effect of interpulse time on streamer continuation	21
2.3.2 Channel evolution between pulses	25
2.4 Discussion	26
2.4.1 Comparison with earlier experimental work	26
2.4.2 Criterion for streamer continuation	28
2.4.3 Role of detachment reactions	30
2.4.4 Effect of using a different chemistry set	31
2.5 Conclusions	32
2.6 Outlook	33
2.7 Appendix	33

2.7.1	Effect of varying O ₂ concentration on detachment reactions	33
2.7.2	Electric field inside the streamer channel during the inter-pulse	33
2.7.3	Effect of gas heating	35
3	Streamer discharge simulations in humid air: uncertainty in input data and sensitivity analysis	37
3.1	Introduction	39
3.2	Simulation model	40
3.2.1	Equations	41
3.2.2	Computational domain and initial conditions	41
3.2.3	Electron-neutral cross sections for N ₂ , O ₂ and H ₂ O	42
3.2.4	Photoionization	45
3.2.5	Chemical reactions	48
3.2.6	Sensitivity tests	50
3.3	Simulation results	51
3.3.1	Effect of H ₂ O cross sections	51
3.3.2	Effect of the photoionization model	54
3.3.3	Effect of chemical reactions	54
3.3.4	Sensitivity analysis of chemical reactions	56
3.4	Conclusions	59
3.5	Appendix	63
3.5.1	Effect of ionization reactions	63
3.5.2	Three chemistry sets for humid air	65
4	Effect of gas heating on repetitively pulsed streamer discharges	77
4.1	Introduction	79
4.2	Model	80
4.2.1	Streamer model	80
4.2.2	Neutral gas model	80
4.2.3	Geometry	83
4.2.4	Voltage waveform and initial conditions	83
4.2.5	Reaction set	84
4.3	Results and discussion	84
4.3.1	Main result	84
4.3.2	Effect of varying repetition frequency	85
4.3.3	Effect of applied voltage	89
4.3.4	Effect of slow heating relaxation time	90
4.3.5	Estimate for temperature increase	93
4.4	Conclusions & outlook	94
4.5	Appendix	95
4.5.1	Reaction set used in this chapter	95

5	Calculating radio emissions of positive streamer phenomena using 3D simulations	97
5.1	Introduction	99
5.2	Simulation method	101
5.2.1	Model	101
5.2.2	Computational domain	102
5.2.3	Initial conditions	102
5.2.4	Calculating the radiated electric field	103
5.2.5	Time-frequency analysis procedure	105
5.3	Results	105
5.3.1	Single streamer propagation	105
5.3.2	Double-headed streamer in a higher background field	110
5.3.3	Branching streamer with stochastic photoionization	111
5.3.4	Interaction with ionized patches	113
5.3.5	Streamer collision	114
5.3.6	Radiated energy	118
5.4	Conclusions	118
5.5	Appendix	120
5.5.1	Experimental results on possible radio emission from streamer branching	120
5.5.2	Numerically solving Jefimenko's equations on an AMR grid	123
5.6	The far field approximation for electromagnetic waves	125
6	Conclusions and outlook	127
6.1	Summary and conclusions	127
6.2	Outlook	128
	Bibliography	131
	Curriculum Vitae	145

Chapter 1

Introduction

Metals like iron or copper are generally good electrical conductors, whereas gases are not. This is why it is usually safe to stand under overhead power transmission lines. However, large electric currents can pass through gases under certain conditions, think for example of lightning during thunderstorms. Such phenomena, in which the electric conductivity of the gas suddenly increases are referred to as electric discharges in gases. Depending on the electric field, properties of the gas and its environmental conditions, different types of gas discharges can occur, see figure 1.1. These discharges contain free electrons, ions and excited atoms or molecules, and they are studied in the context of plasma physics [1–3]. In this thesis, the focus is on *streamer discharges*, which is a specific type of gas discharge discussed further.

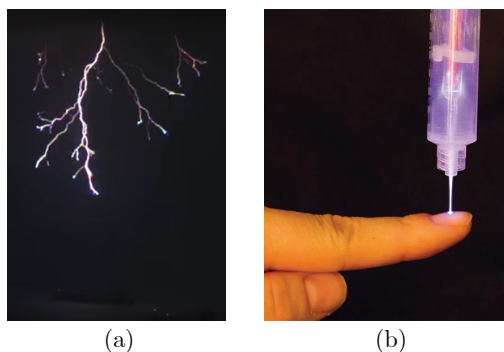


Figure 1.1: Examples of electrical discharges: (a) a snapshot of lightning traveling from cloud to ground [4], (b) a ‘cold’ discharge impinging on a human finger nail. Note that the former discharge can harm humans while the latter is typically harmless and can in fact have disinfecting properties [5].

1.1 Motivation to study electrical gas discharges

We study naturally occurring lightning in our earth's atmosphere not just out of scientific curiosity or to protect ourselves from lightning strikes, but also to gain a better understanding of our upper atmosphere [6]. Additionally, gas discharges find various industrial uses. Certain gas discharges that can be produced and sustained at room temperature are called low temperature plasmas (LTPs). Such discharges have a non-equilibrium nature, i.e., despite being at room temperature, they produce electrons whose temperatures are orders of magnitude greater than room temperature. These energetic electrons collide with neutral gas particles and trigger different chemical reactions that have industrial applications, a few of which are listed below.

- **High-voltage electrical switchgear:** SF₆ (sulphur hexafluoride) gas is still much used to suppress unwanted discharges in high voltage industrial switches. However, SF₆ is really bad for the environment [7, 8] in terms of its global warming potential. Research is being performed into investigating the electrical breakdown properties of other gases like CO₂ or perfluoronitriles like C₄F₇N as eco-friendly alternatives to SF₆ [9–12].
- **Plasma assisted combustion:** As will be illustrated later in this chapter, during a gas discharge different types of chemical processes occur. Discharges can for example be used to dissociate molecules or to excite molecules or atoms to particular states. These excited or dissociated species tend to be more reactive towards hydrocarbon molecules than non-excited ones. Gas discharges in air-fuel mixtures are therefore investigated with the goal of making combustion more efficient [13–16].
- **Biological applications:** Various chemicals like O₃ (ozone), O (atomic oxygen), NO_x (nitrous oxides), H₂O₂ (hydrogen peroxide) can be produced during a gas discharge. These chemicals for example find applications in bio-medical applications as disinfectants, they can kill cancerous cells [17–20], and they can be used as fertilizer replacements or to accelerate seed germination [21–23].
- **Aerospace applications:** Gas discharges heat the gas in which they occur, which leads to gas expansion and motion. This property of certain discharges can be used to control air flow [24, 25], or to de-ice aircraft wings [26, 27] in order to make aircraft more efficient.

For more comprehensive and up-to-date insights into recent and future applications of low temperature plasmas, we refer the reader to the road-map papers written by the low temperature plasma community [28].

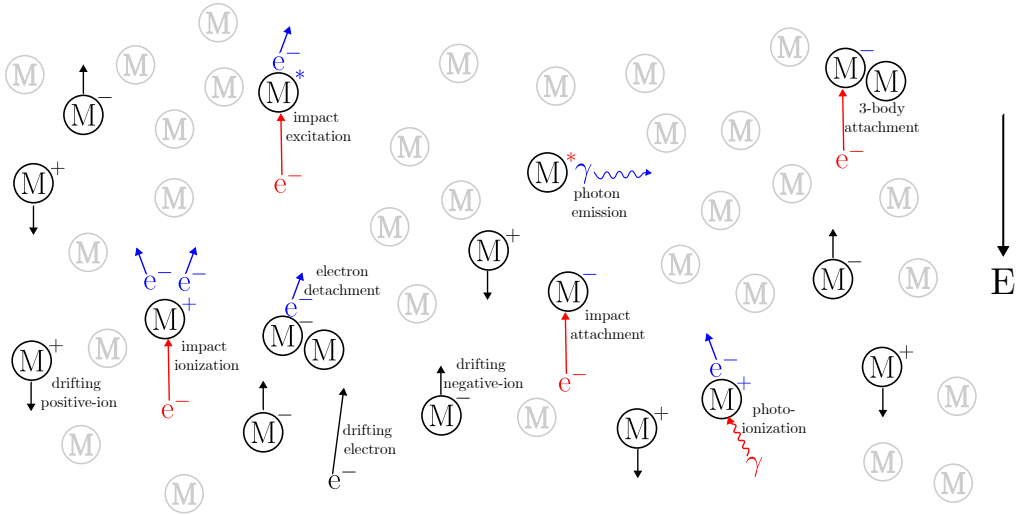
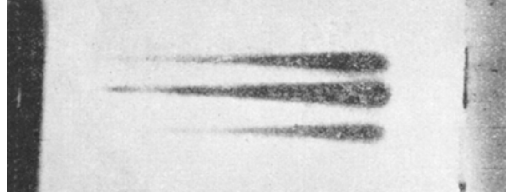


Figure 1.2: Illustration of the main collisional processes in a gas discharge under the influence of an external electric field E (direction shown on the right). The (M) symbol denotes a neutral gas atom or molecule (e.g., O_2 , H_2O , N_2 , or Ar), superscripts indicate the state: excited ($*$), positive ($+$), or negative ($-$). The red and blue colors indicate the state of the particles before and after the collision respectively. Image inspiration taken from [29].

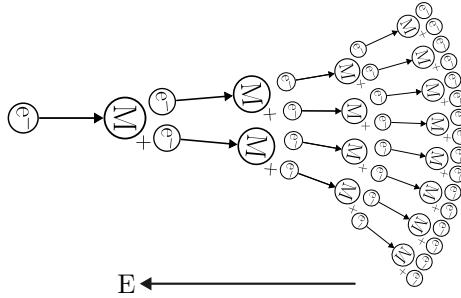
1.2 Microscale physics

Consider a sealed tube filled with a gas with two metal electrodes at its ends, one of which is grounded while the other is connected to a constant voltage. The source of electric current in this gas is the applied field, and free electrons that are usually generated from naturally occurring radiation, leftover from a previous discharge or are emitted from the negative electrode-terminal (also called secondary emission). These electrons gain energy as they are accelerated in the direction opposite to the external electric field maintained by the voltage supply. They collide with gas particles on their path and exchange momentum and energy. The average distance travelled by such electrons between collisions is called the mean free path, denoted as l_{mfp} . The energy gained by electrons between collisions depends on the product of l_{mfp} and the electric field. Depending on the electron energy and the gas particle, different types of collisions occur, some of which are shown in figure 1.2.

From figure 1.2 we see that some collisions liberate new electrons (e.g., impact ionization) whereas others attach to electrons (e.g., 3-body attachment). If the electron-liberating collisions occur more often than the electron-attaching collisions, then electron numbers rapidly increase resulting in an avalanche of electrons. Figure 1.3 shows experimentally imaged electron avalanches and an



(a)



(b)

Figure 1.3: (a) Experimental observation of electron avalanches (historical image taken from [30]) and (b) a schematic illustration of an electron avalanche. The direction of the electric field is indicated.

illustration of an avalanche moving from left to right. Electron avalanches tend to occur when the electric field is above a certain critical value E_k , called the critical field or the breakdown field. For air at standard temperature and pressure, the breakdown field E_k is around 30 kV/cm.

When the space charge of electron avalanches grows sufficiently large, it evolves into other types of discharges. These discharges can differ in several characteristics, such as whether they are stationary or transient, how significantly their space charge affects the applied field, and the extent to which they heat the gas. Table 1.1 shows a classification of discharges based on these characteristics. Discharges can transition from one type to another depending on factors like gas pressure, applied voltage, and electrode gap. For example, in relatively long gaps with a high voltage, we could initially have ‘cold’ filamentary streamer discharges which eventually transitions into a hot leader or spark discharge.

1.3 Streamer discharges

Below we briefly describe the basics of streamer discharges. For a more comprehensive introduction, refer to the review [31].

	negligible space charge	space charge dominated	heating dominated
Transient	Avalanche	Streamer	Leader
Stationary	Townsend	Glow	Spark

Table 1.1: Classification of discharges evolving under a constant or pulsed voltage conditions. Image inspiration taken from [29].

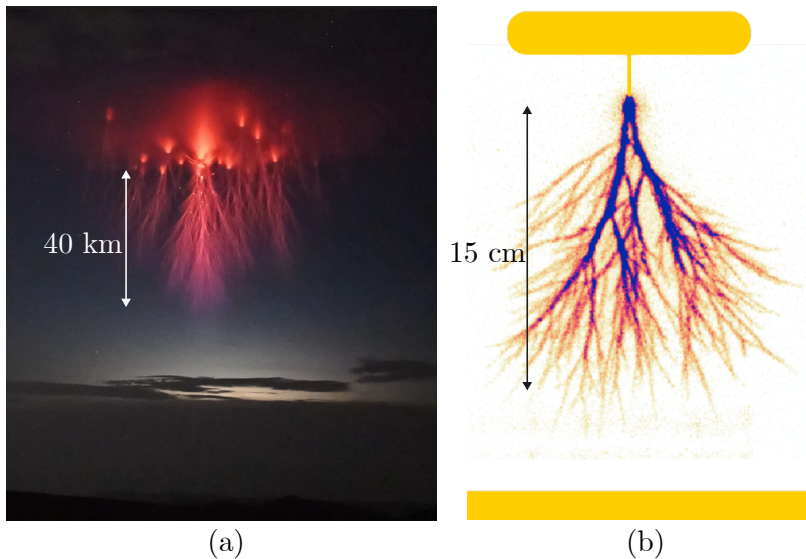


Figure 1.4: Streamer discharge examples:(a) sprite discharge occurring in the rarefied air high in the earth’s atmosphere [32], (b) streamer discharge in air at 0.6 bar pressure, generated in a laboratory [33] which has a similar structure but is orders of magnitude smaller.

Streamers are filamentary discharges that occur as precursors to other discharges or as sprites in the earth’s upper atmosphere. Figure 1.4 shows snapshots of a sprite and a lab-generated streamer discharge in air. They propagate due to the enhanced electric field resulting from their curved space-charge layer, known as the streamer head, and leave behind a wake of quasi-neutral plasma, also known as the streamer channel (see figure 1.5). The local field enhancement due to the curved streamer head (see figure 1.5) is well above the breakdown value, enabling streamers to move into regions where the electric field is below the breakdown value.

A streamer is either positive or negative depending on the polarity of the space-charge layer at its tip, which also determines the direction in which it propagates. A positive streamer has a space-charge layer which has a net posi-

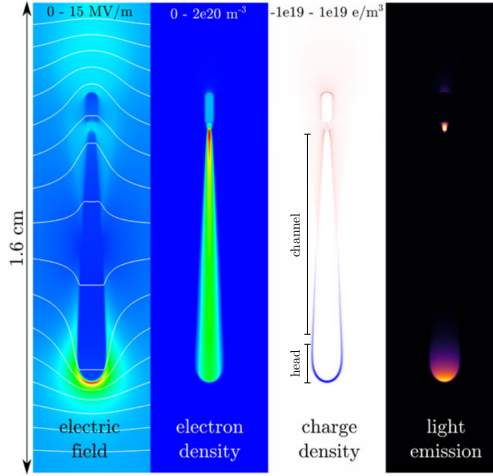


Figure 1.5: Simulation of a downward propagating positive streamer simulation in air at STP. Shown are the cross-sections of the electric field, electron density, charge density (blue: positive and red: negative) and light emission. Also roughly indicated are the streamer head and channel in the charge density cross-section. Image taken from [31].

tive charge (figure 1.5) and propagates by attracting free electrons in front of it (like a vacuum cleaner sucking up dust particles). Thus it is important that a positive streamer has a source of free electrons in front of it to propagate. These electrons are provided by either natural radiation or leftover ionization [34] or by photoionization (see figure 1.2) [35]. In contrast, a negative streamer has a space-charge layer with a net negative charge and propagates by the drift of existing and newly created of electrons away from its head. Thus, unlike positive streamers, negative streamers do not need a source of free electrons at their tip to be able to propagate. Due to the different propagation mechanisms of positive and negative streamers, their inception and properties like propagation velocities, head radii and maximum fields vary as well.

Scaling laws: Streamers at different gas densities tend to be similar and can be understood by simple scaling laws [31, 36–38]. As mentioned in section 1.2, the energy gained by an electron before a collision depends on the product $l_{\text{mfp}} \times E$, where E is the electric field. If the average energy gained by the moving electrons between collisions is the same, then we have similar collisions occurring, which leads to similar discharge characteristics. Naturally, the mean free path depends inversely on the gas number density N , i.e., $l_{\text{mfp}} \propto 1/N$. The electron energy gain between collisions is therefore proportional to E/N .

When comparing streamers at different gas densities, we need to scale their lengths with N similar to l_{mfp} . In figure 1.4, we show a sprite discharge extending over altitudes of 40 to 80 km and a laboratory discharge at sea level. At these

altitudes of 80 or 0 km, the gas number densities N are approximately $3.8 \times 10^{20} \text{ m}^{-3}$ and $2.5 \times 10^{25} \text{ m}^{-3}$ respectively [39]. Correspondingly, we see that the sprite discharge is approximately five orders of magnitude longer than the laboratory discharge.

Multiscale nature of streamers: Even if we only consider atmospheric pressure, a wide range of spatial (μm to m) and temporal scales (ps to μs) are required to describe streamers [38]. The longest streamer can reach meter-sized lengths [40]. But they are only a few mm wide, see figure 1.4. We then have the really thin space charge layer at the streamer head which is usually in the μm range. At the smallest spatial scale, we have the electron mean free path l_{mfp} , which is usually below one μm . The corresponding smallest temporal scale is the electron collision time, which is usually below one ps (10^{-12} s). Streamers in air typically propagate at velocities of 10^5 to 10^7 m/s . The formation of meter-scale discharges therefore corresponds to roughly a μs time scale.

1.4 Introduction to the computational model

We briefly introduce the computational model that we used to simulate various streamer discharges. We use a so-called drift-diffusion-reaction type fluid model, in which all the plasma species are modeled as continuous densities. Such models are used to simulate various types of electrical discharges, e.g., dielectric barrier discharges [41, 42], or glow discharges [43]. We use the in-house, open source code `afivo-streamer` [44], based on the Afivo framework [45] to perform all our simulations. The Afivo framework is based on the finite-volume method with structured mesh. Additionally, it has features like adaptive mesh refinement (AMR), OpenMP parallelism [46], and a geometric multigrid method-based Poisson equation solver. `Afivo-streamer` has been verified against other codes in [47], validated against experiments in [48, 49] and compared with particle model results in [50].

1.4.1 Model equations

Here we present the equations of the drift-diffusion-reaction model. For a derivation, refer to [2, 3]. The time evolution of the electron density n_e is given by

$$\partial_t n_e = \nabla \cdot (\mu_e \mathbf{E} n_e + D_e \nabla n_e) + S_e + S_{\text{ph}}, \quad (1.1)$$

where μ_e is the electron mobility coefficient, D_e the diffusion coefficient, and \mathbf{E} the electric field. S_e is a source (and sink) term due to reactions involving electrons, for example ionization or attachment and is as follows:

$$S_e = (\alpha - \eta) \mu_e |\mathbf{E}| + \text{other reactions}, \quad (1.2)$$

where α and η are the number of ionizing and attaching collisions per unit length per electron. S_{ph} is a photo-ionization source term, which is implemented according to Zheleznyak's model [35] as discussed in [47]. Alternatively, it can be modeled using a discrete Monte-Carlo approach which realistically models the stochasticity of electron density ahead of the streamer [49, 51]. Ion and neutral densities n_i (numbered by $i = 1, \dots, n$) evolve in time as

$$\partial_t n_i + \nabla \cdot (q_i \mu_i \mathbf{E} n_i) = S_i. \quad (1.3)$$

Here S_i is a source/sink term due to various reactions, μ_i is the mobility (which we set to zero when ion motion is ignored) and q_i accounts for the species' charge (0 for neutrals, -1 for negative ions and $+1$ for positive ions).

The electric field \mathbf{E} is calculated in the electrostatic approximation as $\mathbf{E} = -\nabla\phi$. Here ϕ is the electrostatic potential, which is obtained by solving the Poisson equation [45, 52]

$$\nabla^2 \phi = -e (\sum q_i n_i - n_e) / \epsilon_0, \quad (1.4)$$

where $e (\sum q_i n_i - n_e)$ is the space charge density and ϵ_0 is the vacuum permittivity. The electrostatic approximation is valid when the time derivative of the magnetic field is small compared to the right-hand side of equation (1.4), which is generally the case for streamer discharges, see section 5.1 of [31].

Transport data

Electron transport data: We use the local field approximation in our fluid model, so that the electron transport and reaction coefficients (e.g., α and η) depend on the reduced electric field (E/N). We obtain these transport and rate coefficients using Boltzmann solvers [53, 54] or Monte Carlo swarm solvers [55, 56], which in turn require electron-neutral cross sections. These coefficients are computed externally using the Boltzmann solver BOLSIG- [53] and used as tabulated input data for our simulations in this thesis. These cross-section data are collected from various research groups and are hosted as databases on the LXCat website [57]. The choice of database affects the simulated streamer properties, because there is still some uncertainty in certain cross sections.

Ion transport data: In general ions are convected by the electric field, however they are orders of magnitude slower than electrons because of their heavier mass. As a result, their motion can be ignored for most streamer discharge simulations. In Chapters 2 and 4, we include ion motion of some major ions by assuming they have a constant mobility of $2.2 \times 10^{-4} \text{ m}^2/(\text{sV})$ [58]. This is because we perform simulations longer than a few microseconds which is long enough for ion motion to become important.

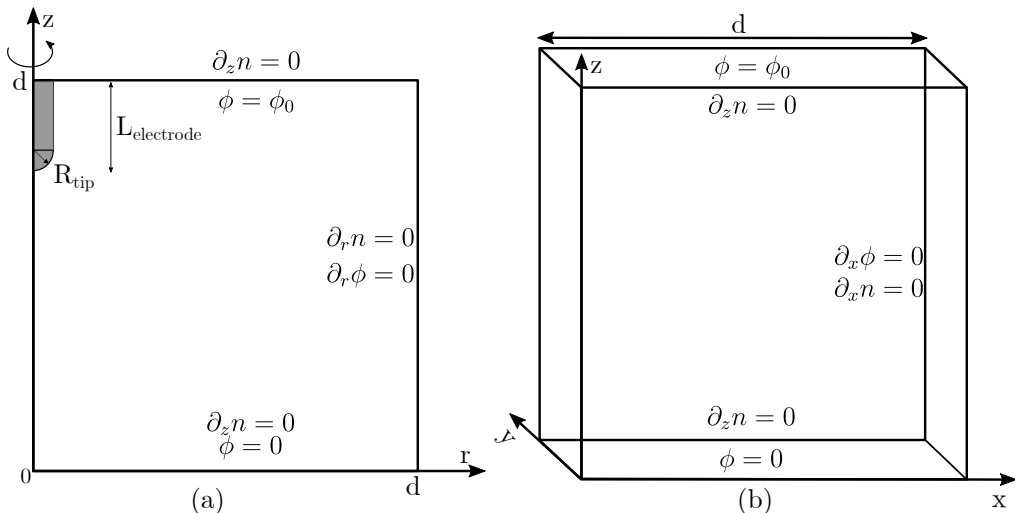


Figure 1.6: The two 3D domains used in this work: cylindrically symmetric (left) and full 3D (right). The dimensions of the domains are given in the respective chapters. Boundary conditions for the species densities n and the electrostatic potential ϕ for each of the domain boundaries are given.

1.4.2 Domain and boundary conditions

For all the results in this work, we used a plate-plate geometry with an electrode as shown in figure 1.6 (left), except in Chapter 5, where we use a cube-shaped domain as shown in figure 1.6 (right).

For the plasma species densities, homogeneous Neumann boundary conditions (gradients normal to the boundary are set to zero) are used on all domain boundaries. For the electric potential, a zero Dirichlet boundary condition (grounded) is used at $z = 0$ and a non-zero Dirichlet boundary condition (applied voltage) is used at $z = d$. For the rest of the boundaries, a homogeneous Neumann boundary condition is used for the electric potential.

1.4.3 Computational algorithms

The equations introduced in section 1.4.1 are solved using the finite-volume method due to its relative ease of implementation, conservative properties, and already existing effective advection-diffusion schemes [59]. The drift terms in equations (1.1), (1.3) are discretized with an upwind scheme using the Koren limiter [60], and the diffusive term is handled through a central differencing scheme. The various source terms are evaluated at the cell centers. For more details on how this was achieved in conjunction with adaptive mesh refinement, we refer the reader to [45].

Mesh details

Resolving the various length scales involved (see section 1.3) in a streamer discharge will be computationally expensive if we use a uniform mesh size. For computational efficiency, we therefore use the adaptive mesh refinement capabilities of the Afivo library. The mesh consists of regular blocks of N^D cells, where N is for example 8 and D is the dimensionality of the simulation. These blocks can be refined by splitting them into 2^D blocks with half the grid spacing. For our streamer simulations, the refinement criterion is related to the growth of the electron density due to ionizing collisions. This means that the simulation should resolve a typical length scale $1/\alpha$ (see equation 1.2), resulting in the following refinement criterion [44]

$$\begin{aligned} &\text{refine if } \alpha(E)\Delta x > c_1, \\ &\text{de-refine if } \alpha(E)\Delta x < c_2, \end{aligned}$$

where c_1 and c_2 are constants which we take to be $c_1 = 1.0$ and $c_2 = 0.125$.

In figure 1.7, we show an example of mesh refinement around various regions at various points of a single streamer simulation.

Poisson solver

Solving the Poisson equation (1.4) on a uniform grid at every timestep tends to be computationally expensive. Therefore, a fast Poisson solver with AMR is required. In our case we use an iterative solver called geometric multigrid method [61] that is implemented in the Afivo library [45]. The suitability of this approach as compared to other approaches has been discussed in detail in section 6.6 of [31]. Additionally, this library has the added advantage of being able to handle curved electrodes via the level-set function approach [52].

Time integration and time step criteria

We integrate the final discretized system of equations using Heun's method (alternatively known as the explicit trapezoidal rule) [62], which is a second-order accurate, two-step, explicit-in-time method. In short, given a system of ordinary differential equations $d_t \mathbf{n} = \mathbf{f}(t, \mathbf{n})$, then the Heun's method is as follows:

$$\text{First step : } \tilde{\mathbf{n}}(t^{k+1}) = \mathbf{n}(t^k) + \Delta t \mathbf{f}(t^k, \mathbf{n}^k) \quad (1.5)$$

$$\text{Second step : } \mathbf{n}(t^{k+1}) = \mathbf{n}(t^k) + \frac{1}{2}\Delta t \left[\mathbf{f}(t^k, \mathbf{n}(t^k)) + \mathbf{f}(t^{k+1}, \tilde{\mathbf{n}}(t^{k+1})) \right] \quad (1.6)$$

where $\mathbf{n}(t^k)$ is the evaluation at the k th timestep, and Δt the time step. For more details, refer to [62]. We use a combination of Δt restrictions to keep our numerical solutions stable:

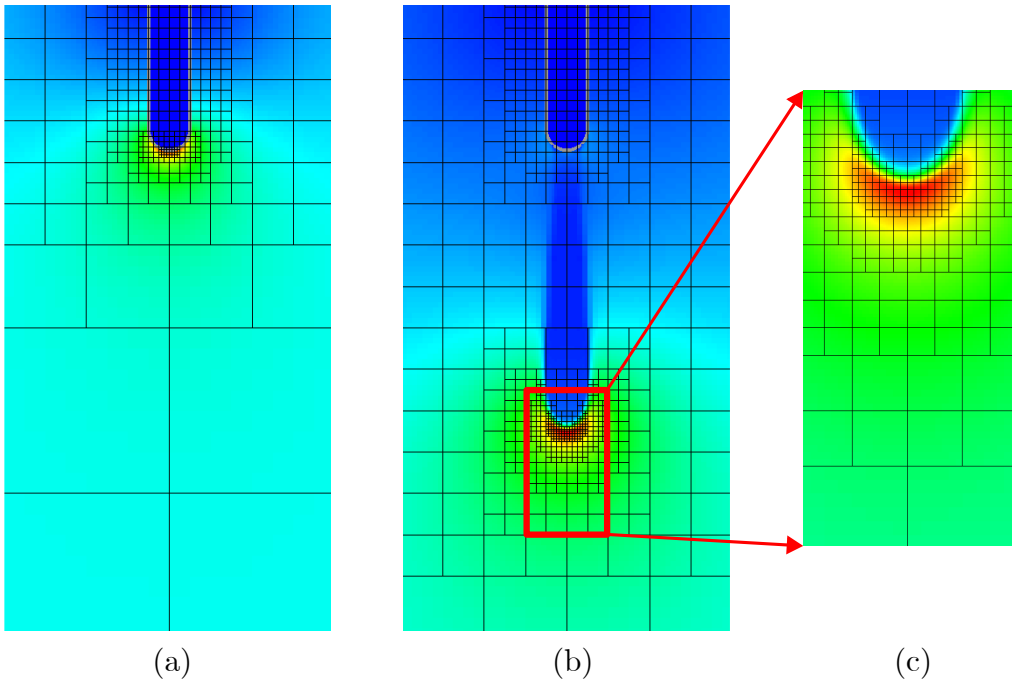


Figure 1.7: An illustration of the adaptive mesh refinement in a simulation of a positive streamer discharge emerging from an elongated electrode. Each square corresponds to a block of 8×8 grid cells. (a) In the electrode region, where the electric field is high, we see more refinement than the rest of the domain. (b) The refinement has shifted to the streamer head where the electric field is high. (c) Zoom of the streamer head.

- The CFL condition [63] arising from the finite volume discretization of the drift and diffusion terms:

$$\Delta t_{\text{cfl}} = 0.5 \left[\sum_{i=1}^{N_{\text{dim}}} \left(\frac{2D_e}{\Delta x_i^2} + \frac{|\mu_e E_i|}{\Delta x_i} \right) \right]^{-1} \quad (1.7)$$

- Dielectric relaxation time:

$$\Delta t_{\text{drt}} = \frac{e\mu_e n_e}{\epsilon_0} \quad (1.8)$$

- Optional time step restriction due to plasma chemistry: Below we take the minimum value of the ratio of each of the species densities and their time derivatives, n_0 is a non-zero number to avoid computational issues arising in the zero density regimes.

$$\Delta t_{\text{chem}} = \min \left(\frac{n + n_0}{\frac{d}{dt}n} \right) \quad (1.9)$$

- The final time step of the simulation is calculated as follows:

$$\Delta t = 0.9 \times \min\{\Delta t_{\text{drt}}, \Delta t_{\text{cfl}}, \Delta t_{\text{chem}}\} \quad (1.10)$$

1.5 Research questions

In this thesis we study positive streamers primarily in artificial air under (repetitive) pulsed conditions, and we address the following questions:

- **Chapter 2: What chemical and physical processes govern the streamer evolution after the first voltage pulse and during the second pulse?** We perform double-pulse streamer simulations by varying the interpulse time and the oxygen percentage of the dry air.
- **Chapter 4: How does the Joule heating of repetitively pulsed streamers affect their properties?** We couple the streamer fluid model with a gas dynamics model. Then we vary input parameters like applied voltage, repetition frequency and heating efficiency to investigate how the neutral gas temperature increases and how this changes streamer properties.
- **Chapter 3: How good is our input data for simulating streamers in humid air?** We investigate the effect of using different input data on streamer simulations in humid air. Different cross-section data sets, photoionization models and chemical reactions sets are compared.

- Chapter 5: **In which frequencies are radio waves emitted by positive streamers?** We perform positive streamer simulations in 3D for the following cases: single streamer propagation using the Helmholtz approximation and the Monte Carlo approach for photoionization, a streamer branching, streamers interacting with an ionized patch and two streamers colliding. Then we compute the radiated fields for each of these cases and analyse the emitted spectra as a function of time.

Chapter 2

Double pulse streamer simulations with varying interpulse times in air

In this chapter, we study how streamer discharges are influenced by a previous voltage pulse using an axisymmetric fluid model. We simulate double-pulse positive streamers in $\text{N}_2\text{-O}_2$ mixtures containing 20% and 10% O_2 at 1 bar. By varying the time between the pulses between 5 ns and 10 μs , we observe three regimes during the second pulse: streamer continuation, inhibited growth and streamer repetition. In the streamer continuation regime, a new streamer emerges from the tip of the previous one. In the inhibited regime, the previous channel is partially re-ionized, but there is considerably less field enhancement and almost no light emission. Finally, for the longest interpulse times, a new streamer forms that is similar to the first one. The remaining electron densities at which we observe streamer continuation agree with earlier experimental work. We introduce an estimate which relates streamer continuation to the dielectric relaxation time, the background field and the pulse duration. Furthermore, we show that for interpulse times above 100 ns several electron detachment reactions significantly slow down the decay of the electron density.

This chapter has been published as [\[64\]](#):

H. Malla, A. Martinez, U. Ebert, and J. Teunissen. Double-pulse streamer simulations for varying interpulse times in air. *Plasma Sources Sci. Technol.*, Volume 32 (9) 095006, 2023.

2.1 Introduction

Streamers are transient, filamentary gas discharges [31, 65]. Due to the strong electric field enhancement at their tips they can propagate in background electric fields below the breakdown threshold. In nature they occur as streamer coronas ahead of lightning leaders, and as tens of kilometers tall sprite discharges in the thin atmosphere high above thunderstorms. Streamer discharges can be used to generate various chemical species and they are used in applications such as plasma medicine [20, 66, 67], agriculture [68], industrial surface treatments [69], and combustion [70].

Streamers are commonly produced using a repetitively pulsed voltage source [71–73]. The repetition rate determines how strongly discharges are affected by previous pulses, through left-over ionized and neutral species as well as gas heating. Such effects from previous pulses can cause transitions between corona, glow and spark discharge regimes [74]. In [75], simulations were performed to study the evolution of electrons, positive and negative ions during the interpulse.

The effect of pulse repetition frequencies on positive streamers in molecular nitrogen-oxygen mixtures was studied systematically in double pulse experiments in [71, 72]. In [71] different formation and propagation behavior was observed for the second-pulse streamer depending on the time between the two voltage pulses. If this time was sufficiently short, the first-pulse streamers continued their growth during the second pulse. The maximum time between two voltage pulses for which this happens was called the continuation time. The authors were able to explain how continuation times vary with the O₂ percentage by zero-dimensional plasma-chemical modeling.

The effect of previous pulses has also been analyzed experimentally or using global kinetics models in the context of plasma jets in [76, 77]. They focus on the minimum electron density needed to observe the repeatable behaviour of a plasma jet. In a recent paper [78], three consecutive negative voltage pulses were simulated for an atmospheric plasma jet to investigate the role of left-over charged species after the first pulse. Repetitive-pulsed DBD experiments were performed in [79, 80], and different breakdown regimes were identified depending on the pulse-off time similar to [71]. Furthermore, streamer memory effects and discharge mode transitions due to repetitive pulses have been studied in a series of papers by Zhao *et al.*, see e.g. [81, 82], and reviewed in [83].

The remaining electron density from a previous pulse can influence where a discharge will grow during the next pulse. Such an effect was observed [71], and it was studied in another context with laser-generated ionization in [84, 85]. The contribution of electrons detached from various negative ions to the seed electrons of subsequent pulses was studied in several papers [34, 77, 78, 86].

In this chapter, we address an open question posed in [71]: which physical mechanism determines the electron density required for streamer continuation? Furthermore, we study how the second-pulse discharge changes when the time

between the voltage pulses is increased beyond the continuation time. To this end, we perform simulations of double-pulse positive streamers in two N₂-O₂ mixtures with 20% and 10% O₂ at standard temperature and pressure, using a 2D axisymmetric fluid model. We use a detailed plasma chemistry including neutral and excited species, which allows us to investigate the relative contribution of various detachment reactions after the first pulse.

2.2 Model

We study streamer discharges at 1 bar and 300 K in two nitrogen-oxygen mixtures containing 20% and 10% oxygen in an average background field of 15 kV/cm. Axisymmetric simulations are performed with a standard drift-diffusion fluid model with the local field approximation, using the `afivo-streamer` code [44]. For a recent comparison of this model against experiments and against particle simulations see [87] and [50]. We briefly summarize the main equations below, for further details see e.g. [44, 47].

2.2.1 Equations

The electron density n_e evolves in time as

$$\partial_t n_e = \nabla \cdot (\mu_e \mathbf{E} n_e + D_e \nabla n_e) + S_e + S_{\text{ph}}, \quad (2.1)$$

where μ_e is the electron mobility coefficient, D_e the diffusion coefficient, and \mathbf{E} the electric field. The electron transport coefficients are assumed to depend on the local electric field (local field approximation) and were computed using BOLSIG- [53] using Phelps' cross-section data [88]. S_e is a source (and sink) term due to reactions involving electrons, for example ionization or attachment, see section 2.2.4. S_{ph} is a photo-ionization source term, which is here implemented according to Zheleznyak's model [35] as discussed in [47]. Ion and neutral densities n_i (numbered by $i = 1, \dots, n$) evolve in time as

$$\partial_t n_i + \nabla \cdot (q_i \mu_i \mathbf{E} n_i) = S_i. \quad (2.2)$$

Here S_i is a source/sink term due to reactions, μ_i is the mobility and q_i accounts for the species' charge (0 for neutrals, -1 for negative ions and $+1$ for positive ions).

The electric field \mathbf{E} is calculated in the electrostatic approximation as $\mathbf{E} = -\nabla\phi$. Here ϕ is the electrostatic potential, which is obtained by solving the Poisson equation [45, 52]

$$\nabla^2 \phi = -\rho/\epsilon_0, \quad (2.3)$$

where ρ is the space charge density and ϵ_0 is the vacuum permittivity.

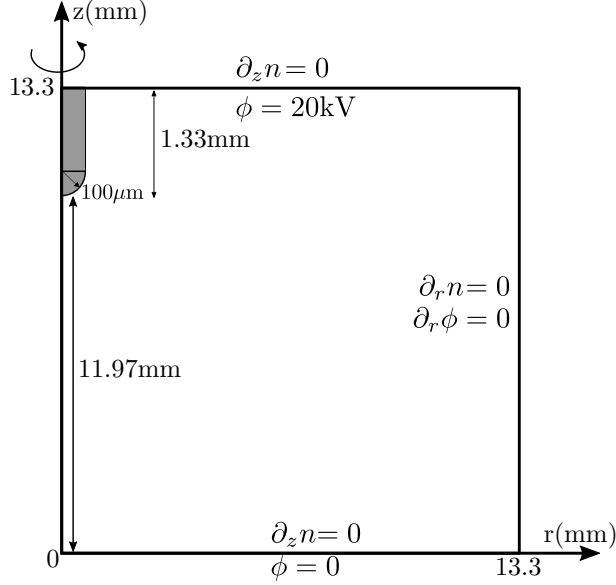


Figure 2.1: The axisymmetric plate-plate geometry with a needle electrode. Boundary conditions for the species densities n and the electrostatic potential ϕ for each of the domain boundaries are given.

2.2.2 Geometry

We use a plate-plate geometry with a needle electrode which is shown in figure 2.1. For species densities, homogeneous Neumann boundary conditions are used on all domain boundaries. For the electric potential, a homogeneous Neumann boundary is used on the outer radial boundary. The bottom plate is grounded, while a high voltage is on the upper plate and the needle electrode. The applied voltage is 20 kV, so that the average field between the plates is 15 kV/cm, which is about half the breakdown field at 1 bar.

2.2.3 Voltage waveform and initial conditions

The applied voltage waveform is shown in figure 2.2, consisting of two identical pulses separated by a time Δt_{inter} that is varied from 5 ns to 10 μs . The peak voltage V_{appl} is 20 kV, which is applied during 13 ns, and the rise and fall times of the voltage are 1 ns. As an initial condition, we use a neutral (electrons and O_2^+) background ionization density of $1.8 \times 10^9 \text{ m}^{-3}$. This background ionization provides the first electrons for streamer inception near the electrode tip, where there is significant electric field enhancement. Inception occurs approximately 1 ns after the voltage is turned on.

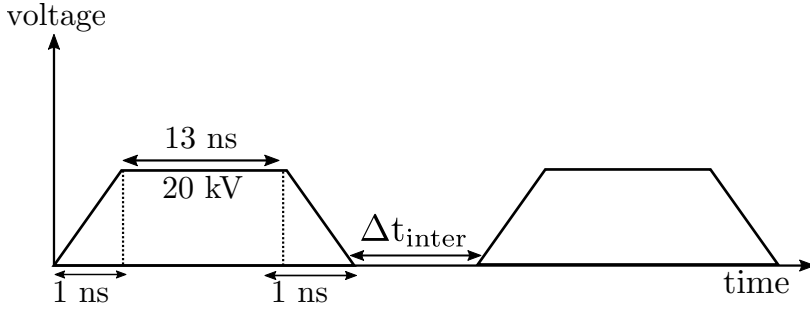


Figure 2.2: The applied voltage waveform with two identical pulses. The time between the pulses Δt_{inter} is varied from 5 ns to 10 μs .

Table 2.1: List of species used in the simulations. We use the reaction set described in [89].

Neutral	N_2 , O_2 , NO , NO_2 , NO_3 , N_2O , N_2O_3 , N_2O_5 , N_2O_4 , O_3 , $\text{N}(^4\text{S})$, $\text{N}(^2\text{D})$, $\text{N}(^2\text{P})$, $\text{O}(^1\text{D})$, $\text{O}(^1\text{S})$, $\text{O}(^3\text{P})$
Positive	N^+ , N_2^+ , N_3^+ , N_4^+ , N_2O_2^+ , N_2O^+ , NO_2^+ , NO^+ , O_2^+ , O_4^+ , O^+
Negative	e^- , N_2O^- , NO_2^- , NO_3^- , NO^- , O_2^- , O_3^- , O_4^- , O^-
Excited	$\text{N}_2(\text{rot})$, $\text{O}_2(\text{rot})$, $\text{N}_2(\text{A})$, $\text{N}_2(\text{B})$, $\text{N}_2(\text{a})$, $\text{N}_2(\text{C})$, $\text{N}_2(\text{E})$, $\text{O}_2(\text{a})$, $\text{O}_2(\text{b})$, $\text{O}_2(\text{A})$, $\text{N}_2(\nu=1-8)$, $\text{O}_2(\nu=1-4)$

2.2.4 Reaction Set

We use the reaction set given in [89], containing 263 reactions, which was primarily compiled from the reactions given in [90, 91]. This set includes reactions between electrons, neutrals, ions, and excited species. A list of the 56 considered species is given in table 2.1. Rate constants for reactions involving electron collisions were computed with BOLSIG+ [53] using the cross-sections from [88]. We remark that the reaction set was designed for dry air (20% O_2 , 80% N_2), and that using the same reactions for 10% O_2 is an approximation as some rate coefficients could depend on the O_2 concentration.

We consider the motion of seven major ion species: N_2^+ , O_2^+ , N_4^+ , O_4^+ , O_2^- , O^- , and O_3^- ; other ions are assumed to be immobile. For simplicity, we assume that the mobile ions all have a constant mobility $2.2 \times 10^{-4} \text{m}^2\text{V/s}$ [58], because ion motion played no major role for the results reported in this chapter.

In section 2.4.4, we use the reaction set used in [48] which is a subset of the above described reaction set to demonstrate the effect of using a simplified reaction set on the interpulse plasma evolution.

2.3 Results

2.3.1 Effect of interpulse time on streamer continuation

We vary the interpulse time Δt_{inter} in two gas mixtures, consisting of N_2 with 20% O_2 or 10% O_2 , to study the properties of the streamer generated by the second voltage pulse. Figures 2.3 and 2.4 show streamers at the end of the second pulse (but before the voltage fall time) for varying Δt_{inter} , for the cases of 20% O_2 and 10% O_2 , respectively. In these figures, the instantaneous light emission is approximated by the Abel-transformed $\text{N}_2(\text{C}^3\Pi_u)$ density, since most of the emission comes from the second positive system [92]. The forward Abel transform was performed using the Hansen-Law method [93]. Axial electric field profiles corresponding to figure 2.3 are shown in figure 2.6.

Depending on Δt_{inter} , we observe three regimes: continuation, inhibited growth and streamer repetition, which are discussed below. In figure 2.5, we show the streamer evolution during the second pulse at equally spaced time intervals for $\Delta t_{\text{inter}} = 25$ ns and 50 ns.

Continuation regime.

For short interpulse times the channel created by the first pulse still has a relatively high conductivity. The existing channel therefore becomes electrically screened during the second pulse, as shown in figure 2.5a, leading to the emergence of a new streamer from its tip. For larger Δt_{inter} the conductivity of the existing channel is lower, which results in a longer electric screening time. This results in a longer inception delay for the second streamer, which is therefore shorter. The maximum time between the pulses for which continuation occurs is here called the streamer continuation time. In section 2.4.2 a criterion for streamer continuation is discussed.

Inhibited regime.

For longer Δt_{inter} the first-pulse streamer channel has lost so much of its conductivity that it does not become fully screened during the second pulse (see figure 2.5b), and there is no streamer continuation. However, the electron density in the old channel is still high enough to inhibit a new streamer from forming, and a weak ionization wave passes through the channel instead. Light emission plots in figure 2.5 show that there is almost no light emission during the second pulse. In [71], such an inhibited regime was also observed. Other studies have also found that a relatively high background electron density reduces the field enhancement of a streamer, leading to slower discharge growth and a lower degree of ionization, see e.g. [85, 87].

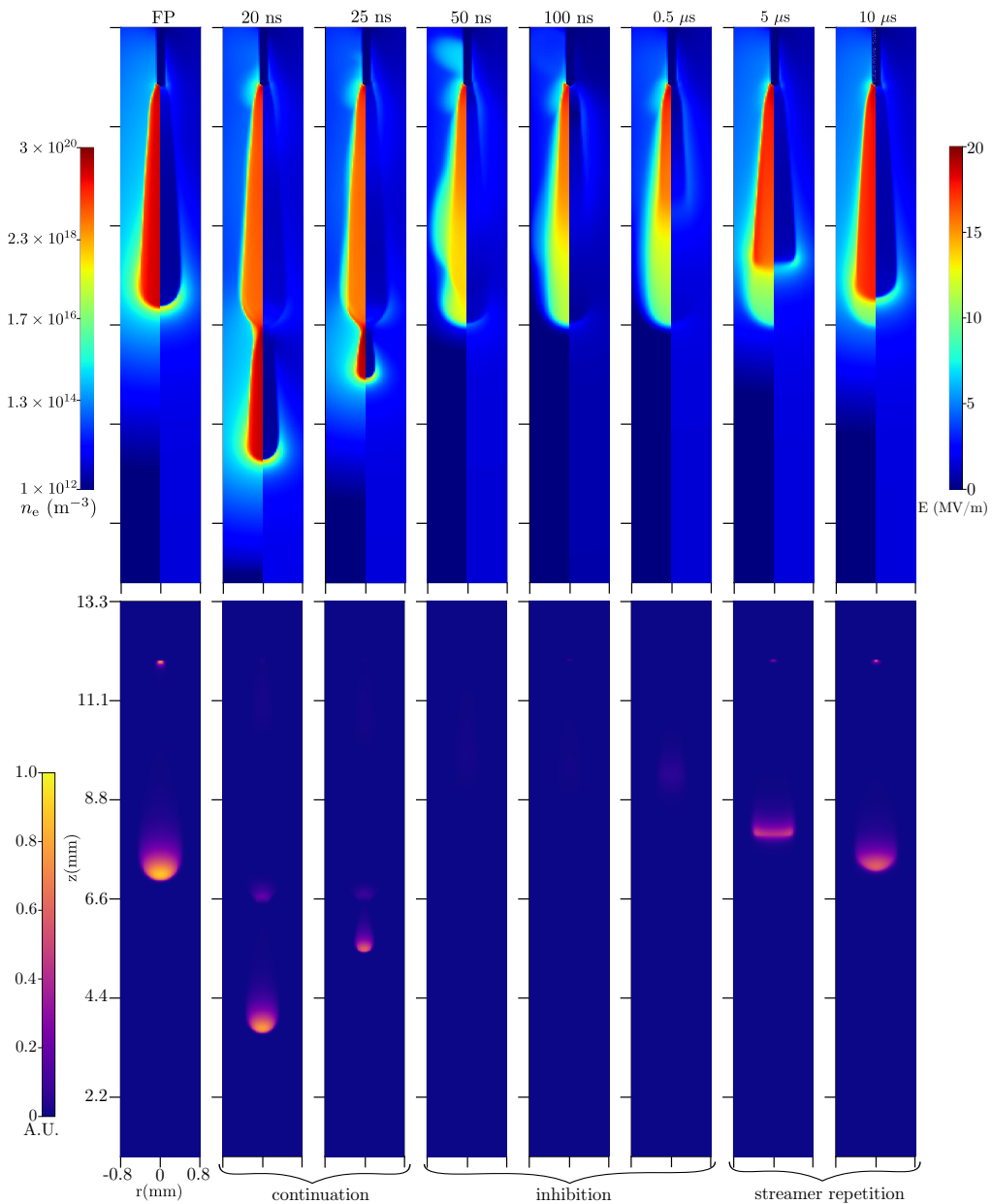


Figure 2.3: Plots of the first pulse (FP) streamer (left most column) and of the second streamer for interpulse times of 20 ns to 10 μs (as indicated above each column), for 20% O_2 . Each column shows electron density (top, left half) and electric field (top, right half) and instantaneous light emission (bottom), all at the end of the pulse but before the fall time. Light emission was computed using a forward Abel transform. The three observed regimes, streamer continuation, inhibited growth and streamer repetition are indicated.

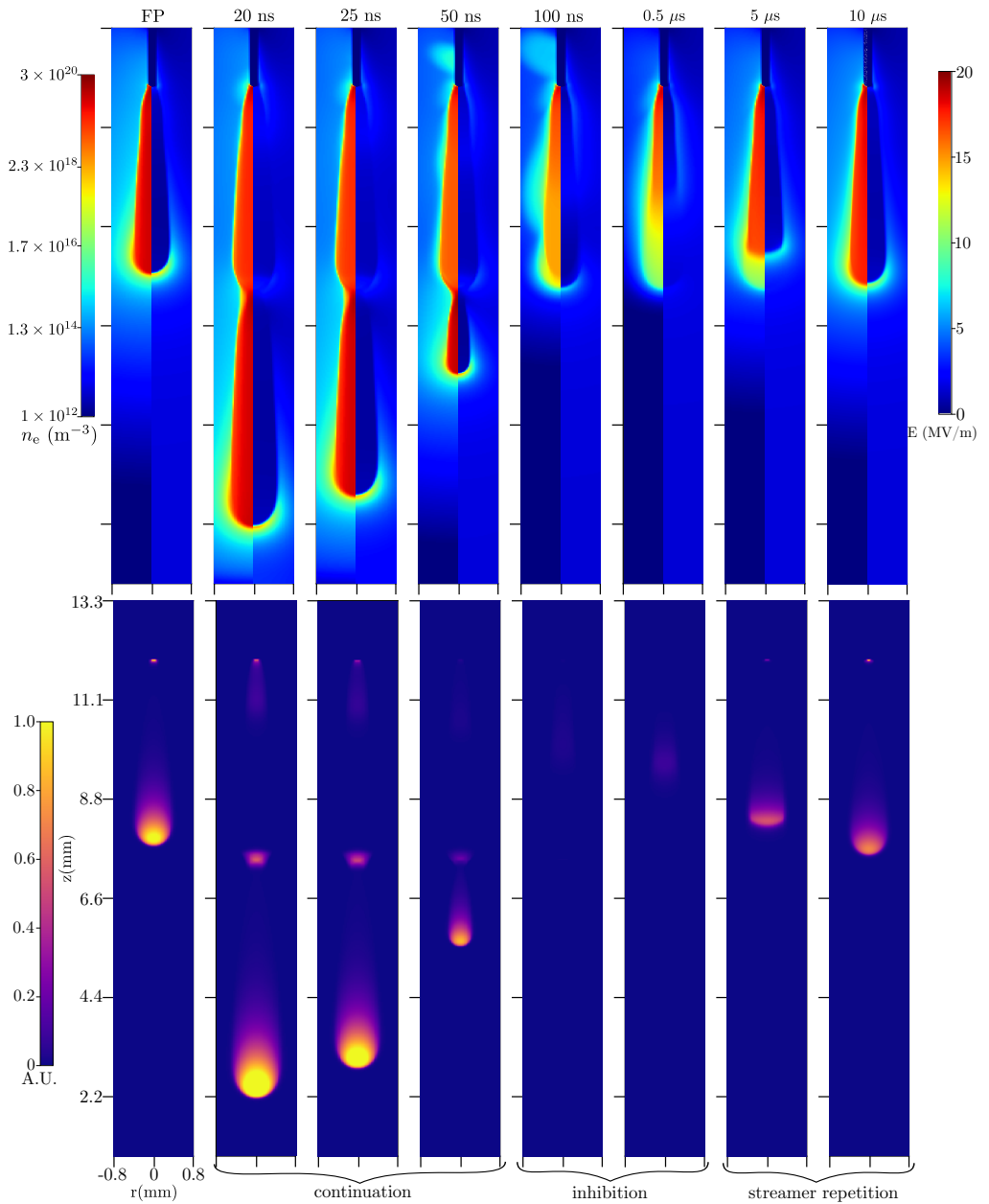


Figure 2.4: The same plots as in figure 2.3, but now for 10% O₂.

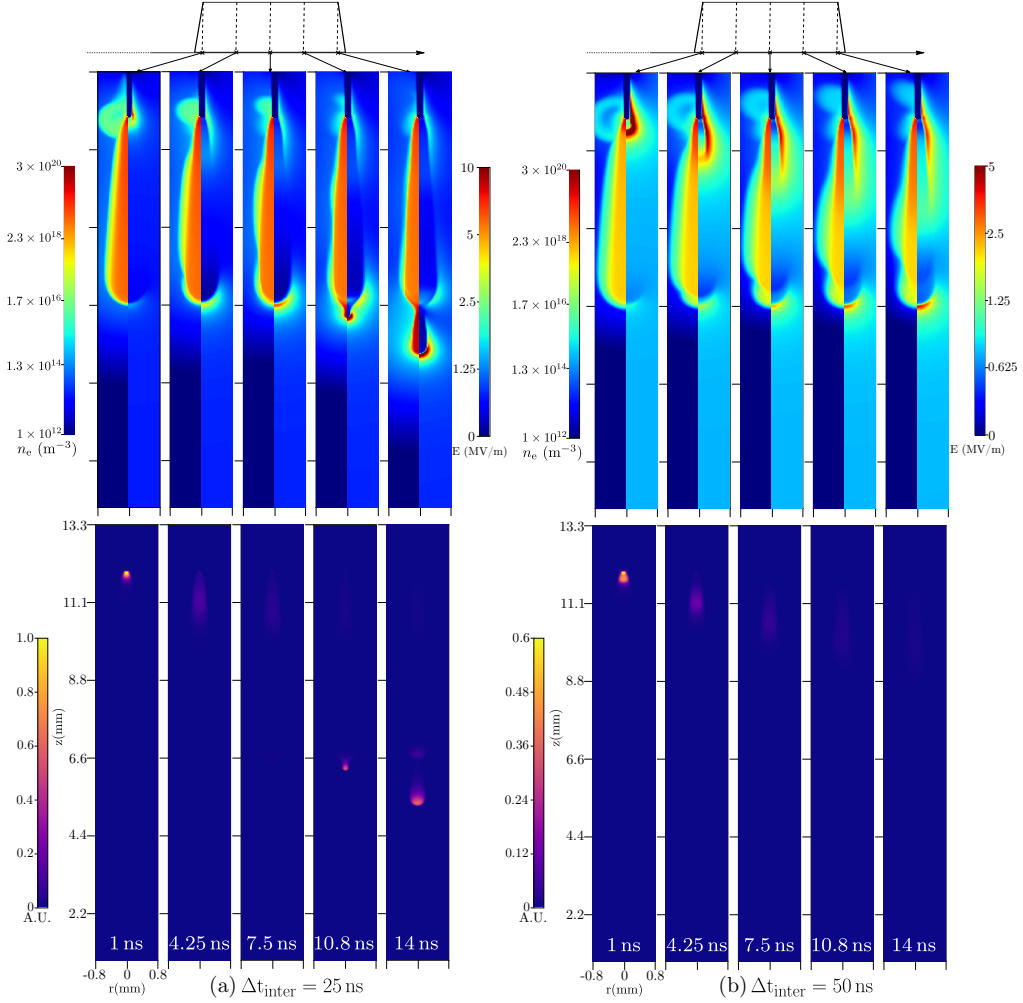


Figure 2.5: Evolution during the second voltage pulse for interpulse times of 25 and 50 ns, for 20% O₂, at equally spaced intervals. The time offsets with regard to the rise of the second voltage pulse are indicated at the bottom and visually at the top. On top, the electron density and the electric field are shown (left and right half of each image), and on the bottom the instantaneous light emission is shown.

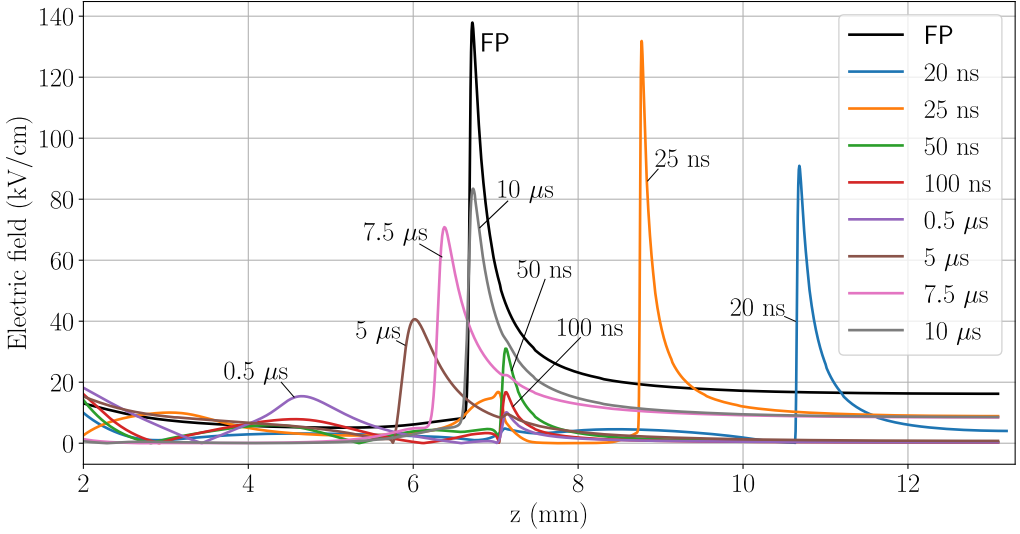


Figure 2.6: Electric field profile at the end of the second pulse (but before the voltage falls) for 20% O_2 , at varying interpulse times. Electric field profile for the first-pulse streamer is plotted as a black curve for reference.

Streamer repetition regime.

For even longer Δt_{inter} , the re-ionization of the channel becomes more streamer-like, as can be seen in figure 2.6: the electric field is enhanced at the tip of the re-ionized region and it is screened behind the tip. Note that the electric field for this second-pulse streamer is still weaker than for the first pulse, and that its head shape is somewhat deformed. Eventually, the electron density of the previous channel will become so low that it hardly affects the evolution during the second pulse. We approach this behavior for $\Delta t_{\text{inter}} = 10 \mu\text{s}$, where the second-pulse streamer therefore closely resembles the first-pulse streamer.

One might expect the effect of gas heating to influence the second-pulse streamer properties. However, this is not the case because the amount of energy deposited before the second pulse is so small that ambient gas heating is negligible, as discussed in 2.7.3.

2.3.2 Channel evolution between pulses

To better understand the evolution of second-pulse streamer, figure 2.7 shows the time evolution of the electron density at a point 1 mm below the electrode tip starting from the moment when the first pulse is off, i.e., from $t = 15 \text{ ns}$. We observe two electron decay timescales. For times up to $0.1 \mu\text{s}$, the electron density and hence the conductivity decay rapidly due to electron attachment and electron-recombination reactions. For $t > 0.1 \mu\text{s}$, the electron decay rate reduces due to detachment reactions. The main attachment and detachment reactions

Table 2.2: Additional positive ion conversion and electron-ion recombination reactions. $T(\text{K})$ and $T_e(\text{K})$ are gas and electron temperatures, respectively. T_e is computed as $T_e = 2\epsilon_e/3k_B$ with the mean electron energy ϵ_e obtained from BOLSIG- [53].

No.	Reaction	Reaction rate coefficient	Ref
Positive ion conversion			
R14	$\text{N}_2^+ + \text{O}_2 \rightarrow \text{O}_2^+ + \text{N}_2$	$k_{14} = 6.0 \times 10^{-17} \left(\frac{300}{T_e}\right)^{0.5} \text{m}^3 \text{s}^{-1}$	[90]
R15	$\text{N}_2^+ + \text{N}_2 + \text{M} \rightarrow \text{N}_4^+ + \text{M}$	$k_{15} = 5.0 \times 10^{-41} \left(\frac{300}{T_e}\right)^{2.2} \text{m}^6 \text{s}^{-1}$	[90]
R16	$\text{N}_4^+ + \text{O}_2 \rightarrow \text{O}_2^+ + \text{N}_2 + \text{N}_2$	$k_{16} = 2.5 \times 10^{-16} \text{m}^3 \text{s}^{-1}$	[90]
R17	$\text{O}_2^+ + \text{O}_2 + \text{M} \rightarrow \text{O}_4^+ + \text{M}$	$k_{17} = 2.4 \times 10^{-42} \left(\frac{300}{T_e}\right)^{3.2} \text{m}^6 \text{s}^{-1}$	[90]
Electron-ion recombination			
R18	$e + \text{N}_2^+ + \text{M} \rightarrow \text{N}_2 + \text{M}$	$k_{18} = 6.0 \times 10^{-39} \left(\frac{300}{T_e}\right)^{1.5} \text{m}^6 \text{s}^{-1}$	[90]
R19	$e + \text{O}_2^+ + \text{M} \rightarrow \text{O}_2 + \text{M}$	$k_{19} = 6.0 \times 10^{-39} \left(\frac{300}{T_e}\right)^{1.5} \text{m}^6 \text{s}^{-1}$	[90]
R20	$e + \text{N}_2^+ \rightarrow \text{N}_2$	$k_{20} = 1.5 \times 10^{-13} \text{m}^3 \text{s}^{-1}$	[58]
R21	$e + \text{O}_2^+ \rightarrow \text{O}_2$	$k_{21} = 1.5 \times 10^{-13} \text{m}^3 \text{s}^{-1}$	[58]
R22	$e + \text{N}_4^+ \rightarrow \text{N}_2 + \text{N}_2$	$k_{22} = 2.0 \times 10^{-12} \left(\frac{300}{T_e}\right)^{0.5} \text{m}^3 \text{s}^{-1}$	[90]
R23	$e + \text{O}_4^+ \rightarrow \text{O}_2 + \text{O}_2$	$k_{23} = 1.4 \times 10^{-12} \left(\frac{300}{T_e}\right)^{0.5} \text{m}^3 \text{s}^{-1}$	[90]

while the voltage is off are given in table 2.3.

The concentration of O_2 in the ambient gas mixture affects the relative contribution of different attachment reactions. For example, during an interpulse time of 500 ns, the percentage contribution to electron loss is as follows:

- Three-body attachment to O_2 gas (R1+R2): 75% (20% O_2) and 55% (10% O_2). Note that the rates of R1 and R2 depend quadratically and linearly on the O_2 concentration.
- Dissociative recombination (R3): 24% (20% O_2) and 44% (10% O_2). This reaction results from the fast conversion of positive ions into O_4^+ inside the streamer channel [94].

Other reactions are responsible for only about 1% of the electron loss. These relative contributions are not sensitive to the interpulse time, with a variation of less than 10% for all the interpulse times.

2.4 Discussion

2.4.1 Comparison with earlier experimental work

In [84], double pulse streamer experiments were performed at 133 mbar for varying interpulse times and for varying O_2 concentrations. With 0D plasma-chemical modeling, it was estimated that the minimum remaining electron density n_e^{\min} for streamer continuation was about $5 \times 10^{17} \text{m}^{-3}$, using a pulse duration t_{const} of about 200 – 300 ns with a rise/fall time of 15 ns. At 1 bar, these values scale to $n_e^{\min} \sim 3 \times 10^{19} \text{m}^{-3}$ and $t_{\text{const}} \sim 27 - 30$ ns, see [31].

Table 2.3: Major reactions that consume and produce electrons when the voltage is turned off. The full reaction set as specified in [89] and used throughout the chapter contained 21 electron attachment and recombination reactions and 18 electron detachment reactions. Reaction R4 from [95] was included to account for field-dependent electron detachment. Note the rate of this reaction should depend on the O_2 concentration [95], but for simplicity we here use a single rate coefficient for both O_2 concentrations, as the rates are similar. T (K) and T_e (K) are gas and electron temperatures, respectively. T_e is computed as $T_e = 2\epsilon_e/3k_B$ with the mean electron energy ϵ_e obtained from BOLSIG- [96]. The ‘‘simple chemistry’’ added in Fig. 2.7 also consists of reactions R1, R3, and R4.

No.	Reaction	Reaction rate coefficient	Ref
Major electron-loss reactions			
R1	$e + O_2 + O_2 \rightarrow O_2^- + O_2$	$k_1(E/N)$	[88]
R2	$e + O_2 + N_2 \rightarrow O_2^- + N_2$	$k_2 = 10^{-43}$	[88]
R3	$e + O_4^+ \rightarrow O_2 + O_2$	$k_3 = 1.4 \times 10^{-12} (300/T_e)^{0.5}$	[90]
Electron-detachment reactions			
R4	$O_2^- + M \rightarrow e + O_2 + M$	$k_4 = 1.24 \times 10^{-17} \exp(-(\frac{179}{8.8+E/N})^2)$	[95]
R5	$O_2^- + O_2^*(b) \rightarrow e + 2O_2$	$k_5 = 3.60 \times 10^{-16}$	[90]
R6	$O_2^- + N_2^*(A) \rightarrow e + O_2 + N_2$	$k_6 = 2.10 \times 10^{-15}$	[90]
R7	$O_2^- + O(^3P) \rightarrow e + O_3$	$k_7 = 1.50 \times 10^{-16}$	[90]
R8	$O_2^- + N(^4S) \rightarrow e + NO_2$	$k_8 = 5 \times 10^{-16}$	[90]
R9	$O_3^- + O(^3P) \rightarrow e + 2O_2$	$k_9 = 3 \times 10^{-16}$	[90]

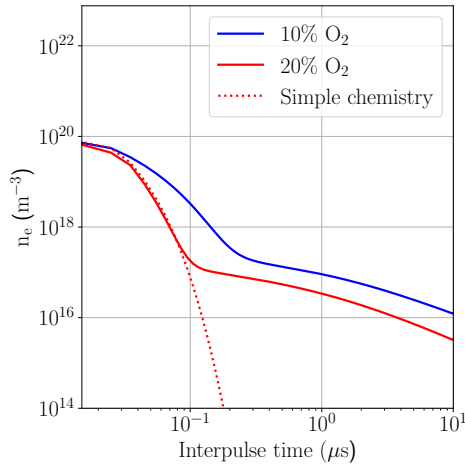


Figure 2.7: The temporal evolution of the electron density during the interpulse phase. The values were obtained at a point 1 mm below the electrode tip. The plot with ‘Simple chemistry’ will be elaborated further in section 2.4.4

For the simulations performed here, with a pulse duration $t_{\text{const}} \sim 13$ ns, we observe streamer continuation for n_e^{min} in the range of 10^{19} m^{-3} up to $4 \times 10^{19} \text{ m}^{-3}$. Compared to the results of [84], some deviations are to be expected, due to the uncertainties in the 0D plasma-chemical modeling in [84], due to corrections to the scaling with pressure, and due to the different electrode geometries and pulse shapes. We therefore consider our results to be in relatively good agreement with [84].

In [80], experiments were performed in a 1 mm overvolted DBD gap containing N_2 with 0.1% O_2 at atmospheric pressure, and a 10 kV voltage was applied with a 10 kHz repetition frequency. Different breakdown regimes were observed by varying the voltage-off time t_{off} between pulses. For $t_{\text{off}} > 20 \mu\text{s}$, a positive streamer propagated between the dielectric-covered electrodes, similar to the streamer repetition regime shown in figures 2.3–2.4. For $20 \mu\text{s} > t_{\text{off}} > 4 \mu\text{s}$, a slower and more diffuse positive streamer developed, which was attributed to a high residual electron density in the gap. Finally, for $t_{\text{off}} < 0.5 \mu\text{s}$ no streamer propagation occurred, and instead a re-ignition of the previous discharge’s after-glow was observed, similar to the inhibition regime shown in figures 2.3–2.4. The authors explain these regimes through 1D modeling, which correlates t_{off} with the background ionization density that is present at the start of the next pulse, similar to the present study. The fact that similar regimes were observed despite the rather different operating conditions shows that left-over ionization plays a generic role in repetitively pulsed discharges.

2.4.2 Criterion for streamer continuation

If the channel eventually becomes electrically screened during the second pulse, as illustrated in the evolution in figure 2.5, a high electric field will again form at its tip, from which a streamer can continue to grow. Whether streamer continuation occurs therefore depends on the remaining conductivity in the previous channel and on the duration of the second pulse. Below we derive a rough estimate for streamer continuation.

We approximate the previous channel at the start of the second pulse as a cylinder with radius R and electric conductivity σ , with a semi-spherical cap, in which the electric field is equal to the background field E_{bg} , see figure 2.8. The electric current in the channel is then initially given by

$$I_0 = \pi R^2 \sigma E_{\text{bg}}. \quad (2.4)$$

This current will decrease over time due to the screening of the background field. For simplicity, we assume that the accumulated charge at the end of the channel is given by

$$Q(\tau) = I_0 \tau, \quad (2.5)$$

where τ is the time since the start of the second pulse. We assume this charge

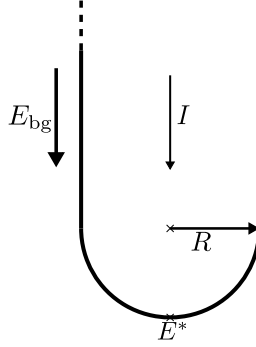


Figure 2.8: Schematic illustration of the assumed streamer shape used in section 2.4.2. The streamer is approximated by a cylinder with a hemispherical cap of radius R .

Q gives rise to an electric field similar to that of a (semi-)spherical charge distribution with radius R

$$E^*(\tau) = E_{\text{bg}} + \frac{1}{4\pi\epsilon_0} \frac{Q(\tau)}{R^2}. \quad (2.6)$$

If we now define a required electric field for discharge inception E_{inc} , we can determine the time τ it takes until $E^* = E_{\text{inc}}$. We include a correction factor k for this time scale, of order unity, which accounts for e.g. the partial screening over time and the fact that the actual channel is not a cylinder with a hemispherical cap. The resulting estimate for τ is then given by

$$\tau = 4k (E_{\text{inc}}/E_{\text{bg}} - 1) \tau_{\text{drt}}, \quad \text{where } \tau_{\text{drt}} = \epsilon_0/\sigma. \quad (2.7)$$

Equation (2.7) provides an estimate for the time τ needed for a streamer to emerge from the tip of a previous one (as illustrated in figure 2.5). Note that τ depends on the interpulse time through the conductivity σ , which decays in the previous channel during the interpulse time. We will now compare equation (2.7) against the simulation results presented in section 2.3. We estimate the required field for discharge inception as $E_{\text{inc}} = 100 \text{ kV/cm}$. Since $E_{\text{bg}} = 15 \text{ kV/cm}$, the factor $4k(E_{\text{inc}}/E_{\text{bg}} - 1)$ is then about $23k$. In the simulations, we measure the time τ_{obs} until a field of strength E_{inc} has been reached at the tip of the previous streamer, with $\tau_{\text{obs}} = 0$ corresponding to the start of the second pulse plus its rise time of 1 ns. Furthermore, we approximate the effective conductivity of the previous streamer as

$$\sigma = \int_0^{R'} 2\pi r \sigma(r) dr / (\pi R'^2), \quad (2.8)$$

where $\sigma(r)$ is a radial conductivity profile 0.5 mm behind the streamer head, and R' is defined as the radius at which $\sigma(r)$ has dropped to 10% of its maximum value. Since the contribution of ions to the conductivity is relatively small for the cases considered here, we approximate $\sigma(r)$ as $e\mu_e(r)n_e(r)$.

Δt_{inter} (ns)	τ_{drt} (ns)	τ_{obs} (ns)	$\tau_{\text{obs}}/\tau_{\text{drt}}$
10	0.0616	1.46	23.7
15	0.0978	2.86	29.2
20	0.162	4.88	30.1
25	0.267	7.01	26.3
50	-	-	-

(a) 20% O₂

Δt_{inter} (ns)	τ_{drt} (ns)	τ_{obs} (ns)	$\tau_{\text{obs}}/\tau_{\text{drt}}$
10	0.0349	1.11	31.8
15	0.0427	1.61	37.7
20	0.0553	2.05	37.1
25	0.0699	2.52	36.1
50	0.164	5.77	35.2

(b) 10% O₂

Table 2.4: Dielectric relaxation times τ_{drt} at the start of the second pulse, based on equation (2.8), together with the observed inception delays τ_{obs} for second-pulse streamers. Specifically, τ_{obs} was here defined as the time it takes for the maximal electric field to reach 100 kV/cm after the rise time of the second pulse.

In table 2.4, we list observed continuation times τ_{obs} together with $\tau_{\text{drt}} = \varepsilon_0/\sigma$, where σ was computed according to equation (2.8) at the start of the second pulse. The ratio $\tau_{\text{obs}}/\tau_{\text{drt}}$ lies between 24 and 38, which is in agreement with equation (2.7) for k between 1.0 and 1.5.

2.4.3 Role of detachment reactions

The chemistry we use [89] has 18 different electron detachment reactions which are of the form



where A is one of O⁻, O₂⁻, O₃⁻ and M is a neutral species in its ground or excited state.

Table 2.3 lists the six detachment reactions that contribute significantly to the production of electrons after the end of the first pulse. Although our chemistry includes electron detachment reactions from O⁻ ions, they are not included in table 2.4 because they made a much smaller contribution for our operating conditions.

In figure 2.9a we show the relative contribution of electron-producing reactions during the interpulse for the case of 20% O₂. For short interpulse times, there is still a major contribution from ionization reactions, which take place due to the decaying field enhancement after the voltage is turned off. For longer

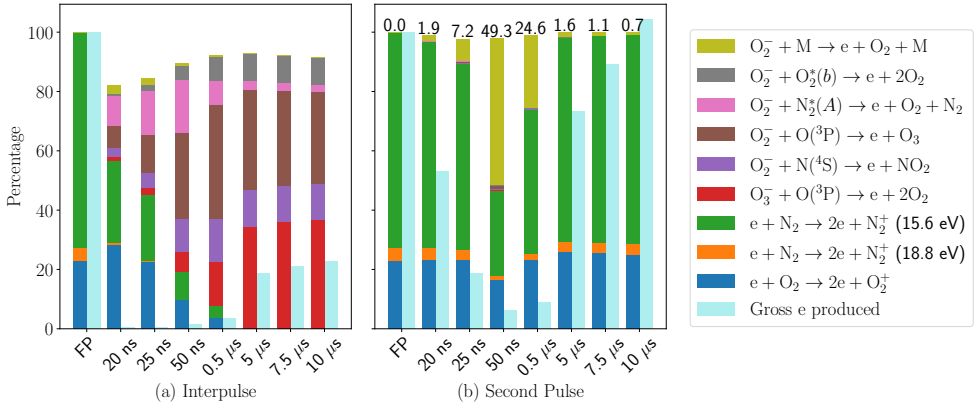


Figure 2.9: Relative contribution of electron-producing reactions during the interpulse (a) and the second pulse (b) for the case of 20% O_2 . The production during the first pulse, and the gross electron production normalized with that of the first pulse is shown for comparison. The percentage contribution of the field dependent detachment reaction $O_2^- + M$ to the gross electron productions is listed at the top of each bar in (b).

interpulse times, most electron production is due to detachment reactions, with the relative contribution of O_3^- detachment increasing over time. Note that the reaction $O_2^- + M \rightarrow e + O_2 + M$ plays only a minor role during the interpulse due to its field-dependent rate coefficient.

Figure 2.9b shows relative contributions of electron-producing reactions during the second pulse. Now field-dependent detachment from O_2^- is the major electron detachment reaction. For Δt_{inter} equal to 50 ns and 500 ns, this reaction is responsible for a significant fraction of the total electron production (which includes ionization reactions). This is mainly due to two factors: the availability of a large number of O_2^- ions, and a reduction in ionization reactions due to lower field enhancement in the inhibited growth regime, see figure 2.5b. For interpulse times of $5 \mu\text{s}$ or more, O_2^- ions are lost due to negative-ion conversion and ion-ion recombination reactions. For interpulse times below 25 ns, detachment from O_2^- does not play a significant role since the previous channel is quickly screened and a new streamer forms.

Results for the case of 10% O_2 and 90% N_2 are given in appendix 2.7.1. We observe a similar trend in the relative contributions of detachment reactions for this case.

2.4.4 Effect of using a different chemistry set

For comparison, we have also simulated the electron density decay during the interpulse with a simpler plasma chemistry from [48]. This chemistry contains

8 species and 15 reactions, and it lacks the extensive electron, ion, neutral and excited species reactions as compared to the chemistry set used in the rest of this chapter. For electrons, the same Phelps [88] cross sections are used. In figure 2.7, where we denote the smaller chemistry from this section as ‘Simple Chemistry’, we compare the electron decay inside the streamer channel during the interpulse phase. The decay agrees well up to 100 ns, but at later times the simpler chemistry predicts a much faster decay due to the absence of the various electron detachment reactions. For a pulse duration of 100 ns or more, the sets would therefore lead to different streamer continuation times.

2.5 Conclusions

We have investigated streamer continuation with double-pulse simulations in N_2 containing 20% and 10% O_2 at 1 bar. We use two identical voltage pulses of 15 ns, and vary the interpulse time Δt_{inter} between 5 ns and 10 μs . For increasing Δt_{inter} , we observe three regimes during the second pulse:

- In the streamer continuation regime ($\Delta t_{\text{inter}} \lesssim 50 \text{ ns}$), a new streamer emerges from the tip of the previous one.
- In the inhibited growth regime ($50 \text{ ns} \lesssim \Delta t_{\text{inter}} \lesssim 500 \text{ ns}$, with somewhat longer time scales for 10% O_2), the previous channel is partially re-ionized, but there is considerable less field enhancement and almost no light emission. This re-ionization wave becomes stronger for increasing interpulse times, characterized by increased electric field screening and increased light emission.
- For $\Delta t_{\text{inter}} \gtrsim 5 \mu\text{s}$, a new streamer forms that is similar to the first one. However, even for the longest interpulse times considered here (10 μs) this new streamer has lower field enhancement and is less bright than the first one.

With 10% O_2 these regimes occurred at slightly longer interpulse times than with 20% O_2 , due to lower electron attachment and recombination rates.

In our simulations, streamer continuation occurred when the remaining electron density was in the range of 10^{19} m^{-3} up to $4 \times 10^{19} \text{ m}^{-3}$. This range agrees with the estimate made in [71], based on experimental measurements and 0D modeling, when scaled to the same pressure. We derived an estimate for the time needed for streamer continuation to occur which depends on the conductivity of the previous channel and the background electric field. This estimate and our observed values of streamer inception delay in the simulations are in reasonable agreement. Furthermore, we show that for interpulse times above 100 ns several electron detachment reactions significantly slow down the decay of the electron density.

2.6 Outlook

We obtained our current results using a specific background electric field, pulse shape and pressure. In future work, our computational model could be improved in the following aspects:

- When the voltage falls to zero, the polarity of the electrode is reversed due to the remaining positive space charge. A cathode sheath with a really high local field is expected to form around the electrode, see e.g. [97–99]. Resolving such a sheath was computationally not feasible with our model, which is why homogeneous Neumann boundary conditions for species at the electrodes were used. The effect of more realistic electrode boundary conditions could be studied in future work.
- As shown in section 2.4.4, for longer interpulse times, it is important that we use a chemistry set that is complete and has accurate rate constants. It was also pointed out in [89] that some rate constants also depend on pressure and temperature. Thus, in order to be able to extend our results to different pressures, future work involves generalizing the reaction set.
- Finally, varying the pulse shape, background electric field, and gas composition might result in streamer branching, which would require fully 3D modeling.

These present and future investigations will allow for theoretical predictions for optimal pulse repetition frequencies for various plasma processing applications.

2.7 Appendix

2.7.1 Effect of varying O_2 concentration on detachment reactions

Here we show the relative contribution (in %) of various electron-producing reactions for the case of 10% O_2 . Figure 2.10 shows the contribution during the interpulse phase and figure 2.11 shows the contribution during the second pulse. In each of these figures, we also show the results from figure 2.9 for comparison.

2.7.2 Electric field inside the streamer channel during the interpulse

In Figure 2.12a, we show the electric field decay over time at various locations along the axis of the streamer channel for 20% O_2 . The electric field decays from 10^6 V/m (41 Td) to 10^2 V/m (0.004 Td) over a time interval of $5 \mu s$. However, the boundary conditions at the electrode are currently not very realistic in our model: a Neumann zero condition is used for electrons, which results in electrons freely

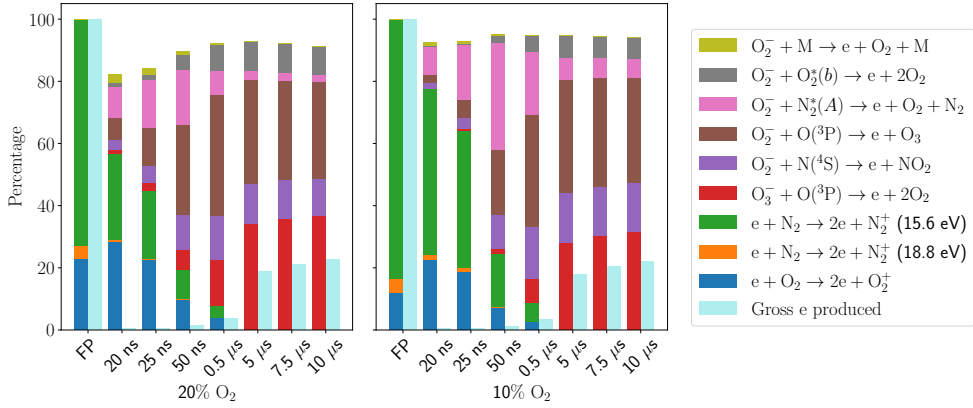


Figure 2.10: Relative contribution of electron-producing reactions during the interpulse for 10% O₂. The production during the first pulse is shown for comparison. We also show the gross electron production normalized to that of the first pulse.

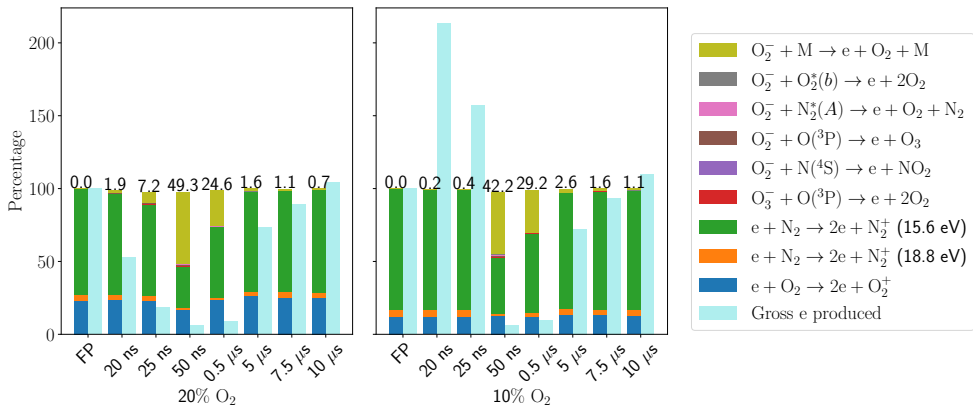
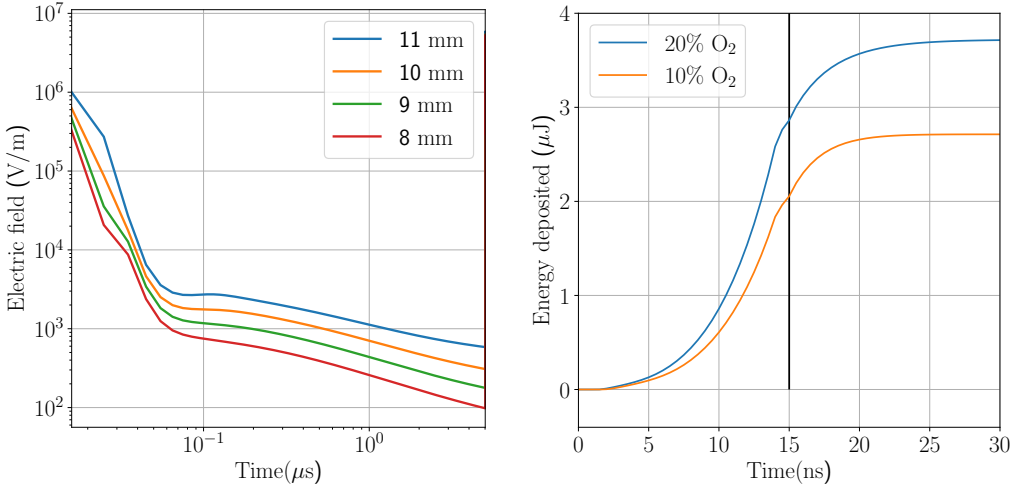


Figure 2.11: Relative contribution of electron-producing reactions during the second pulse for 10% O₂. The production during the first pulse and the gross electron production normalized to that of the first pulse is also shown. The percentage contribution of the field-dependent detachment reaction $O_2^- + M$ to the gross electron productions detachment is listed at the top of each bar plot. For 10% O₂ and $\Delta t_{\text{inter}} = 20 \text{ ns}$ and $\Delta t_{\text{inter}} = 25 \text{ ns}$, gross electron production during the second pulse is higher than during the first pulse.



(a) The temporal evolution of the on-axis electric field inside the streamer channel during the interpulse phase. The values were obtained at points 1, 2, 3 and 4 mm below the electrode tip, which is approximately located at $z = 12$ mm. (b) Space-time integrated Joule heating term. The vertical line is at the 15 ns mark, where the first pulse is turned off.

Figure 2.12: Figures related to appendices 2.7.2 and 2.7.3.

entering the domain after the voltage is turned off. This leads to a faster decay of the residual charge (and thus also of the electric field) than would occur with more realistic boundary conditions. In principle it is possible to specify more realistic boundary conditions at the electrode, in which the outflow of electrons is caused by secondary emission processes. However, with such boundary conditions we cannot run simulations for long time scales, since the anode effectively becomes a cathode after the voltage is turned off, resulting in the formation of thin sheaths with very high local electric fields. We intend to improve our model's boundary conditions in the future, for example by using the local energy approximation as in [100] and/or by approximating the electron dynamics in the sheath.

2.7.3 Effect of gas heating

Figure 2.12b shows the space-time integrated Joule heating ($\vec{j} \cdot \vec{E}$) during the first pulse. The energy deposited due to the first pulse is below $4 \mu\text{J}$, and no energy is deposited after 25 ns. At 1 bar and 300 K, dry air (80% N₂:20% O₂) has a density $\rho = 1.2 \text{ kg m}^{-3}$ and a specific heat capacity $C_p = 1000 \text{ J kg}^{-1} \text{ K}^{-1}$. This energy is deposited in a cylindrical volume of radius $r = 0.8$ mm (maximum width of the streamer channel) and height $h \approx 5.5$ mm (first pulse streamer

length). Even if we assume that all the energy instantaneously goes into gas heating, the temperature increase is only about $\Delta T = 4\mu\text{J}/(C_p\rho\pi r^2 h) \approx 0.3\text{ K}$. Such a small increase in temperature will not have a significant effect on the second-pulse streamer properties, which is why gas heating was not included in our model. In Chapter 4, we explore the effects of gas heating after many pulses.

Chapter 3

Streamer discharge simulations in humid air: uncertainty in input data and sensitivity analysis

When performing streamer discharge simulations in humid air, there is quite some uncertainty in the input data. In this chapter we study the sensitivity of such simulations to the choice of input data, focusing on positive streamers in air with 0%, 3% or 10% H₂O at 1 bar and 300 K. The simulations are performed with an axisymmetric fluid model, on time scales of about 100 ns. Our underlying motivation was to understand to what extent uncertainty in the input data could be reduced by comparing to experimental observations of streamers in humid air. We first consider different H₂O cross-section data and determine their effect on electron transport and streamer properties. Next, we investigate the effect of humidity on photoionization by comparing two humid-air photoionization models proposed in the literature. Finally, we study how the use of different sets of chemical reactions affects streamer properties. Three reaction sets from the literature are used, and a sensitivity analysis is performed to identify important reaction processes.

The manuscript with the results in this chapter is under preparation as the following publication:

B. Guo, H. Malla, A. Malagón, U. Ebert and J. Teunissen. Streamer discharge simulations in humid air: uncertainty in input data and sensitivity analysis.

Hemaditya Malla was responsible for all the initial data collection and the necessary ground work. All the simulations were performed by B. Guo. Writing the text and interpretation of results was equally divided among all the authors.

3.1 Introduction

Streamers are fast-propagating and filamentary ionization fronts featuring an enhanced electric field at their tips [2, 101, 102]. This electric field enables streamers to propagate in sub-breakdown background fields and therefore serve as precursors to more energetic phenomena such as spark and lightning leaders [103–105]. Streamers are fundamental blocks of some transient luminous events (TLEs) such as sprites and blue jets [106]. Sprites are tens of kilometers tall mesospheric discharges formed by thousands of streamers [37, 106–109]. Similarly, streamers shape the cold phase of blue jets [110–112], which emanate from thundercloud tops. Fast-breakdown [113] may also be comprised by hundreds of millions of streamers [114, 115], and source the observed pulsed radio emissions known as narrow bipolar events [113] and the transient blue luminous events emerging from thundercloud tops [116].

Although streamers are low-temperature plasmas, the strong electric field at the apex can accelerate electrons to really high energies and thus, can trigger high-temperature chemical reactions at nearly room temperature. This property has been harnessed for numerous applications such as plasma medicine [18, 117, 118], industrial surface treatments [119], air cleaning [120, 121], agriculture [21, 122], plasma-assisted combustion [123–126] and non-thermal plasma actuators [127, 128].

The gas composition affects streamer properties like velocity, radius, breakdown field, branching characteristics [48, 129–132] but also the species that the discharge produces. Frequently, water vapor is a component of the gas mixture. Specifically, when studying streamer-like discharges in atmospheric air for plasma medicine and agriculture applications, or in super-saturated air inside a thundercloud, humidity is a factor that cannot be neglected.

In the late 1970s, the pioneering experimental works by Griffiths and Phelps [133], Les Renardiens group [134, 135] and Gallimberti [103], showed that water vapor hampers streamer propagation. The recent papers [136, 137] use numerical models to investigate how humidity affects single streamer properties like channel and head radii, maximum field at the head and channel conductivity. The effects are especially noticeable for long streamer discharges where the plasma decay time-scale is relevant [137]. The decay of the conductivity is primarily driven by three-body attachment and electron ion recombination with positive water clusters which are produced in three-body reactions [136, 137]. Water vapor therefore has a more prominent effect on streamer discharges at higher pressures. A lower conductivity increases the voltage drop along the streamer channel, hindering the accumulation of charge at the ionization front [136]. This results in thinner channels and slower streamer propagation, in agreement with previous experimental work [103, 133–135].

One of the main challenges in modeling streamers (or other discharges) in humid air is selecting appropriate input data. For example, different cross sections

Case	H ₂ O	N ₂	O ₂	P (bar)	T (K)
1	0.0%	80.0%	20.0%	1.0	300
2	3.0%	77.6%	19.4%	1.0	300
3	10.0%	72.0%	18.0%	1.067	320

Table 3.1: Gas compositions considered in this chapter, with percentages relative to the gas number density $N_0 = 2.41 \times 10^{25} \text{ m}^{-3}$. Cases 2 and 3 correspond to 86% and 96% relative humidity, respectively.

for H₂O were used in [136] and [137], as well as different sets of chemical reactions, which can lead to significant differences in streamer properties. In this chapter, we therefore investigate how the choice of input data affects streamer properties such as their velocity, their optical diameter and their maximum electric field. We consider different e-H₂O cross section sets, different photoionization models and different sets of chemical reactions, and study their effect on single positive streamers in humid air.

The structure of the chapter is as follows. In section 3.2 the simulation model and the different types of input data are described. The effect of electron-neutral cross sections for H₂O is studied in section 3.3.1, the effect of different photoionization models in section 3.3.2 and the effect of different chemistry sets in section 3.3.3. To identify important reactions in the humid-air chemistry sets, a sensitivity analysis is performed in section 3.3.4.

3.2 Simulation model

We perform axisymmetric simulations of positive streamers with the `afivo-streamer` code [44], using a drift-diffusion fluid model with the local field approximation. The model is briefly described below, for further details see e.g. [44, 47].

The simulations are performed in gas mixtures containing N₂ and O₂ at a 4:1 ratio together with H₂O. We consider three humidities, with a mole fraction of 0%, 3% and 10% H₂O, as listed in table 3.1. At 1 bar pressure, 3% and 10% H₂O would correspond to 100% relative humidity at approximately 297 K and 319 K temperature respectively. We slightly vary the gas temperature and pressure to such that the relative humidity stays below 100% and also keep the gas number density $N_0 = 2.41 \times 10^{25} \text{ m}^{-3}$ the same. At 300 K and 1 bar with a concentration of 3% H₂O, the corresponding relative humidity is around 86%, whereas at 320 K and 1.067 bar with a concentration of 10% H₂O the relative humidity corresponds to around 96%.

3.2.1 Equations

In our model, the electron density n_e evolves in time as

$$\partial_t n_e = -\nabla \cdot (\mathbf{\Gamma}_{\text{drift}} + \mathbf{\Gamma}_{\text{diff}}) + S_e + S_{\text{ph}}, \quad (3.1)$$

where $\mathbf{\Gamma}_{\text{drift}} = -\mu_e \mathbf{E} n_e$ and $\mathbf{\Gamma}_{\text{diff}} = -D_e \nabla n_e$ are the drift and diffusive fluxes of electrons, μ_e is the electron mobility, D_e the diffusion coefficient, and \mathbf{E} the electric field. Furthermore, S_e is a source term due to reactions (e.g., ionization or attachment) as described in section 3.2.5, and S_{ph} is the photo-ionization source term described in section 3.2.4. Electron transport coefficients are assumed to depend on the local electric field, and they were computed using BOLSIG+ [53] using the cross sections described in section 3.2.3.

We consider time scales up to about 200 ns and found that including ion mobilities made no significant difference in our results. The motion of ions is therefore neglected, so that ions and neutral densities n_j (numbered by $j = 1, \dots, n$) evolve in time as

$$\partial_t n_j = S_j, \quad (3.2)$$

where S_j is a source/sink term due to reactions.

The electric field \mathbf{E} is calculated in the electrostatic approximation as $\mathbf{E} = -\nabla\phi$. The electrostatic potential ϕ is obtained by solving the Poisson equation

$$\nabla^2 \phi = -\rho/\epsilon_0, \quad (3.3)$$

using a geometric multigrid method [45, 52], where ρ is the space charge density and ϵ_0 is the vacuum permittivity.

3.2.2 Computational domain and initial conditions

We use a computational domain measuring 20 cm in the r and z directions, which contains a plate-plate geometry with a needle electrode (8 mm in length and 0.8 mm in diameter), as illustrated in figure 3.1. The bottom plate is grounded, while a constant high voltage V is applied on the upper plate and the needle electrode. The axial electric field away from the needle electrode relaxes to the average electric field between the two plate electrodes, which is here defined as the background electric field E_{bg} :

$$E_{\text{bg}} = V/d, \quad (3.4)$$

where $d = 20$ cm is the distance between two plate electrodes.

For the electric potential, a homogeneous Neumann boundary is used on the outer radial boundary. For species densities, homogeneous Neumann boundary conditions are used on all domain boundaries, including the needle electrode. Secondary electron emission from electrodes due to ions and photons is not included.

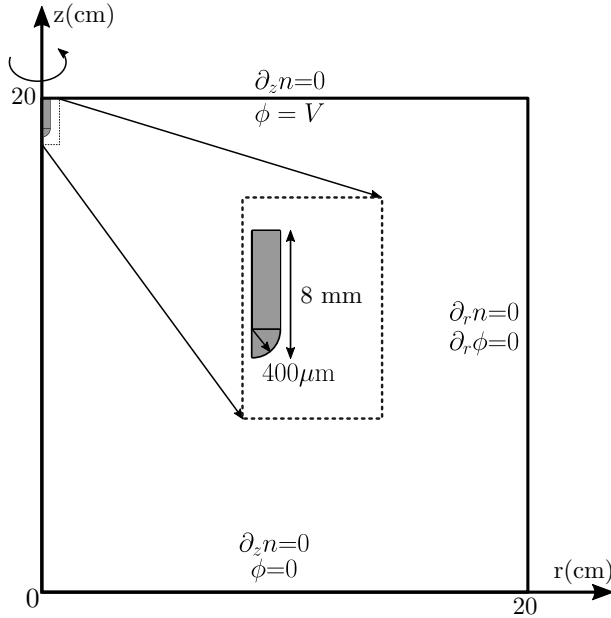


Figure 3.1: The axisymmetric plate-plate geometry with a needle electrode. Boundary conditions for the species densities n_j and the electrostatic potential ϕ are indicated at the domain boundaries.

As an initial condition, homogeneous background ionization with a density of 10^{11} m^{-3} for both electrons and N_2^+ ions is included. All other ion densities are initially zero. This background ionization provides the first electrons for streamer inception near the electrode tip, where there is significant electric field enhancement.

For computational efficiency the simulations are performed using adaptive mesh refinement (AMR). We used the same refinement criterion as in previous works (see e.g. [44]), namely to refine when $\alpha(E)\Delta x > 1.0$ and to de-refine when $\alpha(E)\Delta x < 0.125$, where $\alpha(E)$ is the field-dependent ionization coefficient and Δx is the grid spacing. The minimum grid spacing in the simulations was $\Delta x = 1.5 \mu\text{m}$. Around the needle electrode, we enforce $\Delta x < 50 \mu\text{m}$.

3.2.3 Electron-neutral cross sections for N_2 , O_2 and H_2O

Electron-neutral collisions are the dominant process in streamer discharges, and energy-dependent probabilities of such collisions are described by cross sections. In a fluid model these cross sections are used indirectly through a Boltzmann solver to obtain electron transport coefficients (such as the mobility) and rates for electron-neutral reactions. BOLSIG+ [53] with the temporal growth model was used to obtain such data.

For most atoms and molecules, there is still quite some uncertainty in the

electron-neutral cross sections. For example, in [87] streamer simulations were compared using different cross sections sets for dry air (80% N₂, 20% O₂), and it was found that the streamer velocity could vary by about 10% when compared at the same position. Although the gas mixtures considered here consist mostly of N₂ and O₂, we here want to focus on the uncertainty in cross sections for H₂O. All simulations are therefore performed using Phelps' cross sections for N₂ and O₂ [138–140], whereas for H₂O we consider the cross section sets described below.

We emphasize that the choice of H₂O cross section sets included in our comparison was rather arbitrary, and that we probably could have included other data as well (from e.g., [141–143]). However, our goal here is simply to illustrate how much variation there will be in streamer simulations using different cross section sets. For a more extensive discussion of H₂O cross sections and their accuracy, we refer to [141, 142, 144, 145].

Kawaguchi H₂O cross sections

The cross section set of Kawaguchi *et al* [145] was compiled based on several previous sources (too many to list here), and it contains about 40 cross sections for rotational, vibrational and electronic excitations, ionization and electron attachment. With Monte Carlo swarm simulations, the authors demonstrate that their set reproduces experimental swarm measurements better than those of [142, 143, 146]. What furthermore makes this set attractive to use is that they also provide a set with an isotropic scattering model. The tabulated cross sections do not seem to be available online; we obtained them by contacting the authors directly.

Morgan and Phelps H₂O cross sections

Through lxcats.net [147], we obtained the Morgan [148] and Phelps [149] cross section sets for H₂O. For both of these, there is the following warning: “*This cross section set should not be used in Boltzmann calculations because it does not include explicitly rotational cross sections (very important in H₂O). Morgan used an analytical form for these cross sections.*” Although values for the “continuous approximation to rotation” (CAR) are given, we were not able to reconstruct a reasonable looking rotational cross section using the formulas in [150], in particular due to uncertainty in the units used. For comparison we nevertheless include these sets without rotational cross sections.

We remark that in the recently published paper by Budde *et al* [141] the lack of rotational cross sections for H₂O is extensively addressed. The authors provide a complete set containing 147 rotational cross sections, out of a total of 163 cross sections. The set is tested against swarm measurements using two two-term Boltzmann solvers, and the authors obtain good agreement. At the time of

writing, this set was not yet available on lxcat.net, so we did not include it in our comparison.

Trinita H₂O cross sections

We also obtained the Trinita set [151] through lxcat.net, which was obtained from the EEDF Boltzmann solver [152]. The cross section file includes a reference to Yousfi *et al* 1987, which we could not find, but this suggests that these cross sections could be related to the ones published later in [143].

Itikawa H₂O cross sections

The review paper by Itikawa *et al* [146, 153] provides an overview of available cross sections for H₂O together with recommendations, which are available at lxcat.net. An update of these cross sections was recently given in [154]. We want to briefly mention two caveats when using this data. First, due to the strong dipole moment of H₂O, elastic scattering is highly anisotropic and sharply peaked in the forward direction. Although a total momentum transfer cross section is provided, the cross sections cannot directly be used in a Boltzmann solver that assumes isotropic scattering, since the set also includes rotational excitations that have to be described anisotropically. A second caveat is that some of the cross sections are only given up to a certain energy (which can be as low as 5 eV) at which they are still nonzero. If such cross sections are used in a Boltzmann solver, it depends on the particular implementation how they will be extrapolated above this energy range.

Although the data of [146] should only be used with an appropriate anisotropic scattering model, we include it here in an improper way, just for comparison with the Morgan and Phelps data. For this comparison, we have removed all rotational cross sections from the Itikawa set.

Comparison of electron transport coefficients

We have used the cross section sets described above to compute electron transport coefficients using BOLSIG- [155]. Figure 3.2 shows results for a hypothetical scenario with pure H₂O gas at 1 bar and 300 K. There is considerable variation between the sets for all transport parameters, which is not that surprising since the Morgan, Phelps and Itikawa data are used in an inappropriate way, as discussed above. The Morgan data leads to a substantially higher diffusion coefficient and a rather flat mobility. The Trinita and Kawaguchi sets agree quite well in terms of the ionization coefficient. For the attachment coefficient, we find good agreement between Morgan and Kawaguchi and between Trinita and Phelps.

Figure 3.3 shows results for air with 10% H₂O. As expected, the differences in the transport coefficients are now much smaller, due to the smaller contribution

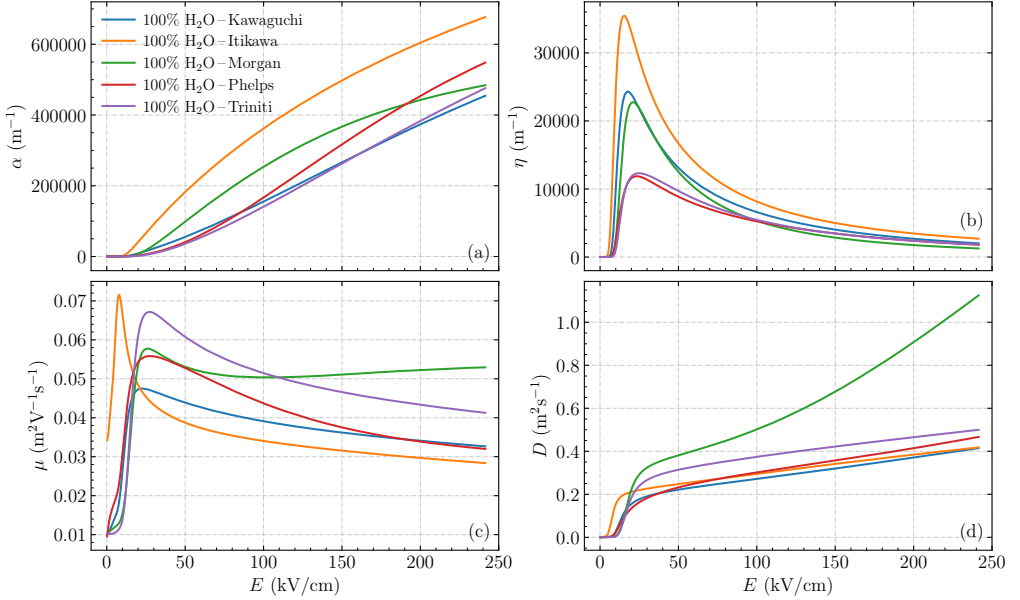
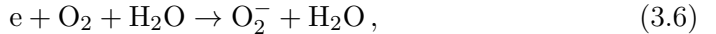
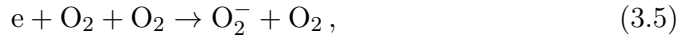


Figure 3.2: Comparison of electron transport coefficients for pure H_2O at 1 bar and 300 K using different sets of H_2O cross sections. (a) Ionization coefficient α , (b) attachment coefficient η , (c) mobility μ , and (d) diffusion coefficient D .

of the H_2O cross sections. The attachment coefficient now has a peak at low electric fields due to three-body attachment reactions:



where for this comparison reaction (3.6) was assumed to have a rate coefficient six times that of reaction (3.5). The maximum difference in the resulting attachment coefficients is about 25%, whereas the variation in the ionization coefficient is below 5%. We also computed transport data for air with 3% H_2O , but do not show it here because differences are then difficult to see.

3.2.4 Photoionization

Photoionization in humid air resembles that in dry air: excited N_2 molecules can emit photons with enough energy to non-locally ionize O_2 molecules, see e.g. [156]. We consider two approaches for modeling photoionization in humid air, which are described below. For comparison, we also briefly describe the dry air case.

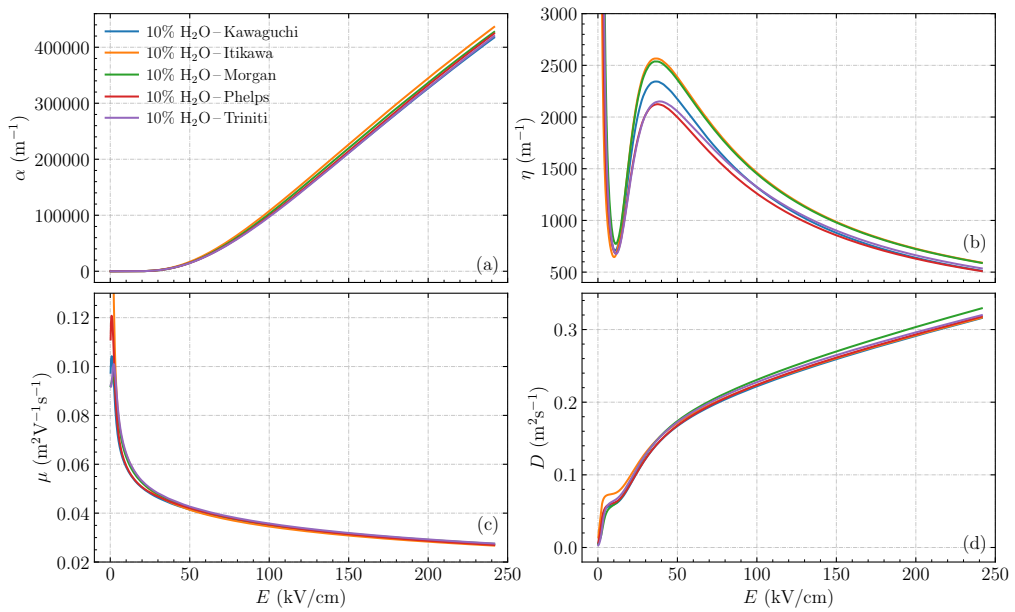


Figure 3.3: Comparison of electron transport coefficients for air with 10% H₂O at 1 bar and 300 K using different sets of H₂O cross sections. (a) Ionization coefficient α , (b) attachment coefficient η , (c) mobility μ , and (d) diffusion coefficient D .

Dry air - Zheleznyak's model

In dry air, the production I (per unit time and volume) and absorption $f(r)$ (per unit distance) of these photons is here approximated using Zheleznyak's model [35]. In this model, I is proportional to the electron impact ionization source term S_i :

$$I = \frac{p_q}{p + p_q} \xi S_i, \quad (3.7)$$

where $p_q = 40$ mbar is the quenching pressure, p the gas pressure, and ξ is a proportionality factor, which is here set to $\xi = 0.075$ as in e.g. [157, 158]. Furthermore, the absorption function is given by

$$f_{\text{air}}(r) = \frac{\exp(-k_1 p_{\text{O}_2} r) - \exp(-k_2 p_{\text{O}_2} r)}{r \ln(k_2/k_1)}, \quad (3.8)$$

where $k_1 = 0.035 \text{cm}^{-1} \text{Torr}^{-1}$, $k_2 = 2 \text{cm}^{-1} \text{Torr}^{-1}$ and p_{O_2} is the partial pressure of O_2 . We remark that what actually matters is the number density of O_2 molecules, but we here follow the usual assumption of the gas being at room temperature.

Humid air - Naidis model

Naidis [159] proposed a simple modification of Zheleznyak's model, in which water molecules lead to extra absorption:

$$f_{\text{Naidis}}(r) = \exp(-k_3 p_{\text{H}_2\text{O}} r) \times f_{\text{air}}(r), \quad (3.9)$$

where $k_3 = 0.26 \text{cm}^{-1} \text{Torr}^{-1}$. Note that with this extra term, the integral (from 0 to inf) over the absorption function is less than unity, because the photons absorbed by H_2O do not contribute to photoionization.

Humid air - Aints model

Aints *et al* [160] performed measurements on photoionization in humid air that were not consistent with equation (3.9) for small values of $k_3 p_{\text{H}_2\text{O}} r$. They therefore proposed a different absorption function which we here write as

$$f_{\text{Aints}}(r) = \frac{\exp(-K_1 r) - \exp(-K_2 r)}{r \ln(K_2/K_1)}, \quad (3.10)$$

where $K_1 = k_1 p_{\text{O}_2} + k_4 p_{\text{H}_2\text{O}}$ and $K_2 = k_2 p_{\text{O}_2} + k_5 p_{\text{H}_2\text{O}}$, with $k_4 = 0.13 \text{cm}^{-1} \text{Torr}^{-1}$ and $k_5 = 0.57 \text{cm}^{-1} \text{Torr}^{-1}$. Note that this absorption function has an integral of unity. The authors instead introduced additional quenching by H_2O in equation (3.7):

$$I_{\text{Aints}} = \left(1 + \frac{p - p_{\text{H}_2\text{O}}}{p_q} + \frac{p_{\text{H}_2\text{O}}}{p_{q,\text{H}_2\text{O}}} \right)^{-1} \xi S_i, \quad (3.11)$$

Case (% H ₂ O)	Model	λ_1	λ_2	λ_3 (mm ⁻¹)	A_1	A_2	A_3 (mm ⁻²)
0	Zheleznyak	0.830	2.19	13.4	0.0447	1.15	110
3	Naidis	1.51	3.88	32.5	0.0863	3.89	757
3	Aints	1.21	3.59	32.6	0.0963	4.37	875
10	Naidis	2.83	5.19	33.0	0.0858	3.83	697
10	Aints	1.86	4.24	33.3	0.114	5.18	1045

Table 3.2: Coefficients for the three-term Helmholtz approximations to photoionization, obtained by fitting the respective absorption functions. All coefficients have been multiplied with the respective partial pressures, so that they are given in units of m⁻¹ and m⁻².

which was fitted against their data to obtain $p_{q,\text{H}_2\text{O}} = 0.3$ Torr. We use the above expressions, but remark that the value of $p_{q,\text{H}_2\text{O}}$ is unrealistic, since gas molecules do not collide (or interact) frequently enough to warrant such a low quenching pressure.

Numerical implementation

We implement photoionization in our fluid model with the Helmholtz approach, as described in [161, 162]. We used an expansion with three Helmholtz terms of the form

$$(\nabla^2 - \lambda_i^2)S_{\text{ph}} = -A_i I, \quad (3.12)$$

where I corresponds to equation (3.7) or (3.11), and the coefficients λ_i and A_i are given in table 3.2. See e.g. Appendix A of [47] for more details about this type of expansion.

3.2.5 Chemical reactions

In addition to electron-neutral cross sections, chemical reactions are another important input data for streamer fluid simulations. They are usually collected theoretically or experimentally. However, there are often significant uncertainties in both the reaction form and the reaction rate coefficient for most reactions, see e.g. [163, 164]. Furthermore, even with a specific discharge condition, various chemistry sets can be used for fluid models, and it is unclear which set is the most suitable or which reactions are significant. For example, in [87] streamer simulations were compared using different chemistry sets for dry air (80% N₂, 20% O₂), but the results of all simulation cases were highly similar, suggesting that the ionization reactions were the dominant processes for streamer discharges.

In this work, we use different chemistry sets described below. We have made small modifications to these sets so that they are compatible with the electron-

neutral cross sections that we use. We have also included reactions to obtain the emitted light from the second positive system ($\text{N}_2(\text{C}) \rightarrow \text{N}_2(\text{B}) + h\nu$), which is responsible for most of the optical emission in air at atmospheric pressure [165]. Furthermore, we have made corrections to reactions rates when necessary. All these changes are documented in 3.5.2.

We remark that the choice of chemistry sets was rather arbitrary, with the sets obtained from recent papers for streamer simulations in dry/humid air. There are other datasets, e.g., from [166–168]. Our purpose here is simply to demonstrate how sensitive streamer simulations are to the use of different datasets.

Humid air - Malagón chemistry set

This chemistry set for streamer simulations in humid air is based on the reactions from Malagón-Romero *et al* [136], and it is listed in table 3.4. This set contains 97 chemical reactions, which can be divided into eight different processes: electron impact ionization, electron attachment, electron detachment, negative ion conversion, positive ion conversion, electron-ion recombination, ion-ion recombination, and light emission. For most reactions of ion-ion recombination, reaction products were not given.

Humid air - Starikovskiy chemistry set

This chemistry set for humid air is based on Starikovskiy *et al* [137], as given in table 3.5. The set contains only 72 chemical reactions and six processes. Compared to the Malagón chemistry set described above, it does not include electron detachment and negative ion conversion processes. Additionally, it includes a single negative ion O_2^- as compared to Malagón's which includes seven negative ions. Finally, the rate coefficient for three-body attachment with H_2O (reaction R10) is seven times that of three-body attachment with O_2 (reaction R9) rather than six times in the Malagón chemistry set. Note that for dissociative recombination of electrons with $\text{H}_3\text{O}^+(\text{H}_2\text{O})_n$ ions, the range $n = 1 - 6$ is used in this set. However, in their original cited paper [169] n only ranged from 1 to 4.

Humid air - Komuro chemistry set

This chemistry set for humid air is based on Komuro *et al* [170, 171], as listed in table 3.6. Compared to the previous two sets, this set contains many more chemical reactions (191 reactions in total) and eleven processes, resulting in some differences. First, it contains several excited species, summarized in table 3.7. Second, it contains electron dissociation reactions (R13-R16), which effectively produce neutral atoms that are needed for neutral species conversion. Third, it contains neutral species conversion as the reactions were collected for studying the behavior of OH radicals in streamer discharges in [170]. Furthermore, as stated in [171], this chemistry set was constructed to investigate the effect of

gas temperature rather than humidity. Therefore, some (important) reactions related to water cluster ions, such as the recombination reactions of electrons with $\text{H}_3\text{O}^+(\text{H}_2\text{O})_n$ ions, $n = 0 - 2$ were not taken into account.

Dry air - Guo chemistry set

This chemistry set from Guo and Teunissen [89] was constructed for streamer simulations in dry air. It contains 263 chemical reactions and twelve processes, which were primarily based on the reactions from [90, 91]. This set is not listed in 3.5.2 as it is completely the same as the one in [89]. For comparison, we obtained three other chemistry sets for dry air by extracting the reactions related to H_2O from the above three humid air chemistry sets, which were still named as Malagón, Starikovskiy and Komuro, respectively.

3.2.6 Sensitivity tests

We use so-called sensitivity tests [172] to better understand which chemical reactions are important. These tests are performed by multiplying individual reaction rate coefficients with a factor c_i for $i = 1, \dots, N_c$, using the following values: (0.0, 0.25, 0.5, 0.75). With N_r reactions, the total number of additional simulations is thus $N_c N_r$. We then pick a “quantity of interest”, here called Q , that we compare at some particular time to the case with unmodified rate coefficients Q_0 . For reaction n there are then results $Q_{n,i}$ for $i = 1, \dots, N_c$, from which we compute normalized derivatives as

$$Q'_{n,i} = \frac{1}{Q_0} \frac{Q_{n,i} - Q_0}{\Delta c}, \quad (3.13)$$

where $\Delta c = c_i - 1$. Finally, we determine the mean of the normalized derivatives

$$\mu = \sum_{i=1}^{N_c} Q'_{n,i} / N_c, \quad (3.14)$$

the mean absolute value of the normalized derivatives

$$\mu^* = \sum_{i=1}^{N_c} |Q'_{n,i}| / N_c, \quad (3.15)$$

and the sample standard deviation of the $Q'_{n,i}$

$$\sigma = \sqrt{\sum_{i=1}^{N_c} (Q'_{n,i} - \mu)^2 / (N_c - 1)}. \quad (3.16)$$

Note that there are more sophisticated ways to do sensitivity tests in which multiple coefficients are varied at the same time, see e.g. [164, 173, 174]. However, our purpose here is simply to understand which reactions are important, and not to quantify the uncertainty in results due to uncertainties in the rate coefficients.

3.3 Simulation results

Below we will study how the H₂O cross sections, the photoionization model and the chemical reaction set affect simulations of positive streamers in humid air. We will compare the following streamer properties:

- The maximum electric field at the streamer head. The location of this maximum is defined as the streamer head position.
- The velocity, obtained as the time derivative of the streamer head position.
- The optical diameter, defined as the full width at half maximum (FWHM) of the time-integrated light emission after a forward Abel transform, see e.g. [87].

3.3.1 Effect of H₂O cross sections

As described in section 3.2.3, five cross section sets for H₂O were considered, namely Kawaguchi, Itikawa, Morgan, Phelps, and Trinit. We remind the reader that rotational cross sections were not included in the Morgan and Phelps data, and that we left them out for the Itikawa data. In this section, we investigate the effect of these H₂O cross sections on positive streamers in humid air with 3% H₂O. The simulations are performed in a background field of 10 kV/cm, using the ‘dry air’ Zheleznyak photoionization model and the chemistry set of Malagón.

We first illustrate the typical time evolution in these simulations in figure 3.4, which shows the electric field and electron density using the Kawaguchi H₂O cross sections. The streamer starts from the needle electrode and accelerates downwards, with the velocity and the optical diameter increasing approximately linearly with time, from about 0.8×10^6 m/s to 2.3×10^6 m/s and from about 1.2 mm to 3.7 mm, respectively. However, the maximal electric field at the streamer head remains approximately constant at about 110 kV/cm.

Simulations with the five different H₂O cross sections are compared in figure 3.5(a), which shows the electric field and electron density profiles at $z = 50$ mm. In air with 3% H₂O, these different cross sections do not lead to obvious differences in streamer properties. This is not that surprising, as differences in the electron transport coefficients are also small with 3% H₂O, as mentioned in section 3.2.3. A more quantitative comparison of the data underlying figure 3.5(a) showed that in terms of streamer velocity and diameter, two groups can be distinguished: the Kawaguchi and Phelps cases agree well, and the Morgan, Itikawa and Trinit cases agree well, with differences between these groups of about 10% when compared at the same streamer length.

In the rest of the chapter, we will use the Kawaguchi H₂O cross sections, as they can reproduce experimental swarm measurements and because they can be used with an isotropic scattering model, see section 3.2.3.

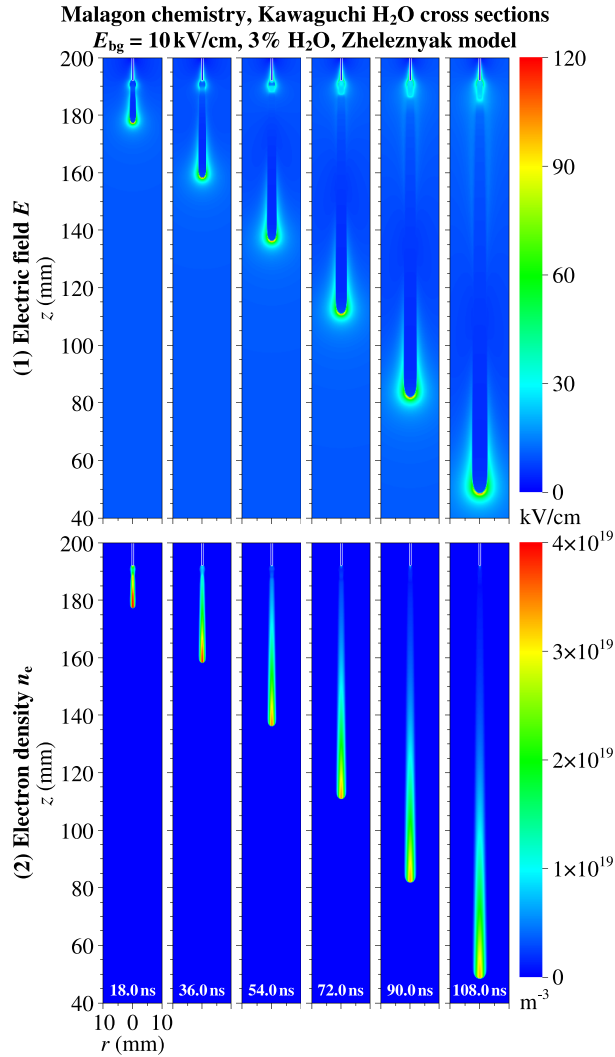


Figure 3.4: Time evolution of (1) the electric field E and (2) the electron density n_e profiles for a positive streamer in a background field of $E_{\text{bg}} = 10 \text{ kV/cm}$ in air with 3% H₂O using Kawaguchi H₂O cross sections. All panels are zoomed into the region where $0 \leq r \leq 10 \text{ mm}$ and $40 \leq z \leq 200 \text{ mm}$.

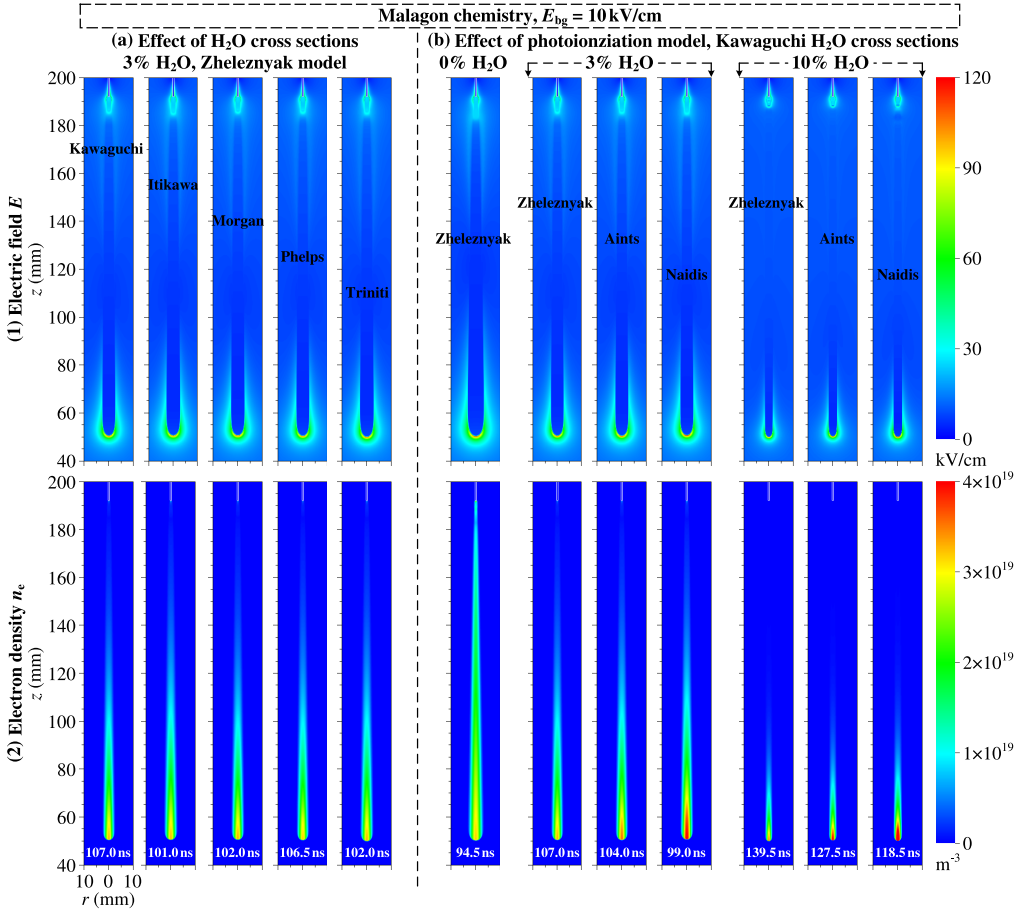


Figure 3.5: (a) Effect of H_2O cross sections on streamers in air with 3% H_2O using the Zheleznyak photoionization model, and (b) effect of the photoionization model on streamers using Kawaguchi H_2O cross sections. Shown are (1) the electric field E and (2) the electron density n_e profiles for streamers at $z = 50 \text{ mm}$.

Chemistry	Photoionization model	H ₂ O %
Guo	Zheleznyak	0
Komuro	Aints	0, 3, 10
Malagón	Aints	0, 3, 10
Starikovskiy	Aints	0, 3, 10

Table 3.3: Simulation parameters for comparison of chemical reaction sets. All simulations were performed in a background field of $E_{bg} = 10 \text{ kV/cm}$ using the Kawaguchi H₂O cross sections.

3.3.2 Effect of the photoionization model

We now compare different photoionization models to understand how important changes in photoionization due to humidity are. Three approaches are considered: the Naidis and Aints models discussed in section 3.2.4, and for comparison also the standard Zheleznyak model for dry air described in section 3.2.4. We performed simulations with these models using the Malagón chemistry, in a background field of 10 kV/cm. The figure 3.5(b) shows the electric fields and the electron densities when the streamers have reached $z = 50 \text{ mm}$, and figure 3.6 shows streamer properties as a function of z .

There is a clear effect of photoionization on E_{max} and other streamer properties. If the Zheleznyak model for dry air is used, E_{max} is almost the same for 0%, 3% and 10% H₂O, even though other streamer properties such as velocity and radius then vary significantly. With the Naidis and Aints models there is less photoionization, which leads to an increase in E_{max} of up to about 15%. Due to the higher field at the streamer tip, the electron density in the streamer channel is also higher. Furthermore, the streamer velocity is substantially higher, for example about 30% higher with the Naidis model and 10% H₂O than with the Zheleznyak model. The effect on the streamer radius is smaller, with differences of up to about 10% between the Naidis and Zheleznyak cases for 10% H₂O.

That a reduction in photoionization can lead to faster streamers was also found in previous work [87]. Perhaps this is most easily understood from the scenario in which there is a very large amount of photoionization. In such cases, the streamer will have less field enhancement, and thus become less conductive, which means that it will propagate more slowly.

3.3.3 Effect of chemical reactions

In this section we study the effect of chemical reactions on positive streamer propagation in humid air. We used the chemistry sets described in section 3.2.5 with varying humidity levels to perform a total of ten streamer simulations, for which the conditions are summarized in table 3.3. Figure 3.7 shows the electron density and the electric field when the streamers have reached $z = 50 \text{ mm}$, and

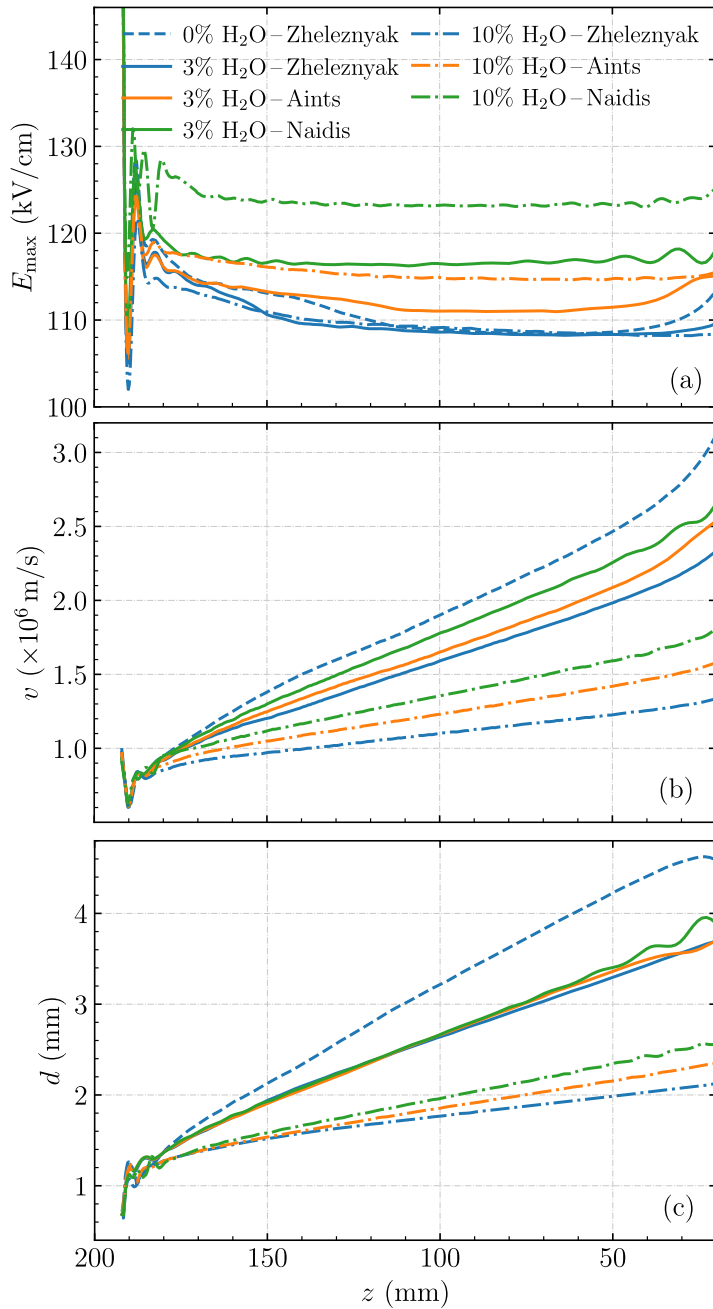


Figure 3.6: Effect of the photoionization model on positive streamers in $E_{\text{bg}} = 10$ kV/cm in air with different humidities (0%, 3% and 10%) using Kawaguchi H₂O cross sections. Streamer properties of (a) the maximal electric field E_{\max} , (b) streamer velocity v , and (c) optical diameter d versus the streamer head position z .

figure 3.8 shows streamer properties as a function of position.

As a first test, we compare results in dry air (0% H₂O), since the chemistry sets also differ in the included reactions for oxygen and nitrogen species. Results with the Komuro and Malagón chemistries agree very well in this case, whereas the Starikovskiy and Guo chemistries lead to slower streamers. At $z = 50$ mm, the Starikovskiy case is about 7% slower, whereas the Guo case is about 12% slower. The differences in streamer diameter are approximately the same, with the slower streamers having a smaller diameter. The variation in the maximum field at the streamer head is much smaller between these cases.

Next, we compare results with the Komuro, Malagón and Starikovskiy chemistries with 3% and 10% H₂O. The differences in streamer velocity then become larger, with the Komuro case leading to the fastest streamers and the Starikovskiy case leading to the slowest ones. With 3% H₂O, the Malagón case is about 15% slower than the Komuro case at $z = 50$ mm, and the Starikovskiy case is about 35% slower. With 10% H₂O, these differences are 15% and 50%, respectively. The differences in streamer diameter are again approximately the same as those in the velocity, and the maximum electric at the streamer head varies by less than 2% at $z = 50$ mm.

Regardless of the particular chemistry, an increase in the percentage of H₂O leads to slower streamers with a smaller radius, as was also found in previous work [136, 137]. In the results presented here, streamers have propagated for about a hundred ns. On such short timescales, the main effect of a chemistry on streamer propagation is through reactions that affect the electron density inside the streamer channel, such as electron attachment, detachment and electron-ion recombination reactions. Below, in section 3.3.4, we present a sensitivity analysis to identify which reactions in each of the chemistry sets are most important in this respect.

3.3.4 Sensitivity analysis of chemical reactions

Using the method described in section 3.2.6, we have studied the sensitivity of streamer simulations to individual chemical reactions. The total number of electrons N_e at $t = 100$ ns was used as the “quantity of interest”. We exclude electron impact ionization reactions from this analysis; their effect is discussed in appendix 3.5.1. All simulations were performed in air containing 3% H₂O, using a background field of 10 kV/cm, the Aints photoionization model and the Kawaguchi cross sections for H₂O.

In figures 3.9–3.11, the ten most important reactions from the Komuro, Malagón and Starikovskiy chemistry sets are shown. ‘Most important’ is here defined as those reactions that lead to largest μ^* (see equation (3.15)), which is an indication of the relative change in the quantity of interest with respect to a change in the reaction rate coefficient.

Almost all of the important reactions decrease N_e , as indicated by the red

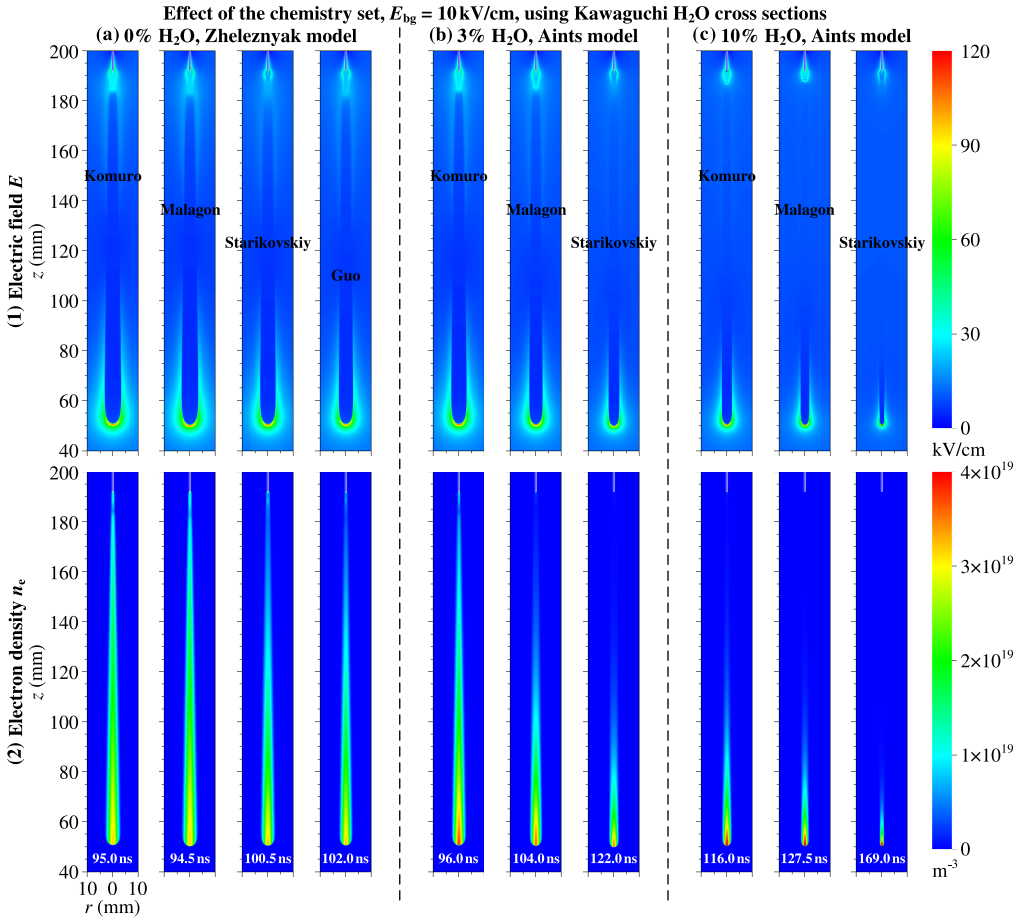


Figure 3.7: Effect of the chemistry set on positive streamers in $E_{bg} = 10 \text{ kV/cm}$ in air with different humidities (0%, 3% and 10%) using Kawaguchi H_2O cross sections. Shown are (1) the electric field E and (2) the electron density n_e profiles for streamers at $z = 50 \text{ mm}$.

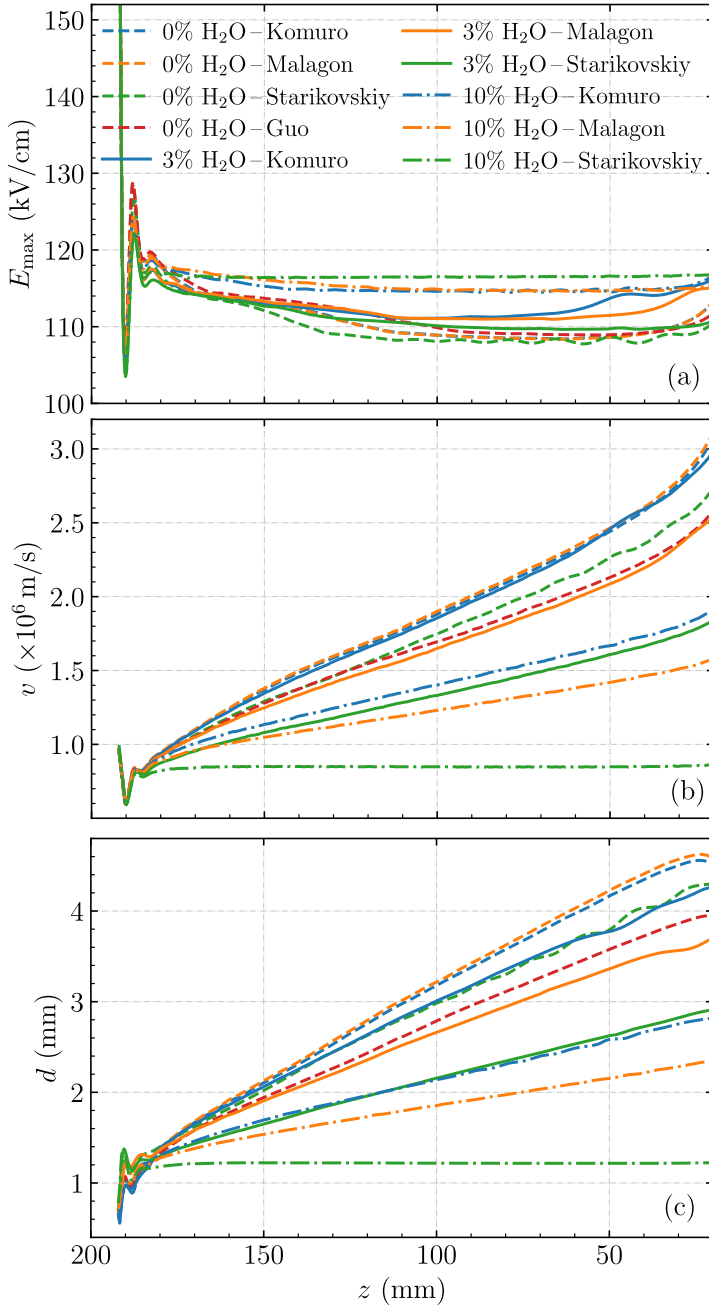


Figure 3.8: Effect of the chemistry set on positive streamers in $E_{\text{bg}} = 10$ kV/cm in air with different humidities (0%, 3% and 10%) using Kawaguchi H₂O cross sections. Streamer properties of (a) the maximal electric field E_{\max} , (b) streamer velocity v , and (c) optical diameter d versus the streamer head position z .

color in the bar plots. The two three-body attachment reactions given by equations (3.5–3.6) are about equally important for all considered chemistries. However, there is a major difference in the importance of water clusters around positive ions. In the Komuro chemistry, the formation of a single cluster $\text{O}_2^+ + \text{H}_2\text{O} + \text{M} \rightarrow \text{O}_2^+(\text{H}_2\text{O}) + \text{M}$ and $\text{O}_4^+ + \text{H}_2\text{O} \rightarrow \text{O}_2^+(\text{H}_2\text{O}) + \text{O}_2$ are included, but these reactions have no strong effect on the later discharge evolution. In contrast, water clusters play a very important role in the Malagón and Starikovskiy chemistries. The Malagón chemistry includes reactions up to the formation of $\text{H}_3\text{O}^+(\text{H}_2\text{O})_3$, whereas the Starikovskiy includes reactions up to $\text{H}_3\text{O}^+(\text{H}_2\text{O})_6$. For both chemistries, the recombination of electrons with these respective clusters is the reaction with the highest sensitivity.

The standard deviations of the ‘sensitivities’, as defined by equation (3.16), are given by the numbers next to the bars in figures 3.9–3.11. Note that there are several reactions related to water clusters that have a large standard deviation. This is caused by the following phenomenon: if there is a chain of reactions (as there is for water cluster formation), the simulation might not be sensitive to changes in the rate of one reaction in the chain. But if one reaction in the chain is fully disabled, the whole chain is stopped, which has a large effect on the result. In our tests, we include such a ‘disabling’ of reactions (namely by multiplying the rate coefficient by zero), which therefore leads to the large σ values.

Sensitivity analysis can be a useful tool for reducing the number of reactions in a set. If we are only interested in the total number of electrons N_e at 100 ns, our results show that the effect of humidity in the Komuro chemistry can be described by one three-body attachment reaction. For the Malagón and Starikovskiy chemistries, the formation of water clusters around positive ions and the consecutive recombination of electrons with these clusters is also important. Since electrons predominantly recombine with the largest clusters, it might be possible to simplify the chemistry by leaving out the intermediate states.

3.4 Conclusions

We have studied how strongly simulations of positive streamers in humid air depend on the choice of input data. We considered different cross section sets for H_2O , different approximations for photoionization in humid air, and different chemical reaction sets. Simulations were performed in air containing a mole fraction of 0%, 3% or 10% H_2O at 300 K and 1 bar, using an axisymmetric fluid model. Our focus was on the streamer propagation stage, and time scales of up to about 100 ns were considered. The underlying motivation was to understand to what extent uncertainty about input data can be resolved by experimentally studying streamers in humid air.

When different H_2O cross sections are used, the most significant differences are in the resulting electron attachment coefficient. We performed simulations

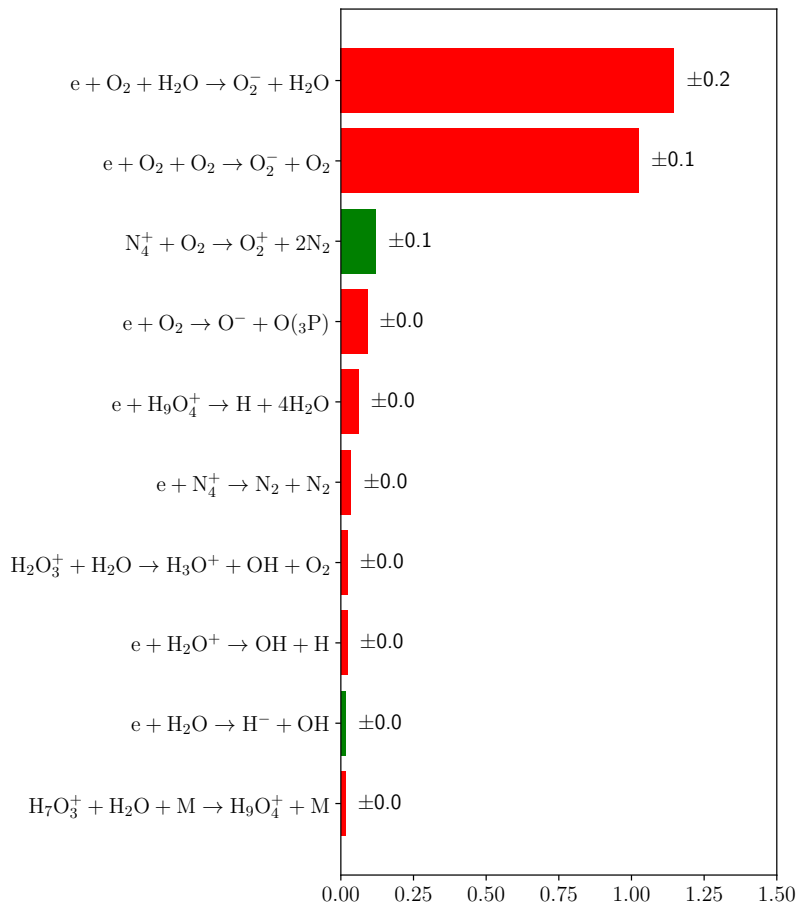


Figure 3.9: Sensitivity analysis of the Komuro chemistry. The effect of individual reactions on the total number of electrons at $t = 100$ ns was determined using the method described in section 3.2.6. The bars indicate the magnitude of the derivative μ^* , see equation (3.15), and their color indicates the sign of the derivative (red: negative, green: positive). The numbers next to the bars indicate the standard deviations σ , see equation (3.16).

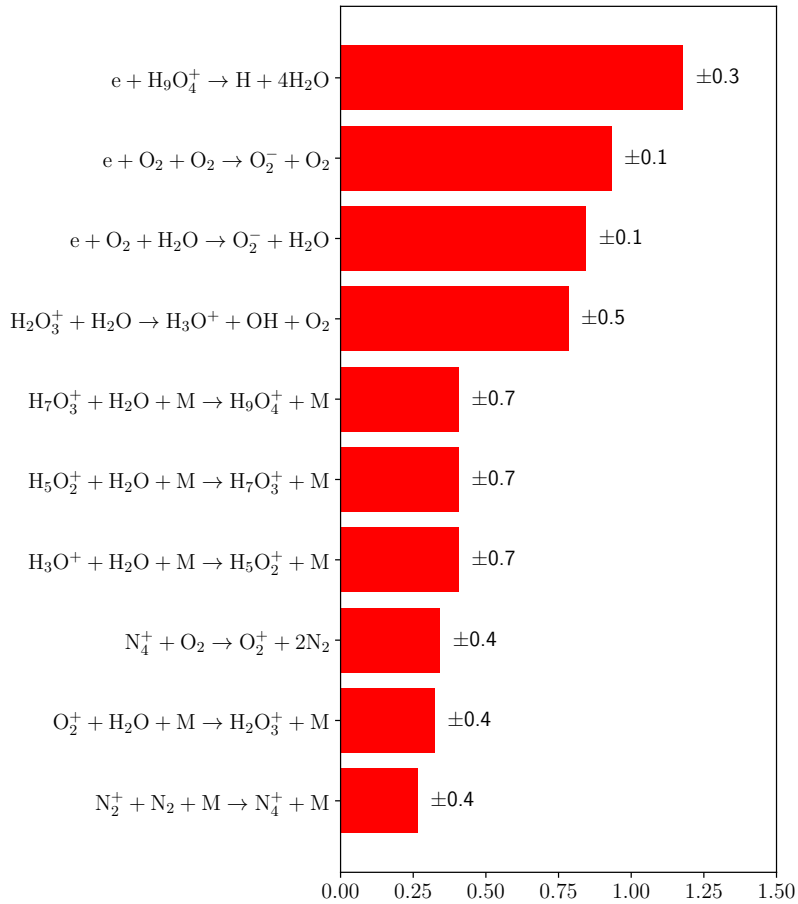


Figure 3.10: Sensitivity analysis of the Malagón chemistry, analogous to figure 3.9.

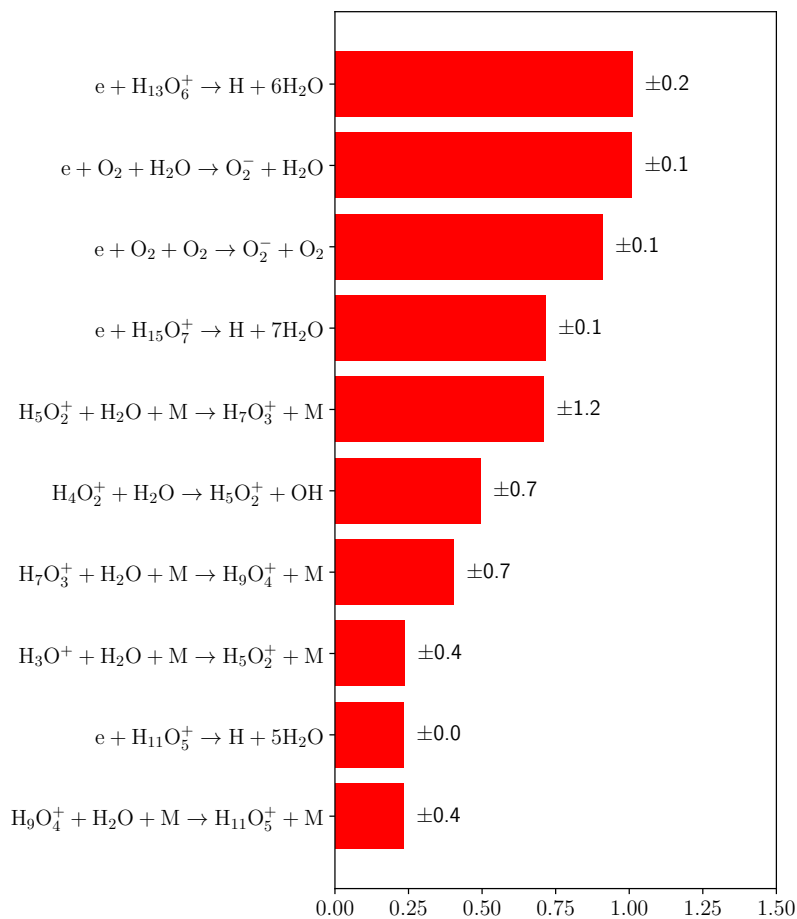


Figure 3.11: Sensitivity analysis of the Starikovskiy chemistry, analogous to figure 3.9.

with these cross section in air containing 3% H₂O, and found relatively minor differences in streamer properties, with the variation in streamer velocity below 10%. We did not use all cross sections sets properly, as we had to leave out rotational cross sections from some of the sets, and because one of the sets is only supposed to be used with an anisotropic scattering model.

In humid air, there is less photoionization than in dry air. We compared two photoionization models, one by Naidis and by Aints, with the standard Zheleznyak model for dry air. With less photoionization, the streamer has a higher maximum electric field at its tip, leading to a higher electron density in the channel and (in our simulations) also a higher velocity. The effect of different photoionization models on the streamer velocity was comparable to the effect of using different H₂O cross sections.

Finally, we performed simulations with three different sets of chemical reactions for humid air, for comparison also including one reaction set for dry air. We considered relatively short time scales, and our focus was on the effect on streamer properties. The sets differed significantly in the formation of water clusters around positive ions, which play an important role in electron-ion recombination. This led to differences of up to a factor three in streamer velocity for 10% H₂O, whereas the differences in velocity in dry air are only about 10-20%. Furthermore, we identified the most important chemical reactions with a sensitivity analysis.

In future work, it would be interesting to experimentally study streamers in air with a high humidity level, e.g. a mole fraction of 10% H₂O or more. This could shed light on the importance of water clusters and their effect on the conductivity of streamer channels.

3.5 Appendix

3.5.1 Effect of ionization reactions

In our analysis, we have focused on the effect of humidity-related input data. However, the presented simulation results will also be sensitive to the cross sections used for N₂ and O₂, of which the most significant effect will probably be changes in the ionization coefficient α . To get an idea of the sensitivity of our simulations to such changes, we have performed simulations in which all ionization reactions were multiplied by a factor k_{ion} while all other reactions were kept unchanged, as was also done in [175]. We modified k_{ion} in the range (1.0, 0.9, 0.8, 0.7, 0.6, 0.5), where $k_{\text{ion}} = 1.0$ corresponds to the unchanged α . The simulations were performed in a background field of 14 kV/cm using the Malagón chemistry.

Figure 3.12 shows the electric field and the electron density for different k_{ion} values when the streamer has propagated up to $z = 50$ mm. From these results, we conclude that the use of different N₂ and O₂ cross sections, resulting in a different ionization coefficient α , could have the following effects:

- The streamer velocity seems to be approximately proportional to α
- The electron density in the streamer channel is also approximately proportional to α (in the figure this is hard to see due to the clipping of color values)
- The streamer radius and the maximal electric field at the streamer tip are both much less sensitive to α .

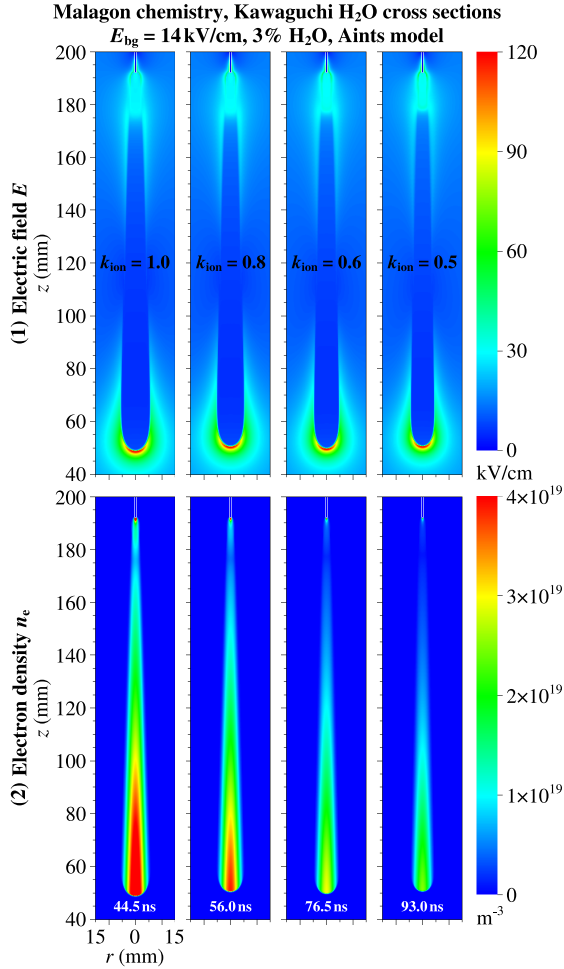


Figure 3.12: Effect of the ionization rate on positive streamers in $E_{\text{bg}} = 14 \text{ kV/cm}$ in air with 3% H₂O using the Aints photoionization model. Shown are (1) the electric field E and (2) the electron density n_e profiles for streamers at $z = 50 \text{ mm}$. All panels are zoomed in into the region where $0 \leq r \leq 15 \text{ mm}$ and $40 \leq z \leq 200 \text{ mm}$.

3.5.2 Three chemistry sets for humid air

Tables 3.4, 3.5 and 3.6 show three (Malagón, Starikovskiy, and Komuro) chemistry sets for humid air used in the chapter. Comments for each set are appended at the end of each table. Table 3.7 lists the excited states of N_2 , O_2 and H_2O used in the Komuro chemistry set, with their activation energies.

Table 3.4: The chemistry set for humid air from Malagón-Romero *et al* [136]. Reaction rate coefficients are in units of $cm^3 s^{-1}$ and $cm^6 s^{-1}$ for two-body and three-body reactions, respectively. The symbol M denotes a neutral molecule (either N_2 , O_2 or H_2O). k_B is the Boltzmann constant. $T(K)$ and $T_e(K)$ are gas and electron temperatures, respectively.

No.	Reaction	Reaction rate coefficient
(1) Electron impact ionization		
R1	$e + N_2 \rightarrow 2e + N_2^+$	$f_1(E/N)$
R2	$e + O_2 \rightarrow 2e + O_2^+$	$f_2(E/N)$
R3	$e + H_2O \rightarrow 2e + H_2O^+$	$f_3(E/N)$
R4	$e + H_2O \rightarrow 2e + H^+ + OH$	$f_4(E/N)$
R5	$e + H_2O \rightarrow 2e + OH^+ + H$	$f_5(E/N)$
R6	$e + H_2O \rightarrow 2e + O^+ + H_2$	$f_6(E/N)$
R7	$e + H_2O \rightarrow 2e + H_2^+ + O$	$f_7(E/N)$
R8	$e + H_2O \rightarrow 3e + O^{2+} + H_2$	$f_8(E/N)$
(2) Electron attachment		
R9	$e + O_2 + O_2 \rightarrow O_2^- + O_2$	$f_9(E/N)$
R10	$e + O_2 \rightarrow O^- + O$	$f_{10}(E/N)$
R11	$e + H_2O \rightarrow H^- + OH$	$f_{11}(E/N)$
R12	$e + H_2O \rightarrow OH^- + H$	$f_{12}(E/N)$
R13	$e + H_2O \rightarrow O^- + H_2$	$f_{13}(E/N)$
R14	$e + O_2 + H_2O \rightarrow O_2^- + H_2O$	$f_{14}(E/N) = 6 \times f_9(E/N)$
(3) Electron detachment		
R15	$O_2^- + M \rightarrow e + O_2 + M$	$1.24 \times 10^{-11} \exp(-(\frac{179}{8.8+E/N})^2)$
R16	$O^- + N_2 \rightarrow e + N_2O$	$1.16 \times 10^{-12} \exp(-(\frac{48.9}{11+E/N})^2)$
R17	$H^- + O_2 \rightarrow e + HO_2$	1.2×10^{-9}
(4) Negative ion conversion		
R18	$O^- + O_2 + M \rightarrow O_3^- + M$	$1.1 \times 10^{-30} \exp(-(\frac{E/N}{65})^2)$
R19	$O^- + O_2 \rightarrow O_2^- + O$	$6.96 \times 10^{-11} \exp(-(\frac{198}{5.6+E/N})^2)$
R20	$O^- + H_2O \rightarrow OH^- + OH$	6.0×10^{-13}
R21	$H^- + O_2 \rightarrow O^- + OH$	1.0×10^{-11}
R22	$H^- + O_2 \rightarrow O_2^- + H$	1.0×10^{-11}
R23	$H^- + H_2O \rightarrow OH^- + H_2$	3.8×10^{-9}
R24	$O_2^- + H_2O + M \rightarrow O_2^-(H_2O) + M$	2.2×10^{-28}
R25	$O_2^-(H_2O) + H_2O + M \rightarrow O_2^-(H_2O)_2 + M$	5.0×10^{-28}

Table 3.4: (Continued.)

No.	Reaction	Reaction rate coefficient
R26	$O_2^-(H_2O)_2 + H_2O + M \rightarrow O_2^-(H_2O)_3 + M$	5.0×10^{-29}
R27	$O_2^-(H_2O) + M \rightarrow O_2^- + H_2O + M$	$5.91 \times 10^{-9} \exp\left(-\frac{1.28 \times 10^{-19}}{k_B(T + \frac{E/N}{0.18})}\right)$
R28	$O_2^-(H_2O)_2 + M \rightarrow O_2^-(H_2O) + H_2O + M$	$1.34 \times 10^{-8} \exp\left(-\frac{5.8 \times 10^{-20}}{k_B(T + \frac{E/N}{0.18})}\right)$
R29	$O_2^-(H_2O)_3 + M \rightarrow O_2^-(H_2O)_2 + H_2O + M$	$1.34 \times 10^{-9} \exp\left(-\frac{4.49 \times 10^{-20}}{k_B(T + \frac{E/N}{0.18})}\right)$
R30	$O_2^-(H_2O) + M \rightarrow O_2^- + H_2O + M$	$5.91 \times 10^{-9} \exp\left(-\frac{1.28 \times 10^{-19}}{k_B(T + \frac{E/N}{0.18})}\right)$
R31	$O_2^-(H_2O)_2 + M \rightarrow O_2^-(H_2O) + H_2O + M$	$1.34 \times 10^{-8} \exp\left(-\frac{5.8 \times 10^{-20}}{k_B(T + \frac{E/N}{0.18})}\right)$
R32	$O_2^-(H_2O)_3 + M \rightarrow O_2^-(H_2O)_2 + H_2O + M$	$1.34 \times 10^{-9} \exp\left(-\frac{4.49 \times 10^{-20}}{k_B(T + \frac{E/N}{0.18})}\right)$
(5) Positive ion conversion		
R33	$N_2^+ + N_2 + M \rightarrow N_4^+ + M$	$5.0 \times 10^{-29} \left(\frac{300}{T}\right)^2$
R34	$N_4^+ + O_2 \rightarrow O_2^+ + 2N_2$	2.5×10^{-10}
R35	$O_2^+ + O_2 + M \rightarrow O_4^+ + M$	$2.4 \times 10^{-30} \left(\frac{300}{T}\right)^3$
R36	$O_2^+ + H_2O + M \rightarrow O_2^+(H_2O) + M$	2.6×10^{-28}
R37	$O_2^+(H_2O) + H_2O \rightarrow H_3O^+ + OH + O_2$	3.0×10^{-10}
R38	$H_3O^+ + H_2O + M \rightarrow H_3O^+(H_2O) + M$	3.0×10^{-27}
R39	$H_3O^+(H_2O) + H_2O + M \rightarrow H_3O^+(H_2O)_2 + M$	3.0×10^{-27}
R40	$H_3O^+(H_2O)_2 + H_2O + M \rightarrow H_3O^+(H_2O)_3 + M$	3.0×10^{-27}
(6) Electron-ion recombination		
R41	$e + O_4^+ \rightarrow O_2 + O_2$	$1.4 \times 10^{-6} \left(\frac{300}{T_e}\right)^{0.5}$
R42	$e + H_3O^+(H_2O)_3 \rightarrow H + 4H_2O$	$6.5 \times 10^{-6} \left(\frac{300}{T_e}\right)^{0.5}$
(7) Ion-ion recombination		
R43	$N_2^+ + O^- \rightarrow 2N + O$	1.0×10^{-7}
R44	$N_2^+ + O_2^- \rightarrow 2N + O_2$	1.0×10^{-7}
R45	$N_2^+ + O_3^- \rightarrow 2N + O_3$	1.0×10^{-7}
R46	$N_2^+ + O_2^-(H_2O) \rightarrow \text{neutrals}$	1.0×10^{-7}
R47	$N_2^+ + O_2^-(H_2O)_2 \rightarrow \text{neutrals}$	1.0×10^{-7}
R48	$N_2^+ + O_2^-(H_2O)_3 \rightarrow \text{neutrals}$	1.0×10^{-7}
R49	$N_4^+ + O^- \rightarrow 2N_2 + O$	1.0×10^{-7}
R50	$N_4^+ + O_2^- \rightarrow 2N_2 + O_2$	1.0×10^{-7}
R51	$N_4^+ + O_3^- \rightarrow 2N_2 + O_3$	1.0×10^{-7}
R52	$N_4^+ + O_2^-(H_2O) \rightarrow \text{neutrals}$	1.0×10^{-7}
R53	$N_4^+ + O_2^-(H_2O)_2 \rightarrow \text{neutrals}$	1.0×10^{-7}
R54	$N_4^+ + O_2^-(H_2O)_3 \rightarrow \text{neutrals}$	1.0×10^{-7}
R55	$O_2^+ + O^- \rightarrow 2O + O$	1.0×10^{-7}
R56	$O_2^+ + O_2^- \rightarrow 2O + O_2$	1.0×10^{-7}
R57	$O_2^+ + O_3^- \rightarrow 2O + O_3$	1.0×10^{-7}
R58	$O_2^+ + O_2^-(H_2O) \rightarrow \text{neutrals}$	1.0×10^{-7}
R59	$O_2^+ + O_2^-(H_2O)_2 \rightarrow \text{neutrals}$	1.0×10^{-7}
R60	$O_2^+ + O_2^-(H_2O)_3 \rightarrow \text{neutrals}$	1.0×10^{-7}
R61	$O_4^+ + O^- \rightarrow 2O_2 + O$	1.0×10^{-7}
R62	$O_4^+ + O_2^- \rightarrow 2O_2 + O_2$	1.0×10^{-7}
R63	$O_4^+ + O_3^- \rightarrow 2O_2 + O_3$	1.0×10^{-7}
R64	$O_4^+ + O_2^-(H_2O) \rightarrow \text{neutrals}$	1.0×10^{-7}
R65	$O_4^+ + O_2^-(H_2O)_2 \rightarrow \text{neutrals}$	1.0×10^{-7}
R66	$O_4^+ + O_2^-(H_2O)_3 \rightarrow \text{neutrals}$	1.0×10^{-7}
R67	$O_2^+(H_2O) + O^- \rightarrow \text{neutrals}$	1.0×10^{-7}

Table 3.4: (Continued.)

No.	Reaction	Reaction rate coefficient ($\text{cm}^3 \text{s}^{-1}$ or $\text{cm}^6 \text{s}^{-1}$)
R68	$\text{O}_2^+(\text{H}_2\text{O}) + \text{O}_2^- \rightarrow \text{neutrals}$	1.0×10^{-7}
R69	$\text{O}_2^+(\text{H}_2\text{O}) + \text{O}_3^- \rightarrow \text{neutrals}$	1.0×10^{-7}
R70	$\text{O}_2^+(\text{H}_2\text{O}) + \text{O}_2^-(\text{H}_2\text{O}) \rightarrow \text{neutrals}$	1.0×10^{-7}
R71	$\text{O}_2^+(\text{H}_2\text{O}) + \text{O}_2^-(\text{H}_2\text{O})_2 \rightarrow \text{neutrals}$	1.0×10^{-7}
R72	$\text{O}_2^+(\text{H}_2\text{O}) + \text{O}_2^-(\text{H}_2\text{O})_3 \rightarrow \text{neutrals}$	1.0×10^{-7}
R73	$\text{H}_3\text{O}^+ + \text{O}^- \rightarrow \text{neutrals}$	1.0×10^{-7}
R74	$\text{H}_3\text{O}^+ + \text{O}_2^- \rightarrow \text{neutrals}$	1.0×10^{-7}
R75	$\text{H}_3\text{O}^+ + \text{O}_3^- \rightarrow \text{neutrals}$	1.0×10^{-7}
R76	$\text{H}_3\text{O}^+ + \text{O}_2^-(\text{H}_2\text{O}) \rightarrow \text{neutrals}$	1.0×10^{-7}
R77	$\text{H}_3\text{O}^+ + \text{O}_2^-(\text{H}_2\text{O})_2 \rightarrow \text{neutrals}$	1.0×10^{-7}
R78	$\text{H}_3\text{O}^+ + \text{O}_2^-(\text{H}_2\text{O})_3 \rightarrow \text{neutrals}$	1.0×10^{-7}
R79	$\text{H}_3\text{O}^+(\text{H}_2\text{O}) + \text{O}^- \rightarrow \text{neutrals}$	1.0×10^{-7}
R80	$\text{H}_3\text{O}^+(\text{H}_2\text{O}) + \text{O}_2^- \rightarrow \text{neutrals}$	1.0×10^{-7}
R81	$\text{H}_3\text{O}^+(\text{H}_2\text{O}) + \text{O}_3^- \rightarrow \text{neutrals}$	1.0×10^{-7}
R82	$\text{H}_3\text{O}^+(\text{H}_2\text{O}) + \text{O}_2^-(\text{H}_2\text{O}) \rightarrow \text{neutrals}$	1.0×10^{-7}
R83	$\text{H}_3\text{O}^+(\text{H}_2\text{O}) + \text{O}_2^-(\text{H}_2\text{O})_2 \rightarrow \text{neutrals}$	1.0×10^{-7}
R84	$\text{H}_3\text{O}^+(\text{H}_2\text{O}) + \text{O}_2^-(\text{H}_2\text{O})_3 \rightarrow \text{neutrals}$	1.0×10^{-7}
R85	$\text{H}_3\text{O}^+(\text{H}_2\text{O})_2 + \text{O}^- \rightarrow \text{neutrals}$	1.0×10^{-7}
R86	$\text{H}_3\text{O}^+(\text{H}_2\text{O})_2 + \text{O}_2^- \rightarrow \text{neutrals}$	1.0×10^{-7}
R87	$\text{H}_3\text{O}^+(\text{H}_2\text{O})_2 + \text{O}_3^- \rightarrow \text{neutrals}$	1.0×10^{-7}
R88	$\text{H}_3\text{O}^+(\text{H}_2\text{O})_2 + \text{O}_2^-(\text{H}_2\text{O}) \rightarrow \text{neutrals}$	1.0×10^{-7}
R89	$\text{H}_3\text{O}^+(\text{H}_2\text{O})_2 + \text{O}_2^-(\text{H}_2\text{O})_2 \rightarrow \text{neutrals}$	1.0×10^{-7}
R90	$\text{H}_3\text{O}^+(\text{H}_2\text{O})_2 + \text{O}_2^-(\text{H}_2\text{O})_3 \rightarrow \text{neutrals}$	1.0×10^{-7}
R91	$\text{H}_3\text{O}^+(\text{H}_2\text{O})_3 + \text{O}^- \rightarrow \text{neutrals}$	1.0×10^{-7}
R92	$\text{H}_3\text{O}^+(\text{H}_2\text{O})_3 + \text{O}_2^- \rightarrow \text{neutrals}$	1.0×10^{-7}
R93	$\text{H}_3\text{O}^+(\text{H}_2\text{O})_3 + \text{O}_3^- \rightarrow \text{neutrals}$	1.0×10^{-7}
R94	$\text{H}_3\text{O}^+(\text{H}_2\text{O})_3 + \text{O}_2^-(\text{H}_2\text{O}) \rightarrow \text{neutrals}$	1.0×10^{-7}
R95	$\text{H}_3\text{O}^+(\text{H}_2\text{O})_3 + \text{O}_2^-(\text{H}_2\text{O})_2 \rightarrow \text{neutrals}$	1.0×10^{-7}
R96	$\text{H}_3\text{O}^+(\text{H}_2\text{O})_3 + \text{O}_2^-(\text{H}_2\text{O})_3 \rightarrow \text{neutrals}$	1.0×10^{-7}
(8) Light emission		
R97	$e + \text{N}_2 \rightarrow e + \text{N}_2(\text{C})$	$f_{15}(E/N)$
R98	$\text{N}_2(\text{C}) + \text{N}_2 \rightarrow \text{N}_2 + \text{N}_2$	1.3×10^{-11}
R99	$\text{N}_2(\text{C}) + \text{O}_2 \rightarrow \text{N}_2 + \text{O}_2$	3.0×10^{-10}
R100	$\text{N}_2(\text{C}) \rightarrow \text{N}_2(\text{B}) + h\nu$	$1/(42 \text{ ns})$

1. In [136], a total ionization reaction like R3 was used for H_2O .

Here more ionization reaction channels (R3–R8) are included when using Kawaguchi H_2O cross sections, whereas for other cross section sets only R3 is used.

2. In [136], rate coefficients for R30 and R31 were $5.0 \times 10^{-29} (\frac{300}{T})^3$ and $2.5 \times 10^{-10} (\frac{300}{T})^3$, respectively. We check with their cited paper [176] and have corrected them to $5.0 \times 10^{-29} (\frac{300}{T})^2$ and 2.5×10^{-10} , respectively.

3. R94–R97 are included for light emission, which were taken from [177].

Table 3.5: The chemistry set for humid air from Starikovskiy *et al* [137]. T (K) and T_e (K) are gas and electron temperatures, respectively.

No.	Reaction	Reaction rate coefficient
(1) Electron impact ionization		
R1	$e + N_2 \rightarrow 2e + N_2^+$	$f_1(E/N)$
R2	$e + O_2 \rightarrow 2e + O_2^+$	$f_2(E/N)$
R3	$e + H_2O \rightarrow 2e + H_2O^+$	$f_3(E/N)$
R4	$e + H_2O \rightarrow 2e + H^+ + OH$	$f_4(E/N)$
R5	$e + H_2O \rightarrow 2e + OH^+ + H$	$f_5(E/N)$
R6	$e + H_2O \rightarrow 2e + O^+ + H_2$	$f_6(E/N)$
R7	$e + H_2O \rightarrow 2e + H_2^+ + O$	$f_7(E/N)$
R8	$e + H_2O \rightarrow 3e + O^{2+} + H_2$	$f_8(E/N)$
(2) Electron attachment		
R9	$e + O_2 + O_2 \rightarrow O_2^- + O_2$	$f_9(E/N)$
R10	$e + O_2 + H_2O \rightarrow O_2^- + H_2O$	$f_{10}(E/N) = 7 \times f_9(E/N)$
(3) Positive ion conversion		
R11	$N_2^+ + N_2 + M \rightarrow N_4^+ + M$	5.0×10^{-29}
R12	$N_2^+ + O_2 \rightarrow O_2^+ + N_2$	6.0×10^{-11}
R13	$N_2^+ + H_2O \rightarrow H_2O^+ + N_2$	$2.3 \times 10^{-9} (\frac{300}{T})^{0.5}$
R14	$N_2^+ + H_2O \rightarrow N_2H^+ + OH$	$5.0 \times 10^{-10} (\frac{300}{T})^{0.5}$
R15	$N_4^+ + O_2 \rightarrow O_2^+ + 2N_2$	2.5×10^{-10}
R16	$N_4^+ + H_2O \rightarrow H_2O^+ + 2N_2$	$2.4 \times 10^{-9} (\frac{300}{T})^{0.5}$
R17	$O_2^+ + N_2 + M \rightarrow N_2O_2^+ + M$	9.0×10^{-31}
R18	$O_2^+ + O_2 + M \rightarrow O_4^+ + M$	2.4×10^{-30}
R19	$O_2^+ + H_2O + M \rightarrow O_2^+(H_2O) + M$	$2.6 \times 10^{-28} (\frac{300}{T})^4$
R20	$O_4^+ + H_2O \rightarrow O_2^+(H_2O) + O_2$	1.7×10^{-9}
R21	$N_2H^+ + H_2O \rightarrow H_3O^+ + N_2$	$2.6 \times 10^{-9} (\frac{300}{T})^{0.5}$
R22	$N_2O_2^+ + N_2 \rightarrow O_2^+ + 2N_2$	4.3×10^{-10}
R23	$N_2O_2^+ + O_2 \rightarrow O_4^+ + N_2$	1.0×10^{-9}
R24	$H_2O^+ + O_2 \rightarrow O_2^+ + H_2O$	4.1×10^{-10}
R25	$H_2O^+ + H_2O \rightarrow H_3O^+ + OH$	$2.1 \times 10^{-9} (\frac{300}{T})^{0.5}$
R26	$O_2^+(H_2O) + H_2O \rightarrow H_3O^+ + OH + O_2$	3.0×10^{-10}
R27	$O_2^+(H_2O) + H_2O \rightarrow H_3O^+(OH) + O_2$	1.9×10^{-9}
R28	$H_3O^+(OH) + H_2O \rightarrow H_3O^+(H_2O) + OH$	3.0×10^{-9}
R29	$H_3O^+ + H_2O + M \rightarrow H_3O^+(H_2O) + M$	$3.2 \times 10^{-27} (\frac{300}{T})^4$
R30	$H_3O^+(H_2O) + H_2O + M \rightarrow H_3O^+(H_2O)_2 + M$	$7.4 \times 10^{-27} (\frac{300}{T})^{7.5}$
R31	$H_3O^+(H_2O)_2 + H_2O + M \rightarrow H_3O^+(H_2O)_3 + M$	$2.5 \times 10^{-27} (\frac{300}{T})^{8.1}$
R32	$H_3O^+(H_2O)_3 + H_2O + M \rightarrow H_3O^+(H_2O)_4 + M$	$3.3 \times 10^{-28} (\frac{300}{T})^{14}$
R33	$H_3O^+(H_2O)_4 + H_2O + M \rightarrow H_3O^+(H_2O)_5 + M$	$4.0 \times 10^{-29} (\frac{300}{T})^{15.3}$
R34	$H_3O^+(H_2O)_5 + H_2O + M \rightarrow H_3O^+(H_2O)_6 + M$	$4.5 \times 10^{-30} (\frac{300}{T})^{16}$
R35	$H_3O^+(H_2O) + M \rightarrow H_3O^+ + H_2O + M$	$4.3 \times 10^{-2} (\frac{300}{T})^4 \exp(\frac{-16430}{T})$
R36	$H_3O^+(H_2O)_2 + M \rightarrow H_3O^+(H_2O) + H_2O + M$	$2.1 \times 10^{-2} (\frac{300}{T})^{7.5} \exp(\frac{-10030}{T})$
R37	$H_3O^+(H_2O)_3 + M \rightarrow H_3O^+(H_2O)_2 + H_2O + M$	$1.7 \times 10^{-2} (\frac{300}{T})^{8.1} \exp(\frac{-8320}{T})$
R38	$H_3O^+(H_2O)_4 + M \rightarrow H_3O^+(H_2O)_3 + H_2O + M$	$1.3 \times 10^{-4} (\frac{300}{T})^{14} \exp(\frac{-5750}{T})$
R39	$H_3O^+(H_2O)_5 + M \rightarrow H_3O^+(H_2O)_4 + H_2O + M$	$3.3 \times 10^{-5} (\frac{300}{T})^{15.3} \exp(\frac{-5000}{T})$
R40	$H_3O^+(H_2O)_6 + M \rightarrow H_3O^+(H_2O)_5 + H_2O + M$	$4.6 \times 10^{-6} (\frac{300}{T})^{16} \exp(\frac{-5000}{T})$

Table 3.5: (Continued.)

No.	Reaction	Reaction rate coefficient ($\text{cm}^3 \text{s}^{-1}$ or $\text{cm}^6 \text{s}^{-1}$)
(4) Electron-ion recombination		
R41	$e + \text{N}_2^+ \rightarrow \text{N} + \text{N}$	$2.8 \times 10^{-7} \left(\frac{300}{T_e}\right)^{0.5}$
R42	$e + \text{N}_4^+ \rightarrow \text{N}_2 + \text{N}_2$	$2.6 \times 10^{-6} \left(\frac{300}{T_e}\right)^{0.41}$
R43	$e + \text{O}_2^+ \rightarrow \text{O} + \text{O}$	$2.0 \times 10^{-7} \left(\frac{300}{T_e}\right)$
R44	$e + \text{O}_4^+ \rightarrow \text{O}_2 + \text{O}_2$	$4.2 \times 10^{-6} \left(\frac{300}{T_e}\right)^{0.48}$
R45	$e + \text{N}_2\text{H}^+ \rightarrow \text{H} + \text{N}_2$	2.4×10^{-7}
R46	$e + \text{N}_2\text{O}_2^+ \rightarrow \text{N}_2 + \text{O}_2$	$1.3 \times 10^{-6} \left(\frac{300}{T_e}\right)^{0.5}$
R47	$e + \text{H}_2\text{O}^+ \rightarrow \text{neutrals}$	$4.3 \times 10^{-7} \left(\frac{300}{T_e}\right)^{0.7}$
R48	$e + \text{H}_3\text{O}^+ \rightarrow \text{neutrals}$	$8.0 \times 10^{-7} \left(\frac{300}{T_e}\right)^{0.8}$
R49	$e + \text{H}_3\text{O}^+(\text{OH}) \rightarrow \text{neutrals}$	$2.0 \times 10^{-6} \left(\frac{300}{T_e}\right)^{0.5}$
R50	$e + \text{H}_3\text{O}^+(\text{H}_2\text{O}) \rightarrow \text{H} + 2\text{H}_2\text{O}$	$2.5 \times 10^{-6} \left(\frac{300}{T_e}\right)^{0.5}$
R51	$e + \text{H}_3\text{O}^+(\text{H}_2\text{O})_2 \rightarrow \text{H} + 3\text{H}_2\text{O}$	$4.5 \times 10^{-6} \left(\frac{300}{T_e}\right)^{0.5}$
R52	$e + \text{H}_3\text{O}^+(\text{H}_2\text{O})_3 \rightarrow \text{H} + 4\text{H}_2\text{O}$	$6.5 \times 10^{-6} \left(\frac{300}{T_e}\right)^{0.5}$
R53	$e + \text{H}_3\text{O}^+(\text{H}_2\text{O})_4 \rightarrow \text{H} + 5\text{H}_2\text{O}$	$8.5 \times 10^{-6} \left(\frac{300}{T_e}\right)^{0.5}$
R54	$e + \text{H}_3\text{O}^+(\text{H}_2\text{O})_5 \rightarrow \text{H} + 6\text{H}_2\text{O}$	$10.5 \times 10^{-6} \left(\frac{300}{T_e}\right)^{0.5}$
R55	$e + \text{H}_3\text{O}^+(\text{H}_2\text{O})_6 \rightarrow \text{H} + 7\text{H}_2\text{O}$	$12.5 \times 10^{-6} \left(\frac{300}{T_e}\right)^{0.5}$
R56	$e + \text{H}_3\text{O}^+(\text{H}_2\text{O}) + \text{H}_2\text{O} \rightarrow \text{H} + 3\text{H}_2\text{O}$	$2.7 \times 10^{-23} \left(\frac{300}{T_e}\right)^2$
R57	$e + \text{H}_3\text{O}^+(\text{H}_2\text{O})_2 + \text{H}_2\text{O} \rightarrow \text{H} + 4\text{H}_2\text{O}$	$2.7 \times 10^{-23} \left(\frac{300}{T_e}\right)^2$
R58	$e + \text{H}_3\text{O}^+(\text{H}_2\text{O})_3 + \text{H}_2\text{O} \rightarrow \text{H} + 5\text{H}_2\text{O}$	$2.7 \times 10^{-23} \left(\frac{300}{T_e}\right)^2$
R59	$e + \text{H}_3\text{O}^+(\text{H}_2\text{O})_4 + \text{H}_2\text{O} \rightarrow \text{H} + 6\text{H}_2\text{O}$	$2.7 \times 10^{-23} \left(\frac{300}{T_e}\right)^2$
R60	$e + \text{H}_3\text{O}^+(\text{H}_2\text{O})_5 + \text{H}_2\text{O} \rightarrow \text{H} + 7\text{H}_2\text{O}$	$2.7 \times 10^{-23} \left(\frac{300}{T_e}\right)^2$
R61	$e + \text{H}_3\text{O}^+(\text{H}_2\text{O})_6 + \text{H}_2\text{O} \rightarrow \text{H} + 8\text{H}_2\text{O}$	$2.7 \times 10^{-23} \left(\frac{300}{T_e}\right)^2$
R62	$e + \text{O}_2^+(\text{H}_2\text{O}) \rightarrow \text{O}_2 + \text{H}_2\text{O}$	$3.0 \times 10^{-7} \left(\frac{300}{T_e}\right)^{0.5}$
R63	$2e + \text{N}_2^+ \rightarrow e + \text{N}_2$	$1.0 \times 10^{-19} \left(\frac{300}{T_e}\right)^{4.5}$
R64	$2e + \text{O}_2^+ \rightarrow e + \text{O}_2$	$1.0 \times 10^{-19} \left(\frac{300}{T_e}\right)^{4.5}$
R65	$2e + \text{H}_2\text{O}^+ \rightarrow e + \text{H}_2\text{O}$	$1.0 \times 10^{-19} \left(\frac{300}{T_e}\right)^{4.5}$
(5) Ion-ion recombination		
R66	$\text{O}_2^- + \text{N}_2^+ + \text{M} \rightarrow \text{O}_2 + \text{N}_2 + \text{M}$	$2.0 \times 10^{-25} \left(\frac{300}{T}\right)^{2.5}$
R67	$\text{O}_2^- + \text{O}_2^+ + \text{M} \rightarrow \text{O}_2 + \text{O}_2 + \text{M}$	$2.0 \times 10^{-25} \left(\frac{300}{T}\right)^{2.5}$
R68	$\text{O}_2^- + \text{H}_2\text{O}^+ + \text{M} \rightarrow \text{O}_2 + \text{H}_2\text{O} + \text{M}$	$2.0 \times 10^{-25} \left(\frac{300}{T}\right)^{2.5}$
(6) Light emission		
R69	$e + \text{N}_2 \rightarrow e + \text{N}_2(\text{C})$	$f_{11}(E/N)$
R70	$\text{N}_2(\text{C}) + \text{N}_2 \rightarrow \text{N}_2 + \text{N}_2$	1.3×10^{-11}
R71	$\text{N}_2(\text{C}) + \text{O}_2 \rightarrow \text{N}_2 + \text{O}_2$	3.0×10^{-10}
R72	$\text{N}_2(\text{C}) \rightarrow \text{N}_2(\text{B}) + h\nu$	$1/(42 \text{ ns})$

1. In [137], a total ionization reaction like R3 was used for H_2O . Here more ionization reaction channels (R3–R8) are included when using Kawaguchi H_2O cross sections.

2. In [137], a rate coefficient function was used for three-body attachment reactions R9 and R10. Here their rate coefficients are obtained using BOLSIG–.

3. In [137], rate coefficients for R29–R40 were pressure- and temperature-dependent.

Here pressure-dependence is not taken into account as the pressure in our simulations is (approximately) 1 bar.

4. In [137], the third body for R66–R88 contained any neutral species.

Here we only include the gas molecule M.

5. R69–R72 are included for light emission, which were taken from [177].

Table 3.6: The chemistry set for humid air from Komuro *et al* [170, 171]. The reactions involving charged particles were taken from table 1 of [171] with some additions (highlighted in red) from table 2 of [170]. Other reactions were taken from tables 1 and 3 of [170]. $T(\text{K})$ and $T_e(\text{K})$ are gas and electron temperatures, respectively.

No.	Reaction	Reaction rate coefficient
(1) Vibrational excitation		
R1	$e + \text{N}_2 \rightarrow e + \text{N}_2(v)$	$f_1(E/N)$
R2	$e + \text{O}_2 \rightarrow e + \text{O}_2(v)$	$f_2(E/N)$
R3	$e + \text{H}_2\text{O} \rightarrow e + \text{H}_2\text{O}(v)$	$f_3(E/N)$
(2) Electron excitation		
R4	$e + \text{N}_2 \rightarrow e + \text{N}_2(\text{A}_1)$	$f_4(E/N)$
R5	$e + \text{N}_2 \rightarrow e + \text{N}_2(\text{A}_2)$	$f_5(E/N)$
R6	$e + \text{N}_2 \rightarrow e + \text{N}_2(\text{B})$	$f_6(E/N)$
R7	$e + \text{N}_2 \rightarrow e + \text{N}_2(\text{a})$	$f_7(E/N)$
R8	$e + \text{N}_2 \rightarrow e + \text{N}_2(\text{C})$	$f_8(E/N)$
R9	$e + \text{N}_2 \rightarrow e + \text{N}_2(\text{E})$	$f_9(E/N)$
R10	$e + \text{O}_2 \rightarrow e + \text{O}_2(\text{a})$	$f_{10}(E/N)$
R11	$e + \text{O}_2 \rightarrow e + \text{O}_2(\text{b})$	$f_{11}(E/N)$
R12	$e + \text{O}_2 \rightarrow e + \text{O}_2(\text{A})$	$f_{12}(E/N)$
(3) Electron dissociation		
R13	$e + \text{N}_2 \rightarrow e + \text{N}(^4\text{S}) + \text{N}(^2\text{D})$	$f_{13}(E/N)$
R14	$e + \text{O}_2 \rightarrow e + \text{O}(^3\text{P}) + \text{O}(^3\text{P})$	$f_{14}(E/N)$
R15	$e + \text{O}_2 \rightarrow e + \text{O}(^3\text{P}) + \text{O}(^1\text{D})$	$f_{15}(E/N)$
R16	$e + \text{O}_2 \rightarrow e + \text{O}(^3\text{P}) + \text{O}(^1\text{S})$	$f_{16}(E/N)$
(4) Electron impact ionization		
R17	$e + \text{N}_2 \rightarrow 2e + \text{N}_2^+$	$f_{17}(E/N)$
R18	$e + \text{O}_2 \rightarrow 2e + \text{O}_2^+$	$f_{18}(E/N)$
R19	$e + \text{H}_2\text{O} \rightarrow 2e + \text{H}_2\text{O}^+$	$f_{19}(E/N)$
R20	$e + \text{H}_2\text{O} \rightarrow 2e + \text{H}^+ + \text{OH}$	$f_{20}(E/N)$
R21	$e + \text{H}_2\text{O} \rightarrow 2e + \text{OH}^+ + \text{H}$	$f_{21}(E/N)$
R22	$e + \text{H}_2\text{O} \rightarrow 2e + \text{O}^+ + \text{H}_2$	$f_{22}(E/N)$
R23	$e + \text{H}_2\text{O} \rightarrow 2e + \text{H}_2^+ + \text{O}$	$f_{23}(E/N)$
R24	$e + \text{H}_2\text{O} \rightarrow 3e + \text{O}^{2+} + \text{H}_2$	$f_{24}(E/N)$
(5) Electron attachment		
R25	$e + \text{O}_2 + \text{O}_2 \rightarrow \text{O}_2^- + \text{O}_2$	$f_{25}(E/N)$
R26	$e + \text{O}_2 \rightarrow \text{O}^- + \text{O}(^3\text{P})$	$f_{26}(E/N)$
R27	$e + \text{H}_2\text{O} \rightarrow \text{H}^- + \text{OH}$	$f_{27}(E/N)$
R28	$e + \text{H}_2\text{O} \rightarrow \text{OH}^- + \text{H}$	$f_{28}(E/N)$
R29	$e + \text{H}_2\text{O} \rightarrow \text{O}^- + \text{H}_2$	$f_{29}(E/N)$
R30	$e + \text{O}_2 + \text{H}_2\text{O} \rightarrow \text{O}_2^- + \text{H}_2\text{O}$	$f_{30}(E/N) = 7 \times f_{25}(E/N)$
(6) Electron detachment		
R31	$\text{O}_2^- + \text{N}_2 \rightarrow e + \text{N}_2 + \text{O}_2$	$1.90 \times 10^{-12} \left(\frac{T}{300}\right)^{0.5} \exp\left(\frac{-4990}{T}\right)$
R32	$\text{O}_2^- + \text{O}_2 \rightarrow e + \text{O}_2 + \text{O}_2$	$2.70 \times 10^{-10} \left(\frac{T}{300}\right)^{0.5} \exp\left(\frac{-5590}{T}\right)$
R33	$\text{O}_2^- + \text{O}_2(\text{a}) \rightarrow e + 2\text{O}_2$	2.00×10^{-10}
R34	$\text{O}_2^- + \text{O}(^3\text{P}) \rightarrow e + \text{O}_3$	3.00×10^{-10}
R35	$\text{O}_2^- + \text{H} \rightarrow e + \text{HO}_2$	1.20×10^{-9}
R36	$\text{O}^- + \text{O}_2(\text{a}) \rightarrow e + \text{O}_3$	3.00×10^{-10}

Table 3.6: (Continued.)

No.	Reaction	Reaction rate coefficient
R37	$O^- + O(^3P) \rightarrow e + O_2$	2.00×10^{-10}
R38	$H^- + O_2 \rightarrow e + HO_2$	1.20×10^{-9}
R39	$H^- + H \rightarrow e + H_2$	2.00×10^{-9}
R40	$OH^- + O(^3P) \rightarrow e + HO_2$	2.00×10^{-10}
R41	$OH^- + H \rightarrow e + H_2O$	1.40×10^{-9}
(7) Negative ion conversion		
R42	$O_2^- + H \rightarrow OH^- + O(^3P)$	1.50×10^{-9}
R43	$H^- + H_2O \rightarrow OH^- + H_2$	1.00×10^{-9}
(8) Positive ion conversion		
R44	$N_2^+ + N_2 + M \rightarrow N_4^+ + M$	$5.20 \times 10^{-29} (\frac{300}{T})^{2.2}$
R45	$O_2^+ + N_2 + N_2 \rightarrow N_2O_2^+ + N_2$	$9.00 \times 10^{-31} (\frac{300}{T})^2$
R46	$O_2^+ + O_2 + M \rightarrow O_4^+ + M$	$2.40 \times 10^{-30} (\frac{300}{T})^{3.2}$
R47	$O_2^+ + H_2O + M \rightarrow O_2^+(H_2O) + M$	$2.60 \times 10^{-28} (\frac{300}{T})^4$
R48	$N_4^+ + N_2 \rightarrow N_2^+ + 2N_2$	$10^{-14.6+0.0036(T-300)}$
R49	$N_4^+ + O_2 \rightarrow O_2^+ + 2N_2$	2.50×10^{-10}
R50	$O_4^+ + N_2 \rightarrow N_2O_2^+ + O_2$	$4.60 \times 10^{-12} (\frac{T}{300})^{2.5} \exp(\frac{-2650}{T})$
R51	$O_4^+ + O_2 \rightarrow O_2^+ + 2O_2$	$3.30 \times 10^{-6} (\frac{300}{T})^4 \exp(\frac{-5030}{T})$
R52	$O_4^+ + O_2(a) \rightarrow O_2^+ + 2O_2$	1.00×10^{-10}
R53	$O_4^+ + O_2(b) \rightarrow O_2^+ + 2O_2$	1.00×10^{-10}
R54	$O_4^+ + O(^3P) \rightarrow O_2^+ + O_3$	3.00×10^{-10}
R55	$O_4^+ + O(^1D) \rightarrow O_2^+ + O_3$	3.00×10^{-10}
R56	$O_4^+ + O(^1S) \rightarrow O_2^+ + O_3$	3.00×10^{-10}
R57	$O_4^+ + H_2O \rightarrow O_2^+(H_2O) + O_2$	1.70×10^{-9}
R58	$O_2^+(H_2O) + H_2O \rightarrow H_3O^+ + OH + O_2$	1.30×10^{-9}
R59	$N_2O_2^+ + N_2 \rightarrow O_2^+ + 2N_2$	$1.10 \times 10^{-6} (\frac{300}{T})^{5.3} \exp(\frac{-2357}{T})$
R60	$N_2O_2^+ + O_2 \rightarrow O_4^+ + N_2$	1.00×10^{-9}
R61	$H_3O^+ + H_2O + M \rightarrow H_3O^+(H_2O) + M$	$3.40 \times 10^{-27} (\frac{300}{T})^4$
R62	$H_3O^+(H_2O) + H_2O + M \rightarrow H_3O^+(H_2O)_2 + M$	$2.30 \times 10^{-27} (\frac{300}{T})^4$
R63	$H_3O^+(H_2O)_2 + H_2O + M \rightarrow H_3O^+(H_2O)_3 + M$	$2.40 \times 10^{-27} (\frac{300}{T})^4$
(9) Electron-ion recombination		
R64	$e + N_2^+ \rightarrow N(^4S) + N(^4S)$	$1.80 \times 10^{-7} (\frac{300}{T_e})^{0.39}$
R65	$e + N_2^+ \rightarrow N_2$	4.00×10^{-12}
R66	$e + N_4^+ \rightarrow N_2 + N_2$	$2.00 \times 10^{-6} (\frac{300}{T_e})^{0.5}$
R67	$e + O_2^+ \rightarrow O(^3P) + O(^3P)$	$2.00 \times 10^{-7} (\frac{300}{T_e})^{0.7}$
R68	$e + O_2^+ \rightarrow O_2$	4.00×10^{-12}
R69	$e + O_4^+ \rightarrow O_2 + O_2$	$1.40 \times 10^{-6} (\frac{300}{T_e})^{0.5}$
R70	$e + N_2O_2^+ \rightarrow N_2 + O_2$	$1.30 \times 10^{-6} (\frac{300}{T_e})^{0.5}$
R71	$e + H_2O^+ \rightarrow OH + H$	3.80×10^{-7}
R72	$e + H_2O^+ \rightarrow H_2 + O(^3P)$	1.40×10^{-7}
R73	$e + H_2O^+ \rightarrow 2H + O(^3P)$	1.70×10^{-7}
R74	$e + H_3O^+(H_2O)_3 \rightarrow H + 4H_2O$	$5.50 \times 10^{-7} (\frac{300}{T_e})^{0.78}$
(10) Ion-ion recombination		
R75	$N_2^+ + O^- \rightarrow N_2 + O(^3P)$	4.00×10^{-7}
R76	$N_2^+ + O_2^- \rightarrow N_2 + O_2$	1.60×10^{-7}

Table 3.6: (Continued.)

No.	Reaction	Reaction rate coefficient (cm ³ s ⁻¹ or cm ⁶ s ⁻¹)
R77	$O_2^+ + O^- \rightarrow O_2 + O(^3P)$	9.60×10^{-8}
R78	$O_2^+ + O_2^- \rightarrow O_2 + O_2$	4.20×10^{-7}
R79	$O_2^+ + O_2^- + O_2 \rightarrow 2O(^3P) + 2O_2$	$2.00 \times 10^{-25} \left(\frac{300}{T}\right)^{2.5}$
R80	$O_4^+ + O_2^- + O_2 \rightarrow 2O(^3P) + 3O_2$	$2.00 \times 10^{-25} \left(\frac{300}{T}\right)^{2.5}$
R81	$H_2O^+ + O^- \rightarrow H_2O + O(^3P)$	4.00×10^{-7}
R82	$H_2O^+ + O_2^- \rightarrow H_2O + O_2$	4.00×10^{-7}
(11) Neutral species conversion		
R83	$N_2(A_1) + O_2 \rightarrow N_2 + O_2(b)$	7.50×10^{-13}
R84	$N_2(A_1) + O_2 \rightarrow N_2 + 2O(^3P)$	1.70×10^{-12}
R85	$N_2(A_1) + O_2 \rightarrow N_2O + O(^3P)$	7.80×10^{-12}
R86	$N_2(A_1) + N_2(A_1) \rightarrow N_2 + N_2(B)$	7.70×10^{-11}
R87	$N_2(A_1) + N_2(A_1) \rightarrow N_2 + N_2(C)$	1.60×10^{-10}
R88	$N_2(A_1) + N_2(A_1) \rightarrow N_2 + N_2(E)$	1.00×10^{-11}
R89	$N_2(A_1) + O(^3P) \rightarrow N_2 + O(^3P)$	2.00×10^{-11}
R90	$N_2(A_1) + O(^3P) \rightarrow N_2 + O(^1S)$	3.00×10^{-11}
R91	$N_2(A_1) + O(^3P) \rightarrow NO + N(^2D)$	7.00×10^{-12}
R92	$N_2(A_1) + H \rightarrow N_2 + H$	2.10×10^{-10}
R93	$N_2(A_1) + OH \rightarrow N_2 + OH$	1.00×10^{-10}
R94	$N_2(A_1) + H_2O \rightarrow N_2 + H + OH$	5.00×10^{-14}
R95	$N_2(A_1) + NO \rightarrow N_2 + NO(A)$	6.90×10^{-11}
R96	$N_2(A_2) + N_2 \rightarrow N_2 + N_2(A_1)$	1.00×10^{-11}
R97	$N_2(A_2) + O(^3P) \rightarrow N_2 + O(^3P)$	2.00×10^{-11}
R98	$N_2(A_2) + O(^3P) \rightarrow NO + N(^4S)$	7.00×10^{-12}
R99	$N_2(A_2) + H \rightarrow N_2 + H$	2.10×10^{-10}
R100	$N_2(A_2) + OH \rightarrow N_2 + OH$	1.00×10^{-10}
R101	$N_2(A_2) + H_2O \rightarrow N_2 + H + OH$	5.00×10^{-14}
R102	$N_2(A_2) + NO \rightarrow N_2 + NO(A)$	6.90×10^{-11}
R103	$N_2(B) + O_2 \rightarrow N_2 + 2O(^3P)$	3.00×10^{-10}
R104	$N_2(B) + N_2 \rightarrow N_2 + N_2(A_1)$	1.00×10^{-11}
R105	$N_2(B) \rightarrow N_2(A_1) + h\nu$	$1.50 \times 10^5 \text{ (s}^{-1}\text{)}$
R106	$N_2(a) + O_2 \rightarrow N_2 + O(^3P) + O(^1D)$	2.80×10^{-11}
R107	$N_2(a) + N_2 \rightarrow N_2 + N_2$	2.00×10^{-13}
R108	$N_2(a) + N_2 \rightarrow N_2 + N_2(B)$	2.00×10^{-13}
R109	$N_2(a) + H_2O \rightarrow N_2 + H + OH$	3.00×10^{-10}
R110	$N_2(a) + H_2 \rightarrow N_2 + 2H$	2.60×10^{-10}
R111	$N_2(a) + NO \rightarrow N_2 + N(^4S) + O(^3P)$	3.60×10^{-10}
R112	$N_2(C) + O_2 \rightarrow N_2 + 2O(^3P)$	2.50×10^{-10}
R113	$N_2(C) + N_2 \rightarrow N_2 + N_2(B)$	1.00×10^{-11}
R114	$N_2(C) + N_2 \rightarrow N_2 + N_2(a)$	1.00×10^{-11}
R115	$N_2(C) \rightarrow N_2(B) + h\nu$	$2.80 \times 10^7 \text{ (s}^{-1}\text{)}$
R116	$N_2(E) + N_2 \rightarrow N_2 + N_2(C)$	1.00×10^{-10}
R117	$NO(A) \rightarrow NO + h\nu$	$5.10 \times 10^6 \text{ (s}^{-1}\text{)}$
R118	$N(^4S) + O_2 \rightarrow NO + O(^3P)$	$4.47 \times 10^{-12} \left(\frac{T}{300}\right) \exp\left(\frac{-3270.2}{T}\right)$
R119	$N(^4S) + O(^3P) + N_2 \rightarrow N_2 + NO$	$6.89 \times 10^{-33} \exp\left(\frac{134.7}{T}\right)$
R120	$N(^4S) + N(^4S) + N_2 \rightarrow N_2 + N_2$	$8.27 \times 10^{-34} \exp\left(\frac{500}{T}\right)$
R121	$N(^4S) + OH \rightarrow NO + H$	$3.80 \times 10^{-11} \exp\left(\frac{85.39}{T}\right)$

Table 3.6: (Continued.)

No.	Reaction	Reaction rate coefficient (cm ³ s ⁻¹ or cm ⁶ s ⁻¹)
R122	N(⁴ S) + HO ₂ → NO + OH	2.19 × 10 ⁻¹¹
R123	N(⁴ S) + NO → N ₂ + O(³ P)	3.51 × 10 ⁻¹¹ exp($\frac{-49.84}{T}$)
R124	N(⁴ S) + NO ₂ → NO + NO	2.30 × 10 ⁻¹²
R125	N(⁴ S) + NO ₂ → N ₂ O + O(³ P)	5.80 × 10 ⁻¹² exp($\frac{-220}{T}$)
R126	N(² D) + O ₂ → NO + O(³ P)	1.50 × 10 ⁻¹² ($\frac{T}{300}$) ^{0.5}
R127	N(² D) + O ₂ → NO + O(¹ D)	9.70 × 10 ⁻¹² exp($\frac{185}{T}$)
R128	N(² D) + N ₂ → N ₂ + N(⁴ S)	1.70 × 10 ⁻¹⁴
R129	N(² D) + O(³ P) → N(⁴ S) + O(³ P)	3.30 × 10 ⁻¹² exp($\frac{260}{T}$)
R130	N(² D) + H ₂ O → NH + OH	4.00 × 10 ⁻¹¹
R131	N(² D) + NO → N ₂ + O(³ P)	1.80 × 10 ⁻¹⁰
R132	O ₂ (a) + O ₂ → O ₂ + O ₂	2.20 × 10 ⁻¹⁸ ($\frac{T}{300}$) ^{0.8}
R133	O ₂ (a) + N ₂ → N ₂ + O ₂	1.40 × 10 ⁻¹⁹
R134	O ₂ (a) + O(³ P) → O ₂ + O(³ P)	7.00 × 10 ⁻¹⁶
R135	O ₂ (a) + N(⁴ S) → NO + O(³ P)	2.00 × 10 ⁻¹⁴
R136	O ₂ (a) + NO → O ₂ + NO	2.50 × 10 ⁻¹¹
R137	O ₂ (a) + NO → NO ₂ + O(³ P)	3.49 × 10 ⁻¹⁷
R138	O ₂ (b) + O ₂ → O ₂ + O ₂ (a)	4.10 × 10 ⁻¹⁷
R139	O ₂ (b) + N ₂ → N ₂ + O ₂ (a)	2.10 × 10 ⁻¹⁵
R140	O ₂ (b) + O(³ P) → O ₂ + O(³ P)	8.00 × 10 ⁻¹⁴
R141	O ₂ (b) + H ₂ O → O ₂ + H ₂ O	4.60 × 10 ⁻¹²
R142	O ₂ (b) + NO → O ₂ (a) + NO	4.00 × 10 ⁻¹⁴
R143	O ₂ (b) + O ₃ → 2O ₂ (a) + O(³ P)	1.80 × 10 ⁻¹¹
R144	O ₂ (A) + O ₂ → O ₂ (b) + O ₂ (b)	2.90 × 10 ⁻¹³
R145	O ₂ (A) + N ₂ → N ₂ + O ₂ (b)	3.00 × 10 ⁻¹³
R146	O ₂ (A) + O(³ P) → O ₂ (b) + O(¹ D)	9.00 × 10 ⁻¹²
R147	O(³ P) + O ₂ + O ₂ → O ₂ + O ₃	6.01 × 10 ⁻³⁴ ($\frac{300}{T}$) ^{2.6}
R148	O(³ P) + O ₂ + N ₂ → N ₂ + O ₃	5.51 × 10 ⁻³⁴ ($\frac{300}{T}$) ^{2.6}
R149	O(³ P) + O(³ P) + O ₂ → O ₂ + O ₂	3.81 × 10 ⁻³³ ($\frac{300}{T}$) ^{0.63}
R150	O(³ P) + O(³ P) + N ₂ → N ₂ + O ₂	9.46 × 10 ⁻³⁴ exp($\frac{484.7}{T}$)
R151	O(³ P) + OH → O ₂ + H	2.40 × 10 ⁻¹¹ exp($\frac{110}{T}$)
R152	O(³ P) + HO ₂ → O ₂ + OH	2.70 × 10 ⁻¹¹ exp($\frac{224}{T}$)
R153	O(³ P) + NO + N ₂ → N ₂ + NO ₂	1.03 × 10 ⁻³⁰ ($\frac{300}{T}$) ^{2.87} exp($\frac{780.5}{T}$)
R154	O(³ P) + NO ₂ → O ₂ + NO	5.50 × 10 ⁻¹² exp($\frac{-187.9}{T}$)
R155	O(³ P) + O ₃ → O ₂ + O ₂	8.00 × 10 ⁻¹² exp($\frac{-2060}{T}$)
R156	O(¹ D) + O ₂ → O ₂ + O(³ P)	3.12 × 10 ⁻¹¹ exp($\frac{70}{T}$)
R157	O(¹ D) + N ₂ → N ₂ + O(³ P)	2.10 × 10 ⁻¹¹ exp($\frac{115}{T}$)
R158	O(¹ D) + H ₂ O → O ₂ + H ₂	3.57 × 10 ⁻¹⁰
R159	O(¹ D) + H ₂ O → OH + OH	2.20 × 10 ⁻¹⁰
R160	O(¹ D) + H ₂ → H + OH	1.10 × 10 ⁻¹⁰
R161	O(¹ D) + H ₂ O ₂ → O ₂ + H ₂ O	5.20 × 10 ⁻¹⁰
R162	O(¹ D) + O ₃ → O ₂ + 2O(³ P)	1.20 × 10 ⁻¹⁰
R163	O(¹ S) + H ₂ O → O ₂ + H ₂	5.00 × 10 ⁻¹⁰
R164	O(¹ S) + H ₂ O → H ₂ O + O(³ P)	3.00 × 10 ⁻¹⁰
R165	O(¹ S) + H ₂ O → OH + OH	5.00 × 10 ⁻¹⁰
R166	O ₃ + H → O ₂ + OH	1.40 × 10 ⁻¹⁰ exp($\frac{-480}{T}$)
R167	O ₃ + OH → O ₂ + HO ₂	1.70 × 10 ⁻¹² exp($\frac{-940}{T}$)

Table 3.6: (Continued.)

No.	Reaction	Reaction rate coefficient (cm ³ s ⁻¹ or cm ⁶ s ⁻¹)
R168	O ₃ + NO → O ₂ + NO ₂	3.16 × 10 ⁻¹² exp($\frac{1563}{T}$)
R169	O ₃ + O ₃ → O ₂ + O ₃ + O(³ P)	7.16 × 10 ⁻¹⁰ exp($\frac{-11200}{T}$)
R170	H + O ₂ + O ₂ → O ₂ + HO ₂	5.94 × 10 ⁻³² ($\frac{300}{T}$)
R171	H + O ₂ + N ₂ → N ₂ + HO ₂	5.94 × 10 ⁻³² ($\frac{300}{T}$)
R172	H + OH + N ₂ → N ₂ + H ₂ O	6.87 × 10 ⁻³¹ ($\frac{300}{T}$) ²
R173	H + OH + H ₂ O → H ₂ O + H ₂ O	4.38 × 10 ⁻³¹ ($\frac{300}{T}$) ²
R174	H + HO ₂ → O ₂ + H ₂	1.75 × 10 ⁻¹⁰ exp($\frac{-1030}{T}$)
R175	H + HO ₂ → H ₂ O + O(³ P)	5.00 × 10 ⁻¹¹ exp($\frac{-866}{T}$)
R176	H + HO ₂ → OH + OH	7.40 × 10 ⁻¹⁰ exp($\frac{-700}{T}$)
R177	OH + OH → H ₂ O + O(³ P)	6.20 × 10 ⁻¹⁴ ($\frac{T}{300}$) ^{2.6} exp($\frac{945}{T}$)
R178	OH + OH → H ₂ O ₂	2.60 × 10 ⁻¹¹
R179	OH + OH + O ₂ → O ₂ + H ₂ O ₂	6.05 × 10 ⁻³¹ ($\frac{300}{T}$) ³
R180	OH + OH + N ₂ → N ₂ + H ₂ O ₂	6.90 × 10 ⁻³¹ ($\frac{300}{T}$) ^{0.8}
R181	OH + OH + H ₂ O → H ₂ O + H ₂ O ₂	1.54 × 10 ⁻³¹ ($\frac{300}{T}$) ² exp($\frac{183.6}{T}$)
R182	OH + HO ₂ → O ₂ + H ₂ O	4.80 × 10 ⁻¹¹ exp($\frac{250}{T}$)
R183	OH + NO + O ₂ → O ₂ + HNO ₂	7.40 × 10 ⁻³¹ ($\frac{300}{T}$) ^{2.4}
R184	OH + NO + N ₂ → N ₂ + HNO ₂	7.40 × 10 ⁻³¹ ($\frac{300}{T}$) ^{2.4}
R185	OH + NO ₂ + O ₂ → O ₂ + HNO ₃	2.20 × 10 ⁻³⁰ ($\frac{300}{T}$) ^{2.9}
R186	OH + NO ₂ + N ₂ → N ₂ + HNO ₃	2.60 × 10 ⁻³⁰ ($\frac{300}{T}$) ^{2.9}
R187	HO ₂ + NO → OH + NO ₂	3.60 × 10 ⁻¹² exp($\frac{269.4}{T}$)
R188	HO ₂ + NO ₂ → O ₂ + HNO ₂	1.20 × 10 ⁻¹³
R189	HO ₂ + HO ₂ → O ₂ + H ₂ O ₂	2.20 × 10 ⁻¹⁹ exp($\frac{600.2}{T}$)
R190	HO ₂ + HO ₂ + O ₂ → 2O ₂ + H ₂ O ₂	1.90 × 10 ⁻³³ exp($\frac{980}{T}$)
R191	HO ₂ + HO ₂ + N ₂ → O ₂ + N ₂ + H ₂ O ₂	1.90 × 10 ⁻³³ exp($\frac{980}{T}$)

1. In [170], H₂O(*v*₁), H₂O(*v*₂) and H₂O(*v*₃) were included. However, in Kawaguchi H₂O cross sections the vibrational excited state was only separated into H₂O(*v*₁) and H₂O(*v*₂), and here we merge them into H₂O(*v*).

2. Here we do not include electron dissociation reactions for H₂O (i.e., R24–R25 in table 1 of [170]), as Kawaguchi H₂O cross sections did not specify them.

3. In [171], a total ionization reaction like R19 was used for H₂O. Here more ionization reaction channels (R19–R24) are included when using Kawaguchi H₂O cross sections.

4. N(S) is replaced by N(⁴S), O(P) and O₂(P) by O(³P), O(D) and O(³D) by O(¹D), and O⁻(²P) by O⁻.

5. Here we do not include R88 (N₂⁺(B) → N₂⁺ + *hν*) in table 3 of [170].

6. Rate coefficients for R81–R82 have been corrected from 4.0 × 10⁻⁶ to 4.0 × 10⁻⁷ by checking their cited paper [178].

7. In [170], the rate coefficient for R120 was wrong, and we have revised it to 8.27 × 10⁻³⁴ exp($\frac{500}{T}$) according to [90].

Table 3.7: Excited states of N_2 , O_2 and H_2O with activation energies and corresponding effective states used in table 3.6. The table is partially based on table 4 of [170].

Excited state	Activation energy ϵ_e (eV)	Effective state
$N_2(X, v = 1)$	0.29	$N_2(v)$
$N_2(X, v = 2)$	0.59	$N_2(v)$
$N_2(X, v = 3)$	0.88	$N_2(v)$
$N_2(X, v = 4)$	1.17	$N_2(v)$
$N_2(X, v = 5)$	1.47	$N_2(v)$
$N_2(X, v = 6)$	1.76	$N_2(v)$
$N_2(X, v = 7)$	2.06	$N_2(v)$
$N_2(X, v = 8)$	2.35	$N_2(v)$
$N_2(A^3\Sigma_u^+, v = 0\dots4)$	6.17	$N_2(A_1)$
$N_2(A^3\Sigma_u^+, v = 5\dots9)$	7.00	$N_2(A_2)$
$N_2(B^3\Pi_g)$	7.35	$N_2(B)$
$N_2(W^3\Delta_u)$	7.36	$N_2(B)$
$N_2(A^3\Sigma_u^+, v > 10)$	7.80	$N_2(B)$
$N_2(B'^3\Sigma_u^-)$	8.16	$N_2(B)$
$N_2(a'^1\Sigma_u^-)$	8.40	$N_2(a)$
$N_2(a^1\Pi_g)$	8.55	$N_2(a)$
$N_2(w^1\Delta_u)$	8.89	$N_2(a)$
$N_2(C^3\Pi_u)$	11.03	$N_2(C)$
$N_2(E^3\Sigma_g^+)$	11.87	$N_2(E)$
$N_2(a''^1\Sigma_g^+)$	12.25	$N_2(E)$
$O_2(X, v = 1)$	0.19	$O_2(v)$
$O_2(X, v = 2)$	0.38	$O_2(v)$
$O_2(X, v = 3)$	0.57	$O_2(v)$
$O_2(X, v = 4)$	0.75	$O_2(v)$
$O_2(a^1\Delta_g)$	0.977	$O_2(a)$
$O_2(b^1\Sigma_g^+)$	1.627	$O_2(b)$
$O_2(c^1\Sigma_u^-)$	4.05	$O_2(A)$
$O_2(A'^3\Delta_u)$	4.26	$O_2(A)$
$O_2(A^3\Sigma_u^+)$	4.34	$O_2(A)$
$H_2O(X, v = 1)$	0.198	$H_2O(v)$
$H_2O(X, v = 2)$	0.466	$H_2O(v)$

Chapter 4

Effect of gas heating on repetitively pulsed streamer discharges

We study the effect of gas heating on simulations of repetitively pulsed positive streamer discharges in air. The simulations are performed with an axisymmetric fluid model in which the compressible Euler equations for gas dynamics are solved. We simulate up to 2 ms and up to 40 pulses and show how changes in the gas temperature and density affect the discharges. The pulse repetition rate and the applied voltage are varied, as well as the parameters that control the transfer of energy from the discharge to the gas. In our results, significant gas heating only occurs after multiple pulses, with more heat being deposited at higher voltages. A resulting reduction in the gas number density in the streamer channel causes streamers to grow longer, but their properties are also affected by the residual ionization from previous pulses.

The manuscript with the results in this chapter is under preparation:
H. Malla, U. Ebert and J. Teunissen. Effect of gas heating on repetitively pulsed streamer discharges.

4.1 Introduction

Streamers are highly-transient, space-charge dominated, filamentary discharges that can propagate in sub-breakdown electric fields in air due to a characteristic strong field enhancement at their tips [31]. In nature, they act as precursors to sprite discharges in the upper atmosphere [179, 180] and other discharges like sparks, and leaders [181–183]. Additionally, streamers are encountered in various industrial applications like high voltage circuit-breakers [12, 184], plasma medicine [20], plasma agriculture [21], and plasma combustion [14, 28, 126].

Despite being cold atmospheric plasmas, streamer discharges do affect the background gas: they lead to gas heating and they induce a gas flow. Streamer-like discharges are for example used to generate corona-wind for aerodynamic applications [24, 25, 185] or to de-ice aircraft wings [26, 27]. In some studies [181, 182, 186], 1-D radial self-consistent models were used to simulate the transition from a streamer to a leader or a spark. They show that Joule heating due to the streamer results in changes such as a decrease in the channel density and increased ionization due to an increase in reduced field inside the channel.

In laboratory and industrial settings, a repetitive voltage pulse source is often used to prevent the transition to a hotter discharge and to minimize energy consumption. The repetition frequency is then an important parameter, as it affects the energy deposition rate as well as the density of left-over ionized and excited species from a previous pulse. The impact of residual ionization on subsequent discharges in $N_2:O_2$ mixtures has been both experimentally studied in [71, 187] and numerically modeled in [64]. Experimentally [74], it was observed that an increase in channel temperature can result in either a glow discharge or a spark discharge depending on the electrode gap and pulse repetition rate. In [188], it was experimentally shown that for relatively low pulse repetition frequencies, the discharge channel temperature does not increase due to the discharge-induced gas flow. In [189], the effect of pulse repetition rate on the ignition of air-methane fuel mixtures was experimentally investigated in a DBD setup. They report a critical pulse repetition rate for which their fuel mixtures ignite below the auto-ignition temperature. Using zero-dimensional kinetic modeling in [190], it was demonstrated that the production of reactive oxygen species depends not only on pulse repetition frequency, but also on the gas temperature.

All the above studies highlight the importance of a changing gas temperature on streamer discharges in a repetitively pulsed setting. We therefore study the gas heating and flow caused by repetitively-pulsed streamer discharges with an axisymmetric fluid model, with which we self-consistently simulate up to 20 pulses. By varying the pulse repetition frequency (section 4.3.2), the applied voltage (4.3.3), and the heat deposition rate (section 4.3.4), we aim to understand how repetitive pulsed streamers heat the gas and how their properties evolve as a result. Our simulations are conducted on a millisecond timescale - allowing for comprehensive evolution of gas dynamics that was previously computationally

not feasible using a 2D-axisymmetric geometry.

4.2 Model

We study streamer discharges initiating at 1 bar and 300 K in a 80%:20% N₂:O₂ mixture in under-volted conditions in a 2D-axisymmetric geometry. We use the standard drift-diffusion fluid model to simulate the streamers (streamer model), coupled with the compressible Navier-Stokes equations to simulate neutral gas dynamics (neutral gas model). To this end we use the `afivo-streamer` code [44], whose streamer model has already been validated against experiments [87] and particle models [50]. The neutral gas model has also been numerically implemented using the Afivo-framework [45] which makes it easier to couple with the streamer model. We briefly summarize the streamer equations and the neutral gas dynamics equations below in sections 4.2.1 and 4.2.2 respectively.

4.2.1 Streamer model

The electron and ion densities, n_e and n_i evolve in time as

$$\partial_t n_e = \nabla \cdot (\mu_e \mathbf{E} n_e + D_e \nabla n_e) + S_e + S_{\text{ph}}, \quad (4.1)$$

$$\partial_t n_i + \nabla \cdot (q_i \mu_i \mathbf{E} n_i) = S_i. \quad (4.2)$$

Here $\mu_{e/i}$ is the electron/ion mobility coefficient, D_e the electron diffusion coefficient, q_i accounts for the species charge (0 for neutrals, -1 for negative ions and $+1$ for positive ions), and \mathbf{E} the electric field. The electron transport coefficients are assumed to depend on the local electric field (local field approximation) and were computed using BOLSIG- [53] using Phelps' cross-section data [88]. S_e and S_i are source (and sink) terms due to reactions involving electrons and ions respectively, for example ionization or recombination, see section 2.2.4. S_{ph} is a photo-ionization source term, which is here implemented according to Zheleznyak's model [35] as discussed in [47].

The electric field \mathbf{E} is calculated in the electrostatic approximation as $\mathbf{E} = -\nabla\phi$. Here ϕ is the electrostatic potential, which is obtained by solving the Poisson equation [45, 52]

$$\nabla^2 \phi = -e (\sum q_i n_i - n_e) / \epsilon_0, \quad (4.3)$$

where e is the electron charge and ϵ_0 is the vacuum permittivity. For computational details, refer to, e.g., [44, 47].

4.2.2 Neutral gas model

We solve the compressible Euler equations for gas dynamics, in which the gas density ρ , the gas velocity $\mathbf{u} = [u_r, u_z]$ and the energy density ϵ evolve in time

as:

$$\partial_t \rho + \nabla \cdot (\rho \mathbf{u}) = 0, \quad (4.4)$$

$$\partial_t (\rho u_r) + \nabla \cdot (\rho u_r \mathbf{u}) + \partial_r p = f_r + f_{\text{geom}}, \quad (4.5)$$

$$\partial_t (\rho u_z) + \nabla \cdot (\rho u_z \mathbf{u}) + \partial_z p = f_z, \quad (4.6)$$

$$\partial_t \epsilon + \nabla \cdot ((\epsilon + p) \mathbf{u}) = S_\epsilon, \quad (4.7)$$

where p is the pressure, S_ϵ the energy source term, $[f_r, f_z]$ the momentum source term, both of which are further elaborated in sections 4.2.2 and 4.2.2 respectively. Because we use an axisymmetric coordinate system, there is a so-called geometric source term in equation (4.5), given by $f_{\text{geom}} = p/r$. The energy density ϵ is related to the gas pressure and velocity by

$$\epsilon = p/(\gamma - 1) + \rho(u_r^2 + u_z^2)/2. \quad (4.8)$$

Finally, the neutral gas variables are related to each other by the ideal gas law, given by

$$pV = \rho R_{\text{spec}} T = N k_B T, \quad (4.9)$$

where $R_{\text{spec}} = 287.05 \text{ J kg}^{-1} \text{ K}^{-1}$ is the specific gas constant, and $k_B = 1.38 \times 10^{-23} \text{ J K}^{-1}$ is the Boltzmann constant. These equations are numerically implemented in the Afivo framework [45] using the Kurganov-Tadmor scheme [191], which makes it easy for them to be coupled to the streamer model.

Gas heating model

The discharge energy gained by the electrons is transferred to various degrees of freedom of the neutral gas (e.g., different excited states), as illustrated in figure 4.1. Over time, much of this energy is converted to thermal energy of the gas molecules. The rate at which this occurs depends on the degree of freedom in which the energy was stored. In literature, two major approaches have been used to model gas heating: a phenomenological approach and a kinetic approach. The kinetic approach is the most detailed, and it has been used in e.g. [193, 194]. With this approach, the transfer of energy from electrons to various types of excited states is modeled (based on cross-section data), as well as the evolution and the eventual de-excitation of these states, which then contribute a specific amount to the thermal heating of the gas. The phenomenological approach involves partitioning the Joule heating term into various energy distribution pathways (degrees of freedom) using ‘heating efficiencies’ and relaxation timescales for the vibrational and excitation degrees of freedom. In literature, this approach was used in [104, 195–197] where the heating efficiencies and relaxation timescales were assumed constant as compared to the works [183, 198] where these parameters were modeled in more detail. In this work, we use the phenomenological approach used in [195] where the individual instantaneous (fast) and slow energy relaxation processes are clumped together into two heating mechanisms. Constant

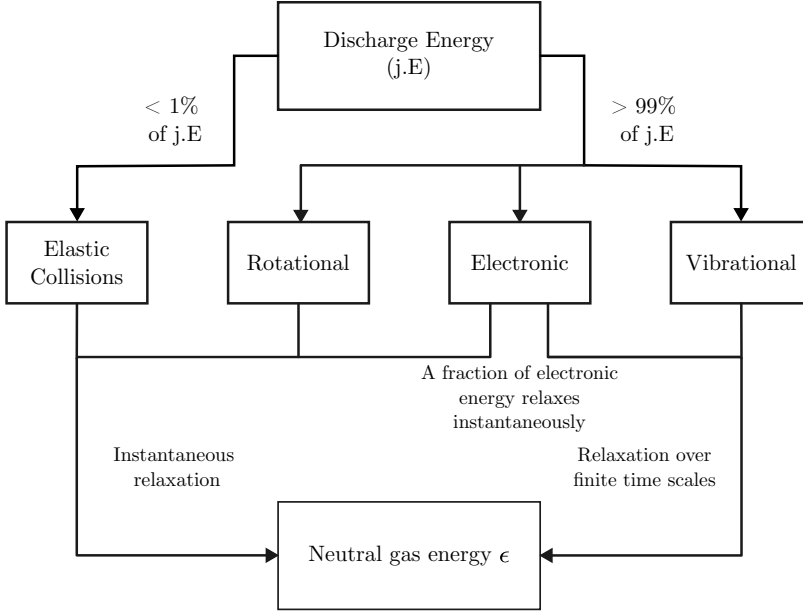


Figure 4.1: Flow chart showing energy transfer between atmospheric plasmas and neutral gas via various degrees of freedom, see e.g. [192].

heating efficiencies are used for these two mechanisms and a constant relaxation timescale for the slow energy relaxation process. The model is explained below.

We couple the streamer model to the neutral gas model via S_ϵ in equation 4.7 which is the heating source term, given by,

$$S_\epsilon = \eta_f \mathbf{j} \cdot \mathbf{E} + (q_s / \tau_s), \quad (4.10)$$

where

$$d_t q_s = \eta_s \mathbf{j} \cdot \mathbf{E} - (q_s / \tau_s). \quad (4.11)$$

In the above equations, $\mathbf{j} \cdot \mathbf{E}$ is the Joule heating term calculated using the streamer model, η_f , η_s are the fast and slow heating efficiencies respectively. Furthermore, q_s is the energy density that slowly relaxes into thermal gas energy over a given timescale τ_s . We assume τ_s to be constant, and study its effect in section 4.3.4.

Electro-hydrodynamic model

The terms f_r and f_z model the electro-hydrodynamic force (EHD) due to momentum transfer between charged particles and neutrals which are given by

$$\mathbf{f} = [f_r, f_z] = e (\Sigma q_i n_i - n_e) \mathbf{E}. \quad (4.12)$$

We remark that the effect of this term on our simulations is negligible.

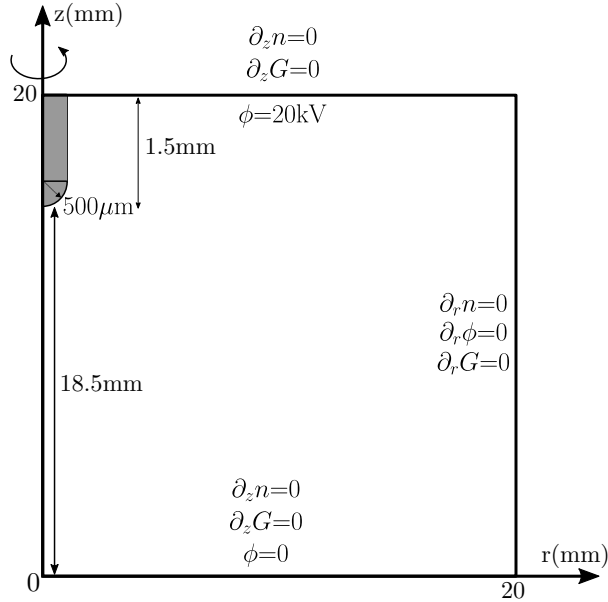


Figure 4.2: The axi-symmetric plate-plate geometry with a needle electrode. Boundary conditions for the species densities n , the gas dynamics variables G and the electrostatic potential ϕ for each of the domain boundaries are given.

4.2.3 Geometry

We use a plate-plate geometry with a needle electrode which is shown in figure 4.2. For species densities, homogeneous Neumann boundary conditions are used on all domain boundaries. For the electric potential, a homogeneous Neumann boundary is used on the outer radial boundary. The bottom plate is grounded, while a high voltage is applied on the upper plate and the needle electrode. Furthermore, we use Neumann boundary conditions for all the equations in section 4.2.2.

4.2.4 Voltage waveform and initial conditions

The voltage waveform, shown in figure 4.3, consists of multiple identical pulses of duration $t_{\text{pulse}}=12\text{ ns}$ and separated by a time Δt_{inter} . For all the results in this work, $\Delta t_{\text{inter}} \gg t_{\text{pulse}}$ and we define the repetition frequency as the inverse of Δt_{inter} . The peak voltage V_{appl} is 40 kV, which is applied for 10 ns, and the rise and fall times of the voltage are 1 ns. In section 4.3.3 we vary the peak voltage to observe its effect on the deposited energy. As an initial condition, we use a neutral (electrons and N_2^+) background ionization density of 10^{14} m^{-3} . This background ionization provides the first electrons for streamer inception near the electrode tip, where there is significant electric field enhancement.

The neutral gas is initially at 1 bar, 300K and is stationary (i.e., $\mathbf{u} = [0, 0]$).

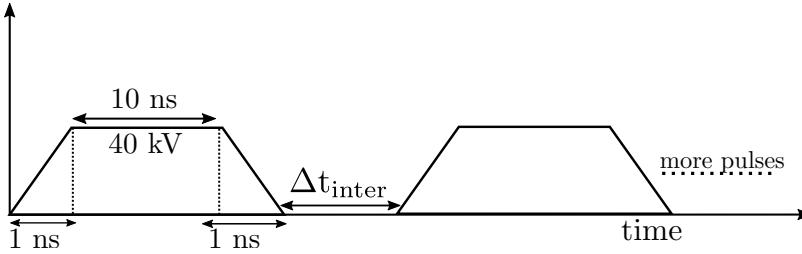


Figure 4.3: The applied voltage waveform with two identical pulses. The time between the pulses Δt_{inter} is varied to change the pulse frequency.

4.2.5 Reaction set

We use an extended reaction set from [87] by including gas temperature dependent ion-ion recombination reactions from [90], see table 4.2 given in appendix 4.5.1. The set includes reactions between electrons, and the following 13 neutral and ionic species: N_2 , O_2 , N_2^+ , O_2^+ , O_2^- , O^- , O_3^- , N_4^+ , O_4^+ , N , O , O_3 , and N_2O . Rate constants for reactions involving electron collisions were computed with BOLSIG+ [53] using the cross-sections from [88].

For simplicity, we assume that all the ions have a constant mobility $2.2 \times 10^{-4} \text{m}^2\text{V/s}$ [58], because ion motion played no major role for the results reported in this chapter.

4.3 Results and discussion

4.3.1 Main result

We apply a voltage waveform as described in section 4.2.4 with a repetition frequency of 10 kHz ($\Delta t_{\text{inter}} = 100 \mu\text{s}$) for a total duration of 2 ms. This results in a total of 20 streamers during each of the 20 voltage pulses. Furthermore, we assume at all of the discharge energy instantaneously relaxes to the neutral gas energy ϵ , i.e, we assume $\eta_f = 1$ and $\eta_s = 0$.

During each pulse, a single streamer emerged from the tip of the electrode and propagated along the negative z-axis and stopped once the voltage dropped to zero. In figure 4.4(a), we show the electric field and the electron density of streamers at the end of pulse numbers 1, 5, 10, 15 and 20. The fifth streamer is shorter than the first streamer. This is mainly caused by residual negative ions from previous pulses, from which electrons can quickly detach, as discussed in Chapter 2. Starting from pulse number 5 the streamer length increases by approximately 1 mm per 5 pulses, which results in the 20th streamer being longer than the first streamer. This can also be seen in the center panel of figure 4.5, where we plot $E_{\text{max}}^{\text{tip}}$ versus streamer length.

During each pulse, the propagating streamer deposits a certain amount of

energy which gets converted into neutral gas energy ϵ (instantaneously in this case). This increases the gas temperature inside the streamer channel, see figure 4.4(b), which causes the gas to expand resulting in a lower gas number density. The changes in temperature and gas number density are the greatest near the electrode tip, where the streamer channel has the smallest radius.

In figure 4.5, we show the streamer velocity, the radius and the maximal reduced field at the tip (E_{\max}^{tip}) versus streamer length for pulses 1, 5, 10, 15 and 20. Note that E_{\max}^{tip} for subsequent pulses is about 100 Td lower than for the first pulse. This effect is probably caused by increased electron detachment from left-over negative ions, which reduces the electric field enhancement of the discharge. There is a slight increase in streamer radius after the first pulse, which is probably related to the same effect, whereas the variation in the streamer velocity is smaller.

Effect on gas dynamics

The energy deposition by the streamers results in an increase in the gas pressure and temperature locally, causing a radially outward propagating pressure wave, which then decreases the neutral gas density locally. This phenomenon is illustrated in figure 4.6, where we see a locally heated region below the electrode tip and the start of the propagation of a pressure wave at $t = 1 \mu\text{s}$. The pressure wave, whose shape is a combination of a spherical and a cylindrical shock wave, propagates approximately 3.5 mm in $9 \mu\text{s}$, so its speed is approximately 400 m/s, which is slightly higher than the speed of sound at 300 K. Similarly shaped pressure waves have been observed in [194, 199–201]. We believe that the spherical part of the wave is caused by the relatively strong heating near the electrode tip, whereas the cylindrical part is due to the heating along the whole channel. Note that the pressure wave propagates into our electrode, because we have not yet implemented a boundary condition for the gas at the electrode surface.

The temperature in a narrow region near the tip of the electrode is about 350 K just after the first pulse. Due to the motion and the expansion of the gas, this temperature relaxes to a value slightly above 300 K at $t = 100 \mu\text{s}$. A similar relaxation can also be seen in the gas number density. This means that in our case, a single pulse only causes a minor change in the neutral gas temperature and density for the next pulse. However, when the effect of many pulses is accumulated, the result is a wider and somewhat diffuse cylindrical region in which the gas number density is lower and the temperature is higher, as illustrated in figure 4.4.

4.3.2 Effect of varying repetition frequency

We now vary the repetition frequency, while keeping all other simulation conditions the same. Figure 4.7 shows the deposited energy and the temperature

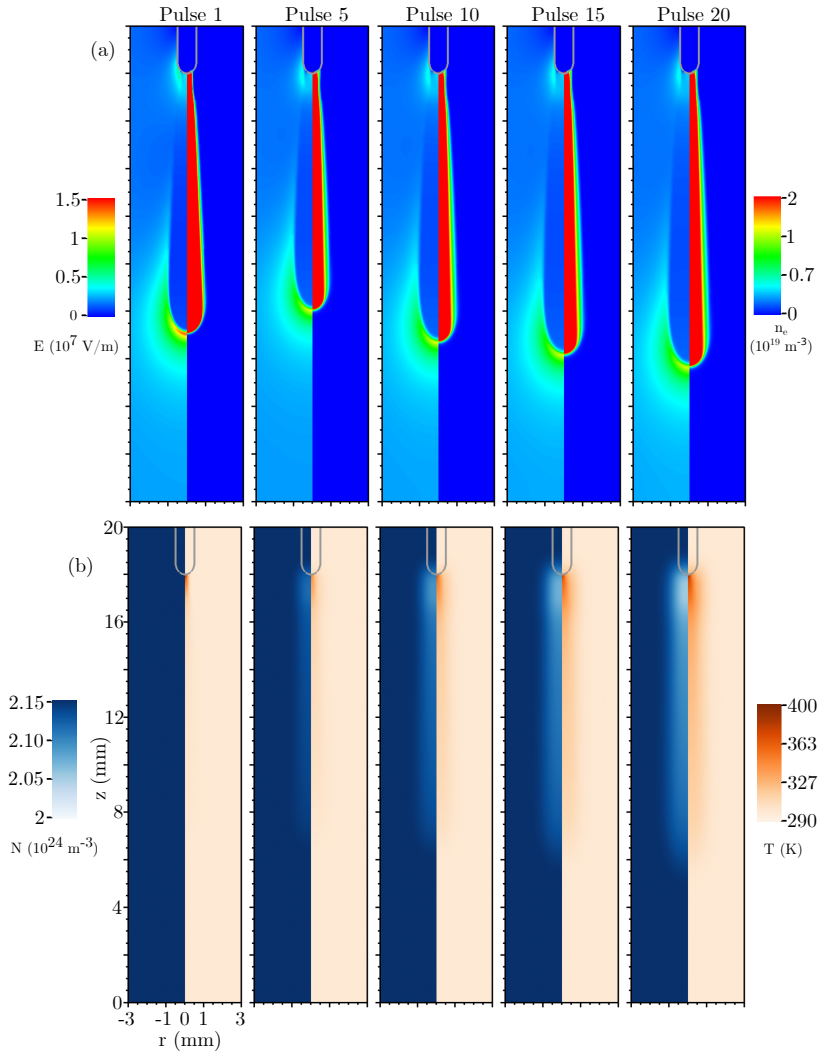


Figure 4.4: Top: electric field and electron density. Bottom: neutral gas density and temperature. The discharges are shown at the end of pulse number 1, 5, 10, 15 and 20, which correspond to times of about 12 ns, 500 μ s, 1000 μ s, 1500 μ s, and 2000 μ s. The applied voltage is 40 kV.

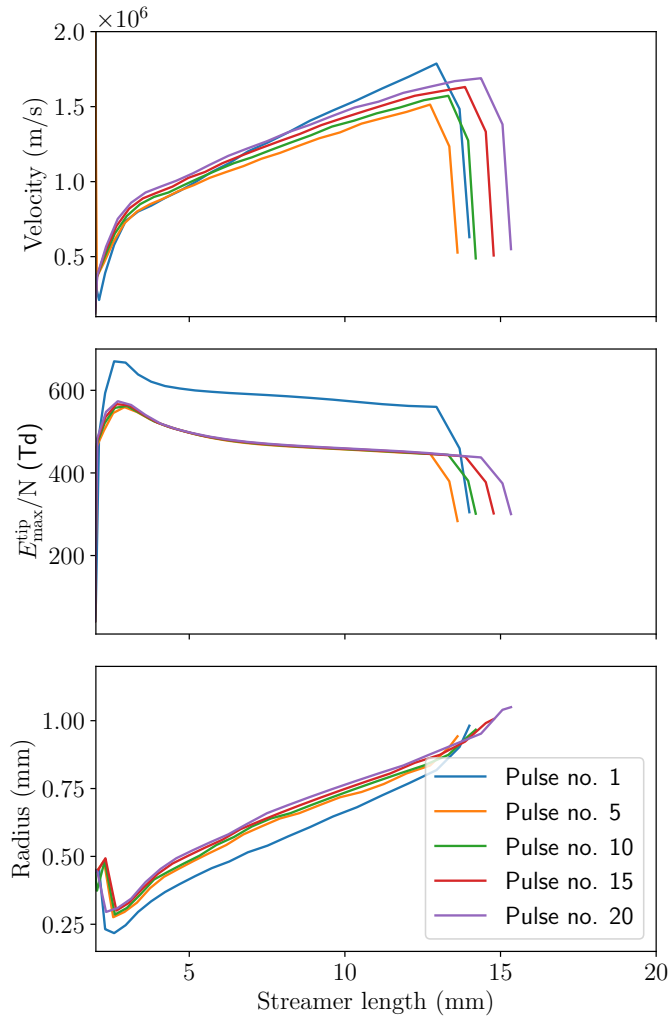


Figure 4.5: Streamer velocity, radius and reduced maximum field at their tip E_{\max}^{tip} , as a function streamer length. The cases shown correspond to figure 4.4.

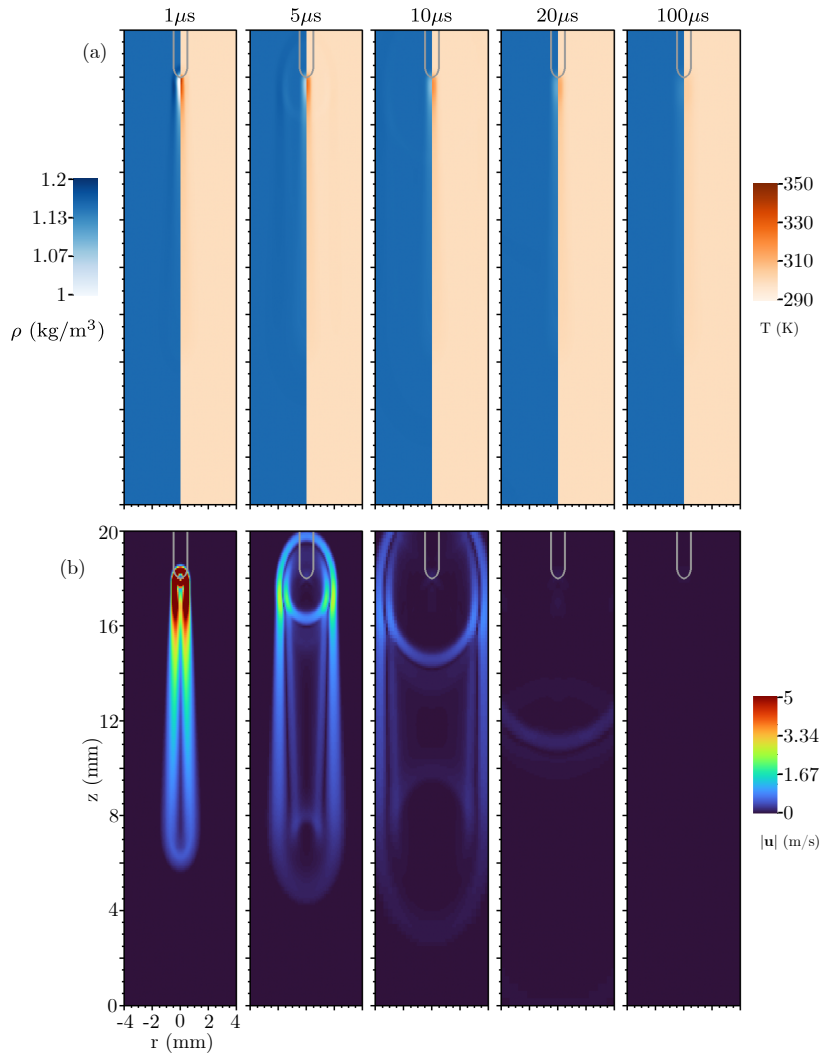


Figure 4.6: Top: neutral gas density and temperature at various times between the first and the second pulse. Bottom: norm of the gas velocity. At subsequent pulses, we observe the same qualitative behaviour.

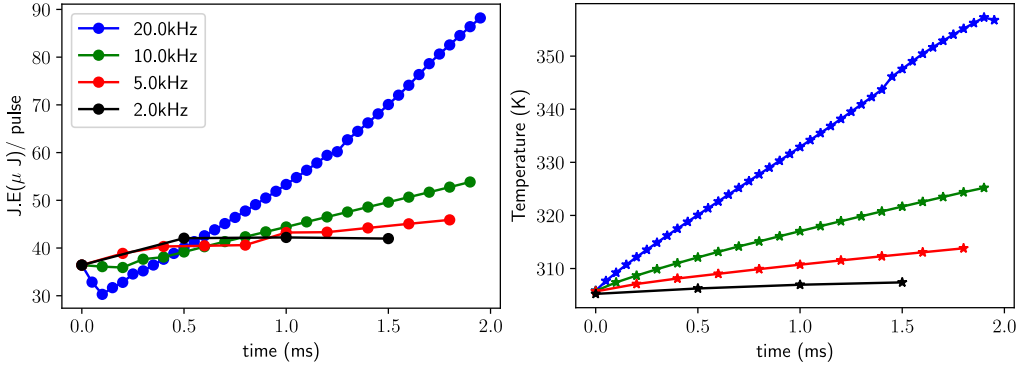


Figure 4.7: Energy deposited per pulse (top) and neutral gas temperature at $z = 13$ mm for varying repetition frequencies, at a voltage of 40 kV.

inside the streamer channel at the end of each pulse for repetition frequencies of 20 kHz, 10 kHz, 5 kHz, and 2 kHz. The deposited energy was computed by integrating the $\mathbf{j} \cdot \mathbf{E}$ term over space and time for the duration of a pulse, and the temperature was measured on-axis at $z = 13$ mm.

Clearly, a higher repetition frequency leads to a faster increase in the channel temperature, and the temperature increases approximately linearly with time in all cases. However, the energy deposited per pulse depends both on the repetition frequency and on the pulse number. With a repetition frequency of 10 kHz or 20 kHz, less energy is deposited in the second and third pulses because there is more left-over ionization. Afterwards, the energy deposited per pulse increases with the pulse number, which is probably related to a change in streamer properties, such as a larger radius and length. With a lower repetition frequency of 2 kHz or 5 kHz, the energy deposited per pulse first slightly increases and then stays more or less constant. Note however that for these cases we only simulated 4 and 10 pulses respectively, and it would be interesting to compare the temperature versus pulse number at say the 50th pulse. One would expect that at some point, a balance is obtained between the dissipation of energy by the gas (due to convection and cooling at the walls) and the heating by the discharges.

4.3.3 Effect of applied voltage

In this section, we study the effect of the applied voltage and the pulse duration on gas heating. We consider the four simulation cases listed in table 4.1, all with a repetition frequency of 10 kHz and with a simulation end time of $t = 2$ ms (i.e., 20 pulses).

Results for these cases are shown in figures 4.8 and 4.9. As expected, a higher applied voltage (and thus a higher background electric field) leads to a longer and wider discharge. When the pulse duration is increased (case d), the discharge also increases in length and to a lesser extent in width. When we compare the

Case	V_{appl} (kV)	t_{pulse} (ns)	E (V/m)
a	30	12	1.5×10^6
b	36	12	1.8×10^6
c	42	12	2.1×10^6
d	30	22	1.5×10^6

Table 4.1: Simulation conditions used to test the effect of the applied voltage. For the results presented in section 4.3.1 and 4.3.2, we used $V_{\text{appl}} = 40$ kV and $t_{\text{pulse}} = 12$ ns.

state after the first pulse and after the 20th pulse, a couple of phenomena can be observed. First, for case a (30 kV), there is a rather significant increase in streamer length. This increase is almost entirely caused by changes in discharge inception due to residual ionization, as there is no significant gas heating. Second, for case b (36 kV) and case d (30 kV, longer pulse) the energy deposited per pulse and the temperature in the streamer channel evolve in much the same way. That the length increase in case d is larger is again mostly caused by a faster inception process due to residual ionization. Third, the highest applied voltage of 42 kV (case c) clearly results in the highest energy deposited per pulse and the fastest heating rate. This streamer is therefore able to cross the discharge gap at the 20th pulse.

We can therefore conclude that effects due to gas heating will be stronger at higher applied voltages. Our results also suggest that at lower voltages it can be difficult to distinguish between effects due to gas heating and effects due residual ionization from previous pulses.

4.3.4 Effect of slow heating relaxation time

The results presented so far assume the deposited energy is instantaneously converted into neutral gas energy, i.e., $\eta_f = 1$ and $\eta_s = 0$. In this section, we assume $\eta_f = 0.5$ and $\eta_s = 0.5$ and vary the slow relaxation timescale τ_s while all the other simulation conditions are the same as in sections 4.3.1 and 4.3.2. Figure 4.10(a) shows the energy deposited per pulse for several values of τ_s . As expected, the temperature rises the fastest when $\eta_f = 1$, and for the cases with $\eta_f = 0.5$ and $\eta_s = 0.5$, it rises more slowly when τ_s is larger. The results with $\tau_s = 50 \mu\text{s}$ and $\tau_s = 250 \mu\text{s}$ are quite similar to those with $\eta_f = 1$. The reason for this is that the time between pulses is already $100 \mu\text{s}$, and a significant effect due to gas heating is only obtained after several pulses. An energy relaxation time of a few hundred μs therefore makes no significant difference. However, when τ_s is increased to $1000 \mu\text{s}$, the temperature increase becomes noticeable slower.

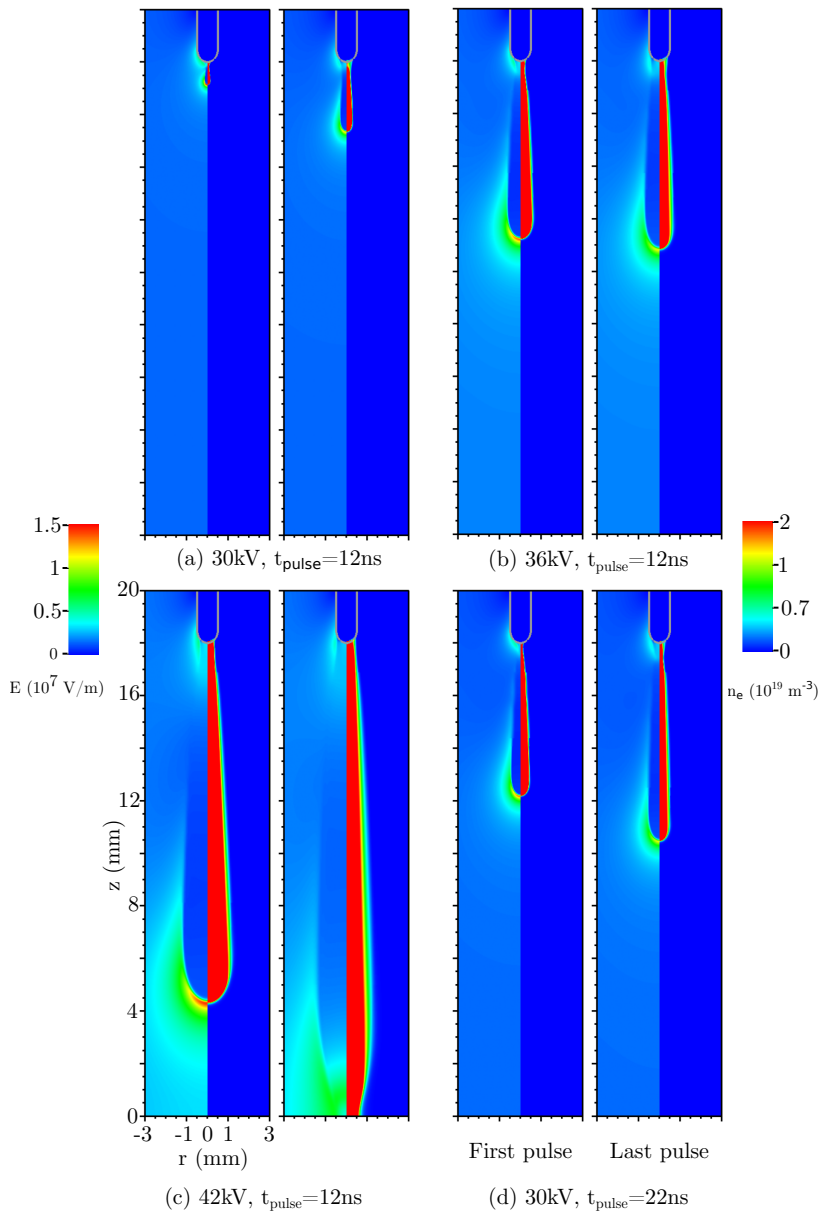


Figure 4.8: Electron density and electric field at the end of the first (left sub-panel) and at the end of the 20th pulse (right sub-panel). The applied voltage and the pulse duration are varied, as described in table 4.1. In all cases, the repetition frequency was 10 kHz.

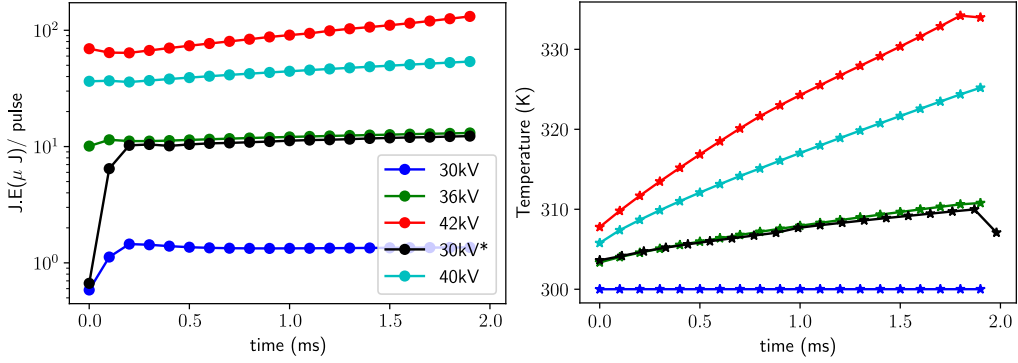


Figure 4.9: Energy deposited per pulse (top) and neutral gas temperature at $z = 13$ mm over time, for the cases shown in figure 4.8. The 30 kV* case corresponds to case (d) in table 4.1, and the 40kV case to the results from sections 4.3.1 and 4.3.2.

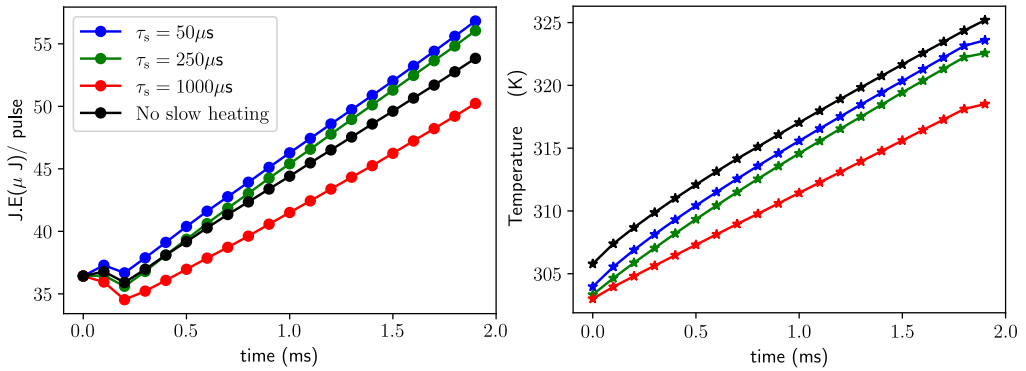


Figure 4.10: Energy deposited per pulse (top) and neutral gas temperature at $z = 13$ mm for varying slow-heating relaxation times η_s , assuming $\eta_f = 0.5$ and $\eta_s = 0.5$. The case “no slow heating” corresponds to $\eta_f = 1.0$ and $\eta_s = 0.0$, as used elsewhere in the chapter.

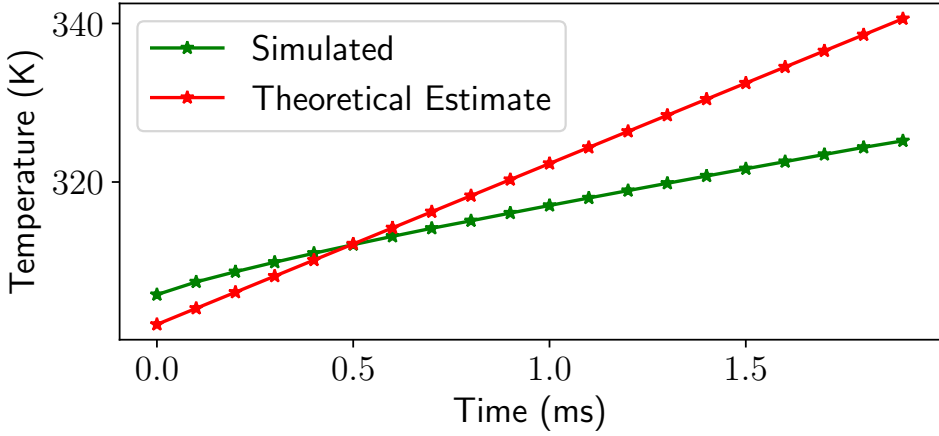


Figure 4.11: Comparison of the estimated temperature increase according to equation (4.13) with simulation results from figure 4.7 (b).

4.3.5 Estimate for temperature increase

We now provide a rough estimate for the gas temperature after the n^{th} pulse, similar to the estimates given in [87] and Chapter 2. If we assume our streamer is a cylinder of radius r and height h , in which energy is deposited uniformly, then the temperature increase ΔT due to the i^{th} pulse is

$$\Delta T = \frac{Q_i}{C_p \rho \pi r^2 h} - L, \quad (4.13)$$

where Q_i is the energy deposited by the pulse, L accounts for various heat losses due to e.g. convection, $C_p = 1000 \text{ J kg}^{-1} \text{ K}^{-1}$ is the specific heat capacity of dry air and $\rho = 1.2 \text{ kg m}^{-3}$. When L is small compared to the other term, the channel temperature will increase approximately linearly with the number of pulses, as we saw in figures 4.7, 4.9 and 4.10. It should be noted that the energy deposited per pulse in these cases did not remain constant, but this was in large part caused by an increase in streamer length and width, so that equation (4.13) was still approximately valid.

We will now compare this simple estimate with the results from section 4.3.1, assuming $L = 0$. For simplicity, we use constant values $Q_i = 45 \mu\text{J}$, $r = 0.5 \text{ mm}$ and $h = 12 \text{ mm}$. Temperature increase according to equation (4.13) is compared against the measured increase in figure 4.11. We assume that the channel temperature in our estimate to be uniform contrary to our results in figure 4.6, hence the underestimation of the temperature by our estimate.

4.4 Conclusions & outlook

We have studied the effect of gas heating in simulations of repetitively pulsed positive streamers. The simulations were performed in air at STP, using an axisymmetric drift-diffusion fluid model coupled to the compressible Euler equations for gas dynamics. We simulated up to 40 pulses and up to a time scale of 2 ms. In our results, a single streamer can temporarily increase the gas temperature by a few tens of Kelvins, in particular in the region near a pointed electrode. However, this temperature increase dissipates between pulses. After the end of a pulse, we observe shock waves emerging from the streamer channel which propagate outward with a velocity that is approximately the speed of sound, in agreement with the findings of [194, 199–201]. A persistent and significant change in gas temperature and gas number density was only obtained after multiple pulses, e.g. five or more. The lower gas number density then leads to a gradual increase in the streamer length for consecutive pulses.

We also observed effects from the residual ionization due to previous pulses, consistent with previous work in Chapter 2. These effects were found to be the most important for lower applied voltages, where the left-over ionization significantly affected discharge inception. At higher applied voltages, gas heating becomes more important. The energy deposited per pulse increases rapidly with the applied voltage, due to the larger volume of the discharge and due to the higher energy deposition per unit volume. We have studied the effect of the repetition rate, and we found that the energy deposited per pulse depends on both the pulse number and on the repetition rate.

The coupling between the discharge and the gas dynamics was done with a simple model with three coefficients: two factors that control the ratio of slow and fast heating, and an energy relaxation time scale slow heating. Our results were not sensitive to the particular choice of these parameters, as long as the energy relaxation time scale was comparable (and not much larger) than the time between pulses.

In future work, several aspects of our model could be improved. For example, a larger computational domain could be used, and the boundary conditions for the gas and plasma species could be made more realistic. This could also improve the description of the heat loss due cooling of the gas at the domain walls. Furthermore, a more extensive plasma chemistry could be used, in which for example the effect of gas dissociation on the gas number density is taken into account.

4.5 Appendix

4.5.1 Reaction set used in this chapter

Table 4.2: T (K) and T_e (K) are gas and electron temperatures, respectively. T_e is computed as $T_e = 2\epsilon_e/3k_B$ with the mean electron energy ϵ_e obtained from BOLSIG+ [96].

No.	Reaction	Reaction rate coefficient($\text{m}^6 \text{s}^{-1}$ or $\text{m}^3 \text{s}^{-1}$)	Reference
Electron-ionization			
R1	$e + \text{O}_2 \rightarrow 2e + \text{O}_2^+$	$k_1(E/N)$	[88]
R2	$e + \text{N}_2 \rightarrow 2e + \text{N}_2^+$ (15.6 eV)	$k_2(E/N)$	[88]
R3	$e + \text{N}_2 \rightarrow 2e + \text{N}_2^+$ (18.8 eV)	$k_3(E/N)$	[88]
Electron-attachment			
R4	$e + \text{O}_2 + \text{O}_2 \rightarrow \text{O}_2^- + \text{O}_2$	$k_4(E/N)$	[88]
R5	$e + \text{O}_2 \rightarrow \text{O}^- + \text{O}$	$k_5(E/N)$	[88]
Electron-detachment			
R6	$\text{O}_2^- + \text{M} \rightarrow e + \text{O}_2 + \text{M}$	$k_6 = 1.24 \times 10^{-17} \exp(-(\frac{179}{8.8+E/N})^2)$	[95]
R7	$\text{O}^- + \text{N}_2 \rightarrow e + \text{N}_2\text{O}$	$k_7 = 1.16 \times 10^{-18} \exp(-(\frac{48.9}{11+E/N})^2)$	[95]
Electron-ion recombination			
R8	$e + \text{N}_4^+ \rightarrow 2\text{N}_2$	$k_8 = 2 \times 10^{-12} (300/T_e)^{\frac{1}{2}}$	[90]
R9	$e + \text{O}_4^+ \rightarrow 2\text{O}_2$	$k_9 = 1.4 \times 10^{-12} (300/T_e)^{\frac{1}{2}}$	[90]
Negative-ion conversion			
R10	$\text{O}^- + \text{O}_2 \rightarrow \text{O}_2^- + \text{O}$	$k_{10} = 6.96 \times 10^{-17} \exp(-(\frac{198}{5.6+E/N})^2)$	[95]
R11	$\text{O}^- + \text{O}_2 + \text{M} \rightarrow \text{O}_3^- + \text{M}$	$k_{11} = 1.1 \times 10^{-42} \exp(-(\frac{E/N}{65})^2)$	[95]
Positive-ion conversion			
R12	$\text{N}_2^+ + \text{O}_2 \rightarrow \text{O}_2^+ + \text{N}_2$	$k_{12} = 6 \times 10^{-17} (300/T)^{\frac{1}{2}}$	[90]
R13	$\text{N}_2^+ + \text{N}_2 + \text{M} \rightarrow \text{N}_4^+ + \text{M}$	$k_{13} = 5 \times 10^{-41} (300/T)^2$	[90]
R14	$\text{N}_4^+ + \text{O}_2 \rightarrow \text{O}_2^+ + 2\text{N}_2$	$k_{14} = 2.5 \times 10^{-16}$	[90]
R15	$\text{O}_2^+ + \text{O}_2 + \text{M} \rightarrow \text{O}_4^+ + \text{M}$	$k_{15} = 2.4 \times 10^{-42} (300/T)^3$	[90]
Ion-ion recombination			
R16	$\text{N}_2^+ + \text{O}^- \rightarrow \text{N} + \text{N} + \text{O}$	$k_{16} = 10^{-13}$	[90]
R17	$\text{N}_2^+ + \text{O}_2^- \rightarrow \text{N} + \text{N} + \text{O}_2$	$k_{17} = 10^{-13}$	[90]
R18	$\text{N}_2^+ + \text{O}_3^- \rightarrow \text{N} + \text{N} + \text{O}_3$	$k_{18} = 10^{-13}$	[90]
R19	$\text{O}_2^+ + \text{O}^- \rightarrow \text{O} + \text{O} + \text{O}$	$k_{19} = 10^{-13}$	[90]
R20	$\text{O}_2^+ + \text{O}_2^- \rightarrow \text{O} + \text{O} + \text{O}_2$	$k_{20} = 10^{-13}$	[90]
R21	$\text{O}_2^+ + \text{O}_3^- \rightarrow \text{O} + \text{O} + \text{O}_3$	$k_{21} = 10^{-13}$	[90]

Table 4.2: (Continued.)

No.	Reaction	Reaction rate coefficient($\text{m}^6 \text{s}^{-1}$ or $\text{m}^3 \text{s}^{-1}$)	Reference
R22	$\text{O}_4^+ + \text{O}^- \rightarrow \text{O}_2 + \text{O}_2 + \text{O}$	$k_{22} = 10^{-13}$	[90]
R23	$\text{O}_4^+ + \text{O}_2^- \rightarrow \text{O}_2 + \text{O}_2 + \text{O}_2$	$k_{23} = 10^{-13}$	[90]
R24	$\text{O}_4^+ + \text{O}_3^- \rightarrow \text{O}_2 + \text{O}_2 + \text{O}_3$	$k_{24} = 10^{-13}$	[90]
R25	$\text{N}_4^+ + \text{O}^- \rightarrow \text{N}_2 + \text{N}_2 + \text{O}$	$k_{25} = 10^{-13}$	[90]
R26	$\text{N}_4^+ + \text{O}_2^- \rightarrow \text{N}_2 + \text{N}_2 + \text{O}_2$	$k_{26} = 10^{-13}$	[90]
R27	$\text{N}_4^+ + \text{O}_3^- \rightarrow \text{N}_2 + \text{N}_2 + \text{O}_3$	$k_{27} = 10^{-13}$	[90]
R28	$\text{N}_2^+ + \text{O}^- + \text{M} \rightarrow \text{N}_2\text{O} + \text{M}$	$k_{28} = 2 \times 10^{-37} (300/T)^{(2.5)}$	[90]
R29	$\text{N}_2^+ + \text{O}^- + \text{M} \rightarrow \text{N}_2 + \text{O} + \text{M}$	$k_{29} = 2 \times 10^{-37} (300/T)^{(2.5)}$	[90]
R30	$\text{N}_2^+ + \text{O}^- \rightarrow \text{N}_2 + \text{O}$	$k_{30} = 2 \times 10^{-13} (300/T)^{(0.5)}$	[90]
R31	$\text{N}_2^+ + \text{O}^- + \text{M} \rightarrow \text{N}_2\text{O} + \text{M}$	$k_{31} = 2 \times 10^{-37} (300/T)^{(2.5)}$	[90]
R32	$\text{N}_2^+ + \text{O}^- + \text{M} \rightarrow \text{N}_2 + \text{O} + \text{M}$	$k_{32} = 2 \times 10^{-37} (300/T)^{(2.5)}$	[90]
R33	$\text{N}_2^+ + \text{O}^- \rightarrow \text{N}_2 + \text{O}$	$k_{33} = 2 \times 10^{-13} (300/T)^{(0.5)}$	[90]
R34	$\text{N}_2^+ + \text{O}_2^- + \text{M} \rightarrow \text{N}_2 + \text{O}_2 + \text{M}$	$k_{34} = 2 \times 10^{-37} (300/T)^{(2.5)}$	[90]
R35	$\text{N}_2^+ + \text{O}_2^- \rightarrow \text{N}_2 + \text{O}_2$	$k_{35} = 2 \times 10^{-13} (300/T)^{(0.5)}$	[90]
R36	$\text{N}_2^+ + \text{O}_3^- \rightarrow \text{N}_2 + \text{O}_3$	$k_{36} = 2 \times 10^{-13} (300/T)^{(0.5)}$	[90]
R37	$\text{O}_2^+ + \text{O}^- + \text{M} \rightarrow \text{O}_3 + \text{M}$	$k_{37} = 2 \times 10^{-37} (300/T)^{(2.5)}$	[90]
R38	$\text{O}_2^+ + \text{O}^- + \text{M} \rightarrow \text{O} + \text{O}_2 + \text{M}$	$k_{38} = 2 \times 10^{-37} (300/T)^{(2.5)}$	[90]
R39	$\text{O}_2^+ + \text{O}^- \rightarrow \text{O}_2 + \text{O}$	$k_{39} = 2 \times 10^{-13} (300/T)^{(0.5)}$	[90]
R40	$\text{O}_2^+ + \text{O}_2^- + \text{M} \rightarrow 2\text{O}_2 + \text{M}$	$k_{40} = 2 \times 10^{-37} (300/T)^{(2.5)}$	[90]
R41	$\text{O}_2^+ + \text{O}_2^- \rightarrow \text{O}_2 + \text{O}_2$	$k_{41} = 2 \times 10^{-13} (300/T)^{(0.5)}$	[90]
R42	$\text{O}_2^+ + \text{O}_3^- \rightarrow \text{O}_2 + \text{O}_3$	$k_{42} = 2 \times 10^{-13} (300/T)^{(0.5)}$	[90]

Chapter 5

Calculating radio emissions of positive streamer phenomena using 3D simulations

We study radio emissions from positive streamers in air using 3D simulations, from which the radiated electric field is computed by solving Jefimenko's equations. The simulations are performed at 0.5 bar using two photoionization methods: the Helmholtz approximation for a photon density and a Monte Carlo method using discrete photons, with the latter being the most realistic. We consider cases with single streamers, streamer branching, streamers interacting with preionization and streamer-streamer encounters. We do not observe a strong VHF radio signal during or after branching, which is confirmed by lab experiments. This indicates that the current inside a streamer discharges evolves approximately continuously during branching. On the other hand, stochastic fluctuations in streamer propagation due to Monte Carlo photoionization lead to more radio emission being emitted at frequencies of 100 MHz and above. Another process that leads to such high-frequency emission is the interaction of a streamer with a weakly preionized region, for example present due to a previous discharge. In agreement with previous work, we observe the strongest and highest-frequency emission from streamer encounters. The amount of total energy that is radiated seems to depend primarily on the background electric field, and less on the particular streamer evolution. Finally, we present approximations for the maximal current along a streamer channel and a fit formula for a streamer's current moment.

This chapter is submitted and under revision as [\[202\]](#):
Hemaditya Malla, Yihao Guo, Brian.M. Hare, Steven Cummer, Alejandro Malagón-Romero, Ute Ebert, Sander Nijdam, Jannis Teunissen. Calculating radio emissions of positive streamer phenomena using 3D simulations. *Submitted to the Journal of Geophysical Research– Atmospheres*

The appendix on experimental results was written by Y. Guo and S. Nijdam.

5.1 Introduction

Streamer discharges determine the initial stages of electric breakdown in air and other gases [31]. In a tropospheric discharge they form streamer bursts that pave the way of lightning leaders, and streamers appear as sprite discharges in the mesosphere. Streamers are space-charge dominated, fast growing plasma filaments with an intricate inner structure. Due to their non-equilibrium nature, they efficiently create nitrogen oxides and ozone, and they also can contribute to electron runaway and consecutive further high energy radiation.

It is difficult to capture the optical light emission from streamers within a thundercloud, because light is scattered multiple times inside clouds. Besides visible light, streamers and related lightning phenomena emit electromagnetic radiation across a wide frequency range, from radio frequencies (RF) to microwaves [203] and beyond [204]. Since thunderclouds are transparent to radio emissions in the 3 kHz–300 GHz range, such emission can help to understand the phenomena taking place inside a thundercloud [205, 206].

Brooks *et al* [207] already measured the radiated electric field from lightning and suggested that the emissions from streamer discharges are in the VHF–UHF range, with VHF (very high frequency) corresponding to 30–300 MHz and UHF (ultra high frequency) corresponding to 0.3–3 GHz. In recent years, several authors have studied radio emissions from streamer discharges using axisymmetric simulations. Shi *et al* [208] simulated streamer inception from hydrometeors in fields above and below the critical field E_k , and computed the radiated electromagnetic field using the approximations presented in [209]. Alejandro Luque [210] performed a full electrodynamic simulation of counter-propagating streamers and their “collision” at atmospheric pressure at sub-breakdown conditions. Such collisions were observed to emit radiation in the range from 100 MHz to a few GHz. Shi *et al* [211] later studied streamer collisions in background electric fields above E_k , and Koile *et al* [212] studied collisions in fields below and above E_k . In all these studies, it was found that the background electric field was an important factor controlling the magnitude of the radio emissions. Furthermore, Garnung *et al* [213] studied the emissions of streamer collisions when they occur inside sprites, and they demonstrated that such phenomena could be detected by radio telescopes.

Radio emissions from streamers have recently also been measured experimentally both in the laboratory and from natural lightning. Parkevich, Shpakov *et al* [214] and Parkevich, Khirianova *et al* [215] performed laboratory experiments to measure the radio emissions from streamer discharges and found that streamer formation processes emit electromagnetic radiation in the MHz–GHz range. Guschin *et al* [216] performed laboratory experiments by charging a cloud of water droplets to trigger streamer discharges, and measured electromagnetic radiation in the microwave to UHF range.

In natural lightning, VHF and higher frequency radio emissions are routinely

observed from almost all negative leaders, presumably from negative polarity streamers. In contrast, VHF radio emissions from positive leaders and thus positive streamers are much weaker and often undetectable. Pu *et al* [217] reported VHF measurements from a strong and very close positive CG leader and found a VHF spectrum that was mostly flat up until 80 MHz above which it dropped steeply in amplitude. Pu *et al* [218] looked at fast positive breakdown (admittedly an extreme case for positive streamers) and measured a flat VHF-UHF spectrum all the way up to almost 400 MHz. And [219] looked for VHF emissions from in-cloud positive leaders and found none despite the very high sensitivity of the LOFAR array. These three scenarios are all different, but they do show that VHF radio emissions from positive streamers is quite variable, and the underlying mechanism of VHF emissions from positive streamers in natural lightning is poorly understood.

Typical time scales in a discharge scale approximately inversely with the gas number density N [37], which means that typical frequencies scale as $1/N$. The same type of phenomena can therefore result in radio emission at different frequencies depending on their altitude. For example, the emissions from head-on sprite streamer collisions at an altitude of 70 km occur in a spectral range from a few kHz up to a few hundred kHz [213], whereas the corresponding spectral range for streamer collisions at atmospheric pressure is a few hundred MHz up to a few GHz [210, 211].

In this chapter, we for the first time compute radio emissions from 3D simulations of positive streamers in air, and we calculate the different spatial components of the electric field at a horizontal distance of 1 km from the approximately vertical discharges. We consider several cases involving single streamers, streamer branching, the interaction of streamers with a preionized channel and a collision between streamers of opposite polarity. The simulations are performed with a 3D fluid model in sub-breakdown conditions. We consider two approaches for photoionization: the so-called Helmholtz approximation where photons are approximated as a density and a Monte Carlo method that takes the full discrete nature of the photons into account [51]. We compute the radiated electric field for all these cases by directly solving Jefimenko's equations for the computed charge density and current density. Another novel aspect of our work is that we use so-called scaleograms, computed using wavelet analysis, to show how the emission spectrum evolves over time. We also provide simple estimates for the current and the current moment of a streamer discharge. Furthermore, an extensive appendix is included in which we present laboratory measurements of the discharge current and the emitted radiation during streamer branching events.

The chapter is organized as follows. We first present the simulation model and the methods for computing and analyzing the radiated field in section 5.2. Results for all the simulation cases are presented and discussed in section 5.3. Finally, we give numerical details on the solution of Jefimenko's equation in section 5.5.2 and we present experimental results on the effect of branching on

Table 5.1: List of reactions included in the model.

Reaction	Rate coefficient
$e + N_2 \xrightarrow{k_1} e + e + N_2^+ (15.60 \text{ eV})$	$k_1(E/N)$
$e + N_2 \xrightarrow{k_2} e + e + N_2^+ (18.80 \text{ eV})$	$k_2(E/N)$
$e + O_2 \xrightarrow{k_3} e + e + O_2^+$	$k_3(E/N)$
$e + O_2 + O_2 \xrightarrow{k_4} O_2^- + O_2$	$k_4(E/N)$
$e + O_2 \xrightarrow{k_5} O^- + O$	$k_5(E/N)$
$e + N_2 \xrightarrow{k_6} e + N_2(C^3\Pi_u)$	$k_6(E/N)$
$N_2(C^3\Pi_u) + N_2 \xrightarrow{k_7} N_2 + N_2$	$k_7 = 0.13 \times 10^{-16} \text{ m}^3\text{s}^{-1}$
$N_2(C^3\Pi_u) + O_2 \xrightarrow{k_8} N_2 + O_2$	$k_8 = 3.0 \times 10^{-16} \text{ m}^3\text{s}^{-1}$
$N_2(C^3\Pi_u) \xrightarrow{k_9} N_2(B^3\Pi_g)$	$k_9 = 1/(42 \text{ ns})$

the streamer current in section 5.5.1.

5.2 Simulation method

We perform full 3D streamer simulations with the classical drift-diffusion-reaction fluid model using the open-source `afivo-streamer` code [44, 45]. For a comparison of this model against experiments and against particle simulations see [87] and [50]. We briefly summarize the main aspects of the model below, further details are given e.g. in [44] and Chapter 2.

5.2.1 Model

In the classical drift-diffusion-reaction fluid model the electron density n_e evolves in time as

$$\partial_t n_e = \nabla \cdot (\mu_e \mathbf{E} n_e + D_e \nabla n_e) + S_e + S_{\text{ph}}, \quad (5.1)$$

where μ_e is the electron mobility coefficient, D_e the diffusion coefficient, \mathbf{E} is the electric field, S_e the source (and sink) term of free electrons due to the processes listed in table 5.1, and S_{ph} is the photo-ionization source term. In this chapter, we consider relatively short time scales of up to about 120 ns at 500 mbar; this pressure corresponds to an altitude of about 5 km according to the 1976 US standard atmosphere. The motion of ion and neutral species is therefore not taken into account, so that their densities n_i (for $i = 1, \dots, n$) evolve as

$$\partial_t n_i = S_i, \quad (5.2)$$

where the S_i are the respective source terms due to reactions. We use the same reactions as [87]; they are given in table 5.1.

The electron transport coefficients and the electron-neutral reaction rates k_1 to k_6 are assumed to depend on the reduced local electric field (local field approximation) E/N , where N is the gas number density. These coefficients

were computed using BOLSIG- [53] using Phelps' cross-section data for N₂ and O₂ [88]. We compute optical light emission from the second positive system of N₂ using the reaction rates given by [92]. They are given in the last three rows in table 5.1.

The photoionization source term S_{ph} is computed using Zheleznyak's model [35], using either the continuum approach like in [47] or the discrete Monte-Carlo approach as in e.g. [51, 158]. The discrete approach is the most realistic, as it takes the quantization of the photons into account and therefore reproduces the stochastic fluctuations in the electron density ahead of a streamer that should physically be there. These fluctuations are an important trigger for the branching of streamers, and including them in a model can reproduce the branching observed in experiments [158]. The Helmholtz approach has the practical advantage that streamers develop non-stochastically, which can make it easier to study how certain conditions affect the streamer's development. The two photoionization approaches are compared in section 5.3.1, and the discrete approach is used in section 5.3.3 to obtain branching streamers.

The electric field \mathbf{E} is calculated in the electrostatic approximation as $\mathbf{E} = -\nabla\phi$. Here ϕ is the electrostatic potential, which is obtained by solving the Poisson equation with a multigrid method [45]

$$\nabla^2\phi = -\rho/\epsilon_0, \quad (5.3)$$

where ρ is the charge density and ϵ_0 is the vacuum permittivity. The electric potential is fixed on the bottom and top of the domain, and homogeneous Neumann boundary conditions are used on the other sides which means that the electrical field is parallel to these lateral boundaries. In this way, a homogeneous background electric field E_{bg} is applied. For species densities, homogeneous Neumann boundary conditions are used on all domain boundaries, but simulations are stopped before the discharges get close to a boundary.

5.2.2 Computational domain

All simulations are performed in a domain of $(30\text{ cm})^3$, which is illustrated in figure 5.1. This domain contains dry air (80% N₂, 20% O₂) at a pressure of 500 mbar. The simulations are performed with adaptive mesh refinement (AMR), as described in [44].

5.2.3 Initial conditions

To start electric discharges we place one or more elongated ionized seeds in the domain. These seeds are initially electrically neutral. In the background field they rapidly become polarized, and hence they provide field enhancement and initial electrons, which are both needed for streamer inception. We use electrically neutral seeds defined by a vertical line segment of 12 mm and a "radius" $r_s = 0.5\text{ mm}$

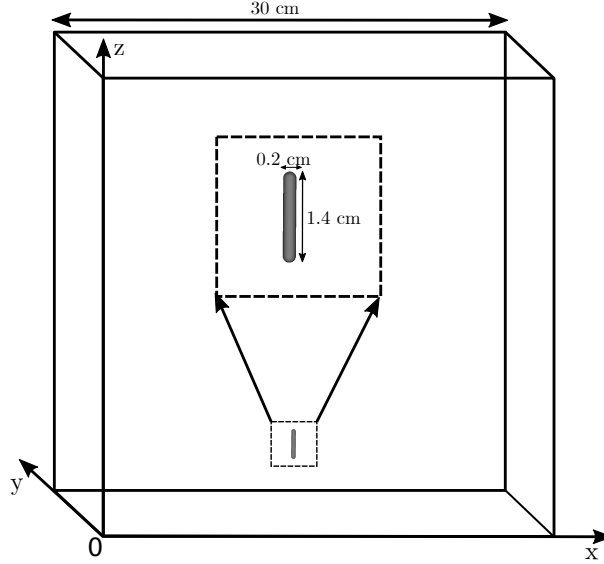


Figure 5.1: The $(30 \text{ cm})^3$ computational domain, with a zoom into the initial ionization seed in the inlay; such seeds are used to start discharges, see section 5.2.3. Table 5.2 lists the locations of the seeds for the different cases considered in this chapter.

(we remark that the actual radius is larger due to the decay profile). The density of electrons and O_2^+ ions along the seed is given by $n_{\text{seed}} \cdot f_{\text{ss}}[(d - r_s)/r_s]$, where d is the distance from the line segment, $n_{\text{seed}} = 2.5 \cdot 10^{19} \text{ m}^{-3}$ and f_{ss} is a smooth step function defined by $f_{\text{ss}}(x) = 1 - 3x^2 + 2x^3$ for $0 \leq x \leq 1$, $f_{\text{ss}}(x) = 1$ for $x < 0$ and $f_{\text{ss}}(x) = 0$ for $x > 1$. An example of such a seed is shown in figure 2.1. Discharge inception occurs approximately 10 ns after the start of the simulation.

5.2.4 Calculating the radiated electric field

According to a reformulation of the Maxwell equations, the electromagnetic field at a point of observation \mathbf{r} due to an evolving space charge distribution can be computed using Jefimenko's equations [220, 221]

$$\mathbf{E}(\mathbf{r}, t) = \frac{1}{4\pi\epsilon_0} \int \left[\frac{\rho(\mathbf{r}', t_r)}{\mathcal{R}^2} \hat{\mathcal{R}} + \frac{1}{c\mathcal{R}} \partial_t \rho(\mathbf{r}', t_r) \hat{\mathcal{R}} - \frac{1}{c^2\mathcal{R}} \partial_t \mathbf{j}(\mathbf{r}', t_r) \right] d^3\mathbf{r}', \quad (5.4)$$

$$\mathbf{B}(\mathbf{r}, t) = \frac{\mu_0}{4\pi} \int \left[\frac{\mathbf{j}(\mathbf{r}', t_r)}{\mathcal{R}^2} + \frac{1}{c\mathcal{R}} \partial_t \mathbf{j}(\mathbf{r}', t_r) \right] \times \hat{\mathcal{R}} d^3\mathbf{r}', \quad (5.5)$$

where $\mathcal{R} = |\mathbf{r} - \mathbf{r}'|$, $\hat{\mathcal{R}} = (\mathbf{r} - \mathbf{r}')/|\mathbf{r} - \mathbf{r}'|$, c is the speed of light, ρ is the charge density, \mathbf{j} is the current density, and t_r is the retarded time given by

$$t_r = t - \mathcal{R}/c. \quad (5.6)$$

Equations (5.4) and (5.5) are time-dependent generalizations of Coulombs' and Biot-Savart's laws respectively, where the first term in each of these equations corresponds to the static case, and decays like $1/\mathcal{R}^2$. Our interest here is in the radiated fields, which correspond to the terms that drop as $1/\mathcal{R}$:

$$\mathbf{E}_{\text{rad}}(\mathbf{r}, t) = \frac{1}{4\pi\epsilon_0} \int \left[\frac{1}{c\mathcal{R}} \partial_t \rho(\mathbf{r}', t_r) \hat{\mathcal{R}} - \frac{1}{c^2\mathcal{R}} \partial_t \mathbf{j}(\mathbf{r}', t_r) \right] d^3\mathbf{r}', \quad (5.7)$$

$$\mathbf{B}_{\text{rad}}(\mathbf{r}, t) = \frac{\mu_0}{4\pi} \int \frac{1}{c\mathcal{R}} \partial_t \mathbf{j}(\mathbf{r}', t_r) \times \hat{\mathcal{R}} d^3\mathbf{r}'. \quad (5.8)$$

We numerically compute $\mathbf{E}_{\text{rad}}(\mathbf{r}_{\text{obs}}, t)$ at a certain observation location \mathbf{r}_{obs} using the output of ρ and $\mathbf{j} = e\mu_e n_e \mathbf{E}$ from our simulations. The details of this procedure are described in 5.5.2. Values for $\mathbf{E}_{\text{rad}}(\mathbf{r}_{\text{obs}}, t)$ are typically computed every 0.5 ns, which corresponds to a sampling rate of 2 GHz. However, for the cases in a background electric field of 10 kV/cm we use a higher sampling rate of 20 GHz.

We remark that in previous work considering axisymmetric simulations, authors have typically used the relation

$$E_{\text{rad}} = c B_{\text{rad}}. \quad (5.9)$$

This relation stems from the far field approximation for electromagnetic waves in vacuum as discussed in more detail in 5.6. For a line current $I(z, t)$ in the vertical z direction, the ϕ component of the radiated magnetic field from equation (5.8) can be computed as

$$B_{\text{rad},\phi}(\mathbf{r}, t) = \frac{\mu_0}{4\pi} \int \frac{\sin\theta}{c\mathcal{R}} \partial_t I(z, t_r) dz, \quad (5.10)$$

where θ is the polar angle of the receiver with respect to the source location, see e.g. [208, 213]. For a far-away observer E_{rad} can further be approximated as

$$E_{\text{rad}}(\mathbf{r}, t) \approx \frac{\mu_0}{4\pi} \frac{\sin\theta}{\mathcal{R}} \partial_t M(t_r), \quad (5.11)$$

where $M(t)$ is the current moment obtained by integrating $I(z, t)$ over z , see e.g. [222]. Note that the variation in t_r along the source is not taken into account in equation (5.11). This is a good approximation when $\sin\theta \approx 1$ or when the spatial extent of the source is small compared to the shortest wavelength of interest.

In the present chapter we work directly with equation (5.4) since we will consider 3D simulations in which currents can flow in all directions, and since we were not sure beforehand what kind of approximations we could make. (In hindsight, we probably could have used equation (5.11)). Details about the numerical evaluation of equation (5.4) on an AMR grid are given in 5.5.2.

Note that the effect of the radiated electric field on the discharge itself is not taken into account here, as this effect would typically be very small and because this requires a much more expensive electrodynamic computation of the fields and their influence on the discharge evolution. As discussed in [210], there could be a noticeable effect of the radiated field on encounters between streamers of opposite polarities, due to the very rapid change in the current.

5.2.5 Time-frequency analysis procedure

We perform a time-frequency analysis of $\mathbf{E}_{\text{rad}}(\mathbf{r}_{\text{obs}}, t)$ using a continuous wavelet transform (CWT) [223, 224], as implemented in the open-source python package `PyWavelets` [225]. With this approach, we obtain spectrograms (or more specifically scaleograms, as they are called when doing wavelet analysis) that show how different frequencies are emitted as a function of time. An example is shown in figure 5.2. For our CWT, we use a Complex-Morlet wavelet [226] with a central frequency of 1 GHz and scale range of [0.1, 100] so that it can resolve frequencies in the range 10 MHz-10 GHz.

The signals we are considering are non-periodic, so some assumption has to be made about the continuation of these signals outside the considered time window. The regions where values are affected by the boundaries of the signal are indicated in figure 5.2. We here assume the signal is extended with a constant value, so that if the signal $f(t)$ is given from $t = 0$ to $t = T$, we have $f(-T/2 < t < 0) = f(0)$ and $f(T < t < T+T/2) = f(T)$. In general, \mathbf{E}_{rad} at later times will of course not be constant, but this simple assumption has the advantage that $f(t)$ is continuous and that no strong artificial emission occurs due to boundary effects.

5.3 Results

In the subsections below we present the simulation cases that are summarized in table 5.2. The used background electric fields E_{bg} range from 6 kV/cm to 10 kV/cm, which correspond to about 40% to 67% of the critical field at 500 mbar. Since we fix the electric potential on top and bottom of our computational domain, streamers will experience a higher effective field when they have crossed a significant part of the gap, because the field in their channels will typically be much lower than E_{bg} . In all cases, the radiated field is computed at $\mathbf{r}_{\text{obs}} = (0, 1 \text{ km}, 0)$, i.e., at 1 km distance in the $+y$ direction.

5.3.1 Single streamer propagation

Smooth propagation with Helmholtz photoionization

We first simulate a single, non-branching positive streamer starting from a single ionized seed as described in table 5.2, using the Helmholtz photoionization

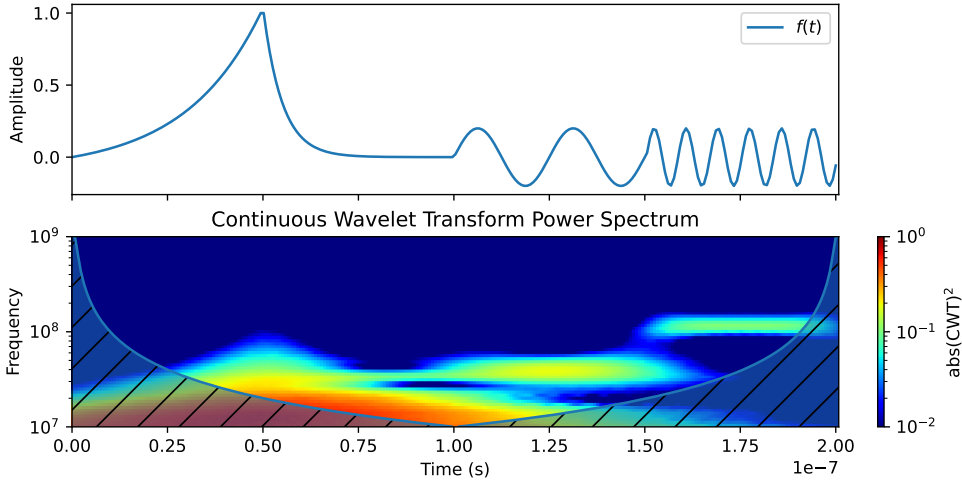


Figure 5.2: Example of a scaleogram for an artificial signal $f(t)$ consisting of four parts: exponential growth and decay with time constants $\tau = 20$ ns and $\tau = 5$ ns, and sine waves with frequencies of 40 MHz and 120 MHz. The signal was sampled at 256 points. Shown is the so-called power spectrum, in which the color indicates the power in the signal as a function of frequency and time. The regions where values are uncertain due to boundary effects are shaded.

Table 5.2: List of simulation parameters. E_{bg} indicates the background field. All simulations are performed at 500 mbar and 300K in a 80%:20% $\text{N}_2:\text{O}_2$ gas mixture, so that the critical field is about $E_k \approx 15$ kV/cm. The coordinates of the initial seeds (as described in section 5.2.3) are also given. Photoionization is either included with a Helmholtz approximation or with discrete Monte Carlo photons (MC), see section 5.2.1.

Description	Section	E_{bg}/E_k	Seed(s) (x, y, z) (cm)	Photoionization
Single streamers	5.3.1	0.40	(15, 15, 10.8)	Helmholtz & MC
Double-headed streamer	5.3.2	0.67	(15, 15, 10.8)	Helmholtz
Guided streamer branching	5.3.3	0.53	(15, 15, 10.8)	MC
Interaction with preionization	5.3.4	0.40	(15, 15, 10.8)	Helmholtz
Streamer collision	5.3.5	0.67	(15, 15, 12.0), (15, 15, 16.8)	Helmholtz

method. Figure 5.3 shows the time evolution of the electron density, the resulting radiated electric field \mathbf{E}_{rad} for an observer at $\mathbf{r}_{\text{obs}} = (0, 1 \text{ km}, 0)$, and scaleograms of the different components of \mathbf{E}_{rad} . The streamer propagates to a length of 10 cm in 120 ns, with an average velocity of about 10^6 m/s . As expected, the x and y components of \mathbf{E}_{rad} are negligible, and the z component points opposite to the background electric field. The streamer initially emits weakly in the 10 MHz range, but as its length increases both the magnitude and the frequency of the emissions increases, as shown in the scaleograms in figure 5.3. However, the radiation below 20 MHz remains dominant in amplitude and above 20 MHz the strength falls quickly. This shape of the radiation spectrum is distinctly different from that reported for strong positive CG leaders [217] and fast positive breakdown [218]. However, VHF radiation that extends only to 20 MHz may be consistent with the lack of detectable radiation from in-cloud positive leaders [219].

Figure 5.4 shows streamer properties (velocity v , radius R and maximum field strength at the streamer head E_{max}), the current I and current moment M , and a comparison between equation (5.11) and equation (5.4). Since this case is essentially axisymmetric, there is almost no difference in the resulting z component of \mathbf{E}_{rad} . The radius is here defined as $R = 0.6 \times \text{FWHM}$, where FWHM is the full width at half maximum of the time-integrated light emission. The current $I(z, t)$ is computed by integrating the electron conduction current over the x and y directions, and the current moment $M(t)$ is computed by integrating $I(z, t)$ over the z direction. Both I and M increase smoothly over time. An estimate for the maximal current I_{max} is also shown, given by

$$I_{\text{max}} = Q_{\text{head}}v/R = 2\pi v R \varepsilon_0 E_{\text{max}}, \quad (5.12)$$

where $Q_{\text{head}} = 2\pi R^2 \varepsilon_0 E_{\text{max}}$ is an approximation for the head charge [31].

The temporal variation in $M(t)$ determines the emission spectrum, and in previous work, this variation has often been characterized as exponential growth [208]. Below, we present an estimate for $M(t)$ in terms of streamer properties. Since M is a spatial integral over I , M can be approximated as $M \approx c_1 L I_{\text{max}}$, where c_1 is a constant less than one, L is the length of the channel and I_{max} is given by equation (5.12). Furthermore, on relatively short time scales we can assume that $L \approx c_2 R$ where c_2 is a constant greater than one, which states that the radius expands approximately linearly with length. If the two constants are combined into $c_3 = c_1 c_2$, the result is

$$M \approx c_3 R I_{\text{max}} = (2\pi c_3 \varepsilon_0) v R^2 E_{\text{max}}, \quad (5.13)$$

and in figure 5.4 a curve labeled M_{fit} is shown for which $c_3 = 13$. Finally, for comparison with the work of [208], we have fitted the velocity for $t > 40 \text{ ns}$ with an exponential function of the form $a \cdot e^{t/\tau}$, which resulted in $\tau \approx 100 \text{ ns}$.

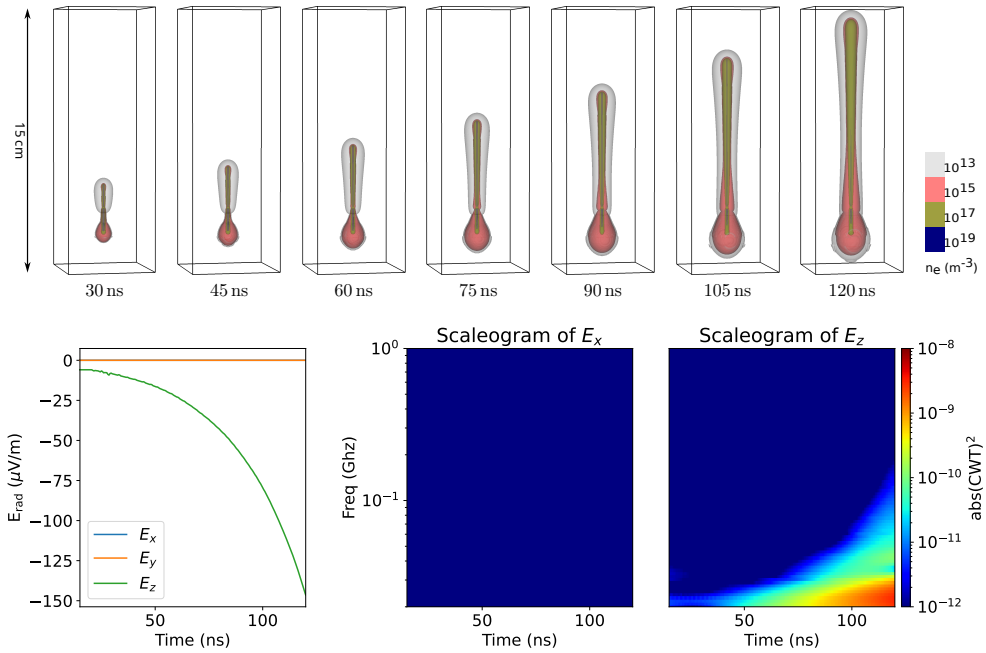


Figure 5.3: Top: contour plots showing the evolution of a single positive streamer with Helmholtz photoionization, propagating in the $+z$ direction in a background electric field of 6 kV/cm . Bottom: radiated electric field \mathbf{E}_{rad} at 1 km distance in the $+y$ direction and corresponding scaleograms. The delay due to the travel time of radiation has been subtracted, so that all times are synchronized. Note that \mathbf{E}_{rad} scales with the magnitude of the observer location.

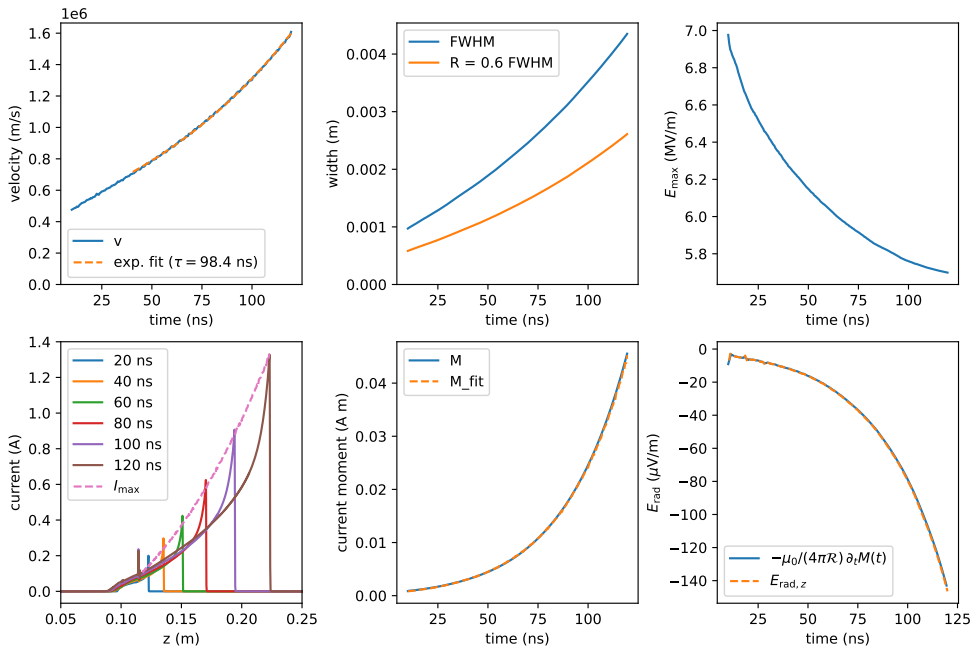


Figure 5.4: Properties of the single streamer with Helmholtz photoionization. Shown on the top row are the velocity, full width half maximum (FWHM) of the optical emission, an estimate for the radius and the maximum electric field at the streamer head. The bottom row shows the current $I(z, t)$ along the z axis, the current moment M , and the radiated electric field according to equations (5.4) and (5.11). The results of equations (5.12) and (5.13) are also shown.

Stochastic propagation with Monte Carlo photoionization

We now repeat the single streamer simulation described above using a Monte Carlo photoionization approach, i.e., the photons are modeled as discrete and stochastic. Figure 5.5 shows the time evolution of the electron density and \mathbf{E}_{rad} . The streamer is very similar to the one with Helmholtz photoionization, as it has about the same velocity, radius and electron density profile. The main difference is that its propagation is now somewhat stochastic, leading to small variations in the direction of propagation and in the streamer radius, and a tiny side branch is visible. The stochastic growth has several effects on the radiated electric field compared to the smoothly propagating case. First, there are significant fluctuations in $E_{\text{rad},z}$, which cause the streamer to emit radio emission at higher frequencies during its propagation as shown in the scaleograms. The period of these oscillations is on the order of 10 ns, which corresponds to frequencies on the order of $(10 \text{ ns})^{-1} = 100 \text{ MHz}$. Second, since the streamer is no longer axisymmetric, there is also emission visible in the x direction. (Note that $E_{\text{rad},y} \approx 0$ since the observer is in the $+y$ direction.) The VHF radiation in this simulation extends to approximately 100 MHz with a roughly constant amplitude, with a steep decay above that frequency. This spectrum is actually quite close to that reported for a strong positive CG [217]. Accordingly it suggests that the presence or lack of detectable VHF emissions from positive leaders (and thus streamers) could be partly driven by the number of streamers: if there are too few, they will not be detectable.

5.3.2 Double-headed streamer in a higher background field

In higher background electric fields streamers tend to propagate and accelerate faster. Streamers in higher background fields therefore typically radiate more energy, as was found in e.g. [208, 210, 211]. To compare how both the magnitude and the frequency of the radiation change with the background field, we have performed a simulation using the same conditions as in section 5.3.1 but with a background electric field of 10 kV/cm instead of 6 kV/cm. One other difference is that simulation output was stored more frequently, namely every 0.05 ns.

Figure 5.6 shows the evolution of the electron density and the radiated electric field. Due to the higher background field, a double-headed streamer forms. In about 36 ns, this double-headed streamer grows to a comparable length as the positive streamers in section 5.3.1 did in 120 ns. We used the Helmholtz photoionization method, so the streamer develops smoothly. However, relatively smooth propagation would also be expected with Monte Carlo photoionization, because discharges typically develop more smoothly in higher background electric fields (as also observed below in section 5.3.3). The radiated field is considerably stronger than for the case of section 5.3.1, with the z component being about an order of magnitude larger. Furthermore, the scaleograms show that

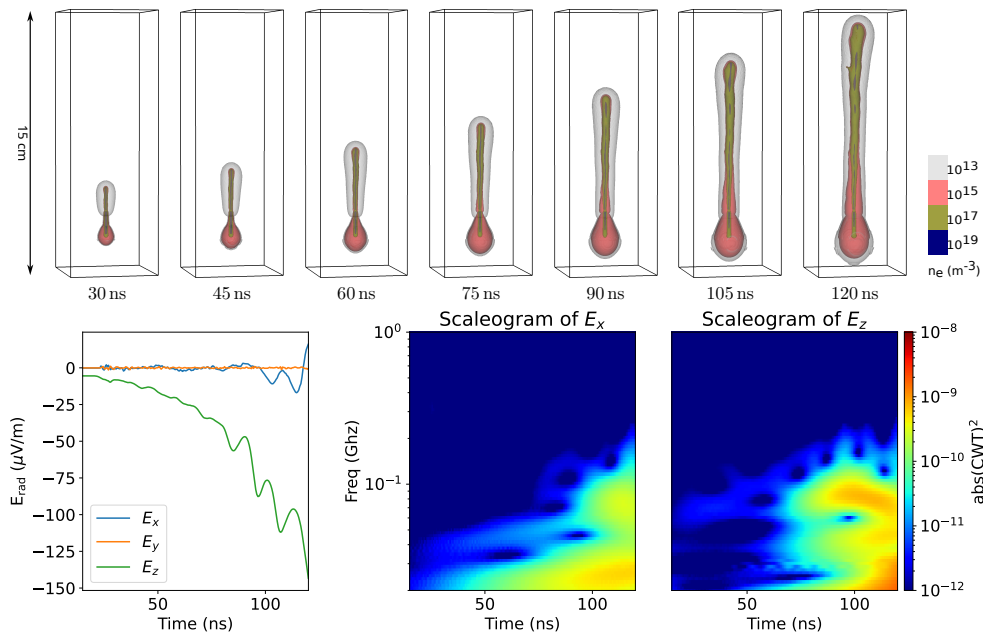


Figure 5.5: Results for a single streamer with stochastic photoionization. Note that the observer location is the same as in figure 5.3.

the emission occurs at higher frequencies, as expected. The higher field produces a faster streamer growth rate and, for this particular set of parameters, strong VHF emissions that are nearly constant in amplitude up to 100 MHz.

5.3.3 Branching streamer with stochastic photoionization

Most streamer discharges consist of many branched channels, together forming a larger “streamer tree”. When a streamer branches, the newly formed channels generally have different radii and velocities than the primary channel, which raises the question whether branching leads to a detectable change in the current through the channel, and therefore to detectable radio emission. Although it was mentioned in [211] that “branching does not lead to rapid changes in the current moment”, no results were presented to quantify the strength of the effect.

We simulate a branching streamer using the discrete Monte Carlo photoionization model that was also used in section 5.3.1. A slightly higher background electric field of 8 kV/cm is used, and in order to induce streamer branching early on, we place a weakly ionized patch slightly off-axis as shown in figure 5.7. This patch contains an equal amount of electrons and O_2^+ ions, and it has a degree of ionization of $5 \times 10^{14} \text{ m}^{-3}$. It is generated using the smoothstep profile as described in section 5.2.3 with $r_s = 0.7 \text{ mm}$.

Figure 5.7 shows that the streamer splits into two somewhat asymmetric

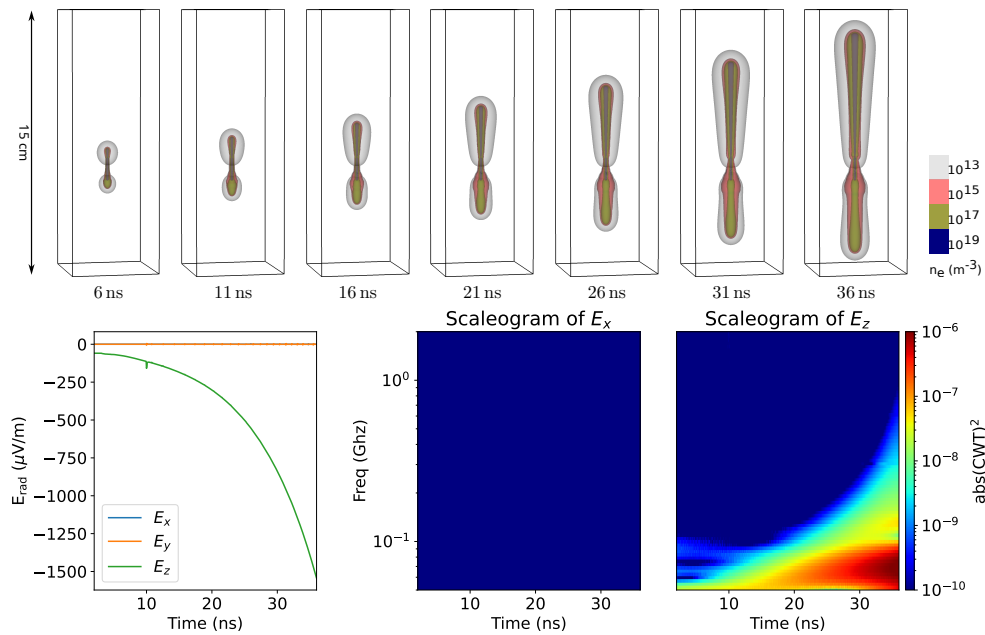


Figure 5.6: Results for a double-headed streamer developing in a background electric field of 10 kV/cm with Helmholtz photoionization. Top: electron density contours, bottom: radiated electric field. Note that the scales of frequency and “power” $\text{abs}(\text{CWT})^2$ in the scaleograms differ from previous plots.

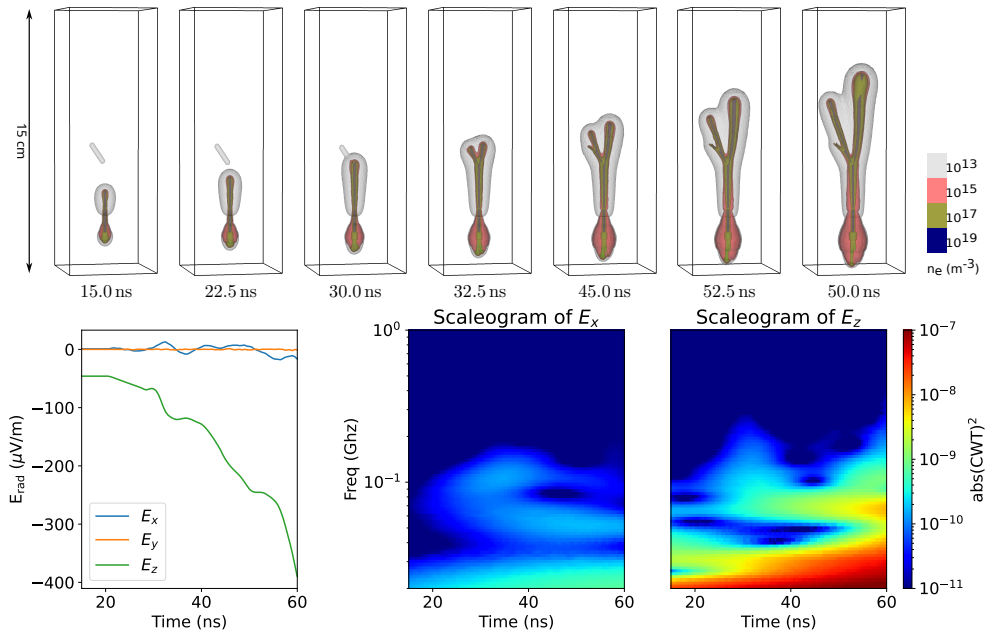


Figure 5.7: Results for a branching streamer developing in a background electric field of 8 kV/cm with Monte Carlo photoionization. A small preionized patch is included to trigger the branching, see text. Top: electron density contours, bottom: radiated electric field.

branches when it encounters the ionized patch around $t \approx 30\text{ ns}$. Although some fluctuations in $E_{\text{rad},z}$ are visible around this time, these fluctuations are weaker (relatively speaking) than the fluctuations observed without branching in section 5.3.1. During the later propagation, $E_{\text{rad},z}$ also develops more smoothly than in section 5.3.1. This is caused by the higher background electric field, which generally leads to smoother discharge propagation [158]. The branches have velocity components in the $+x$ and $-x$ direction, but the radio emission in the x direction is rather weak.

Overall, it seems that streamer branching does not lead to significant variation in the current and thus also not to a significantly different radio emission than the non-branching Monte Carlo streamer shown previously. This is consistent with the earlier statement in [211]. We have also confirmed this finding experimentally, as described in 5.5.1.

5.3.4 Interaction with ionized patches

In a large streamer tree, streamer heads can connect to the tails of other streamer channels that have the same polarity. This phenomenon has been observed in lab experiments, in sprite discharges and in simulations, see e.g. [44, 227]. We expect

that such interactions can lead to a significant change in the current through the channels, and therefore to radio emission. To test this hypothesis, we simulate the interaction of a single positive streamer with a neutral preionized channel having a much lower degree of ionization, namely $n_0 = 10^{15} \text{ m}^{-3}$ or $n_0 = 10^{16} \text{ m}^{-3}$. Such preionization could correspond to an older streamer, in which most electrons have been lost due to attachment and recombination.

The preionization is modeled as a cylindrical seed of length $\approx 5 \text{ cm}$, using the smoothstep profile described in section 5.2.3 with $r_s = 5 \text{ mm}$. The seed is placed at an angle of 45° with the x-axis (see figure 5.8). All other conditions are the same as in section 5.3.1, and we now use Helmholtz photo-ionization.

Simulation results are shown in figures 5.8 and 5.9. In both cases, the positive streamer reaches the preionized channel at approximately $t = 90 \text{ ns}$. For $n_0 = 10^{15} \text{ m}^{-3}$, the streamer temporarily slows down as it hits the preionization, leading to a reduction in $E_{\text{rad},z}$, but it later continues its vertical propagation. The streamer first slightly deviates towards the patch in the $-x$ direction, and the initial phase of a small side branch is visible in the $+x$ direction. This development causes a modest signal to be visible in $E_{\text{rad},x}$.

With $n_0 = 10^{16} \text{ m}^{-3}$ the preionization has a much stronger effect. The main streamer is now “guided” to propagate inside the preionization [85]. This leads to an abrupt change in the z component of the current, resulting in a sharp peak in $E_{\text{rad},z}$ and a sign inversion. Since the streamer propagates at a roughly 45° angle with respect to the z and x axis, $E_{\text{rad},z}$ and $E_{\text{rad},x}$ are of comparable magnitude during the guided propagation. The rapid variation in streamer properties and direction generates high-frequency radio emission. In the scaleograms, signals up to $200 - 300 \text{ MHz}$ are visible.

5.3.5 Streamer collision

Encounters or “collisions” between opposite polarity streamers have frequently been studied in the literature, see e.g. [210, 212, 213]. We present one such case here, so that the magnitude of the radiated field can be compared with the other cases that we have studied. As an initial condition, we use two initial seeds as described in section 5.2.3 and table 5.2. We apply a higher background electric field of 10 kV/cm so that two double headed streamers form. We also store simulation output more frequently, namely every 0.05 ns , so that we can resolve the collision dynamics. Figure 5.10 shows how a positive and negative streamer connect around $t = 14 \text{ ns}$. In agreement with previous work, a sharp peak is visible in the z component of the radiated electric field at the moment of collision. At this time, the emission spectrum extends to multiple GHz, since the collision takes place on sub-nanosecond time scales. The peak in E_{rad} has a significantly larger amplitude than it did for the other cases considered in this chapter, but the emission lasts for a much shorter time.

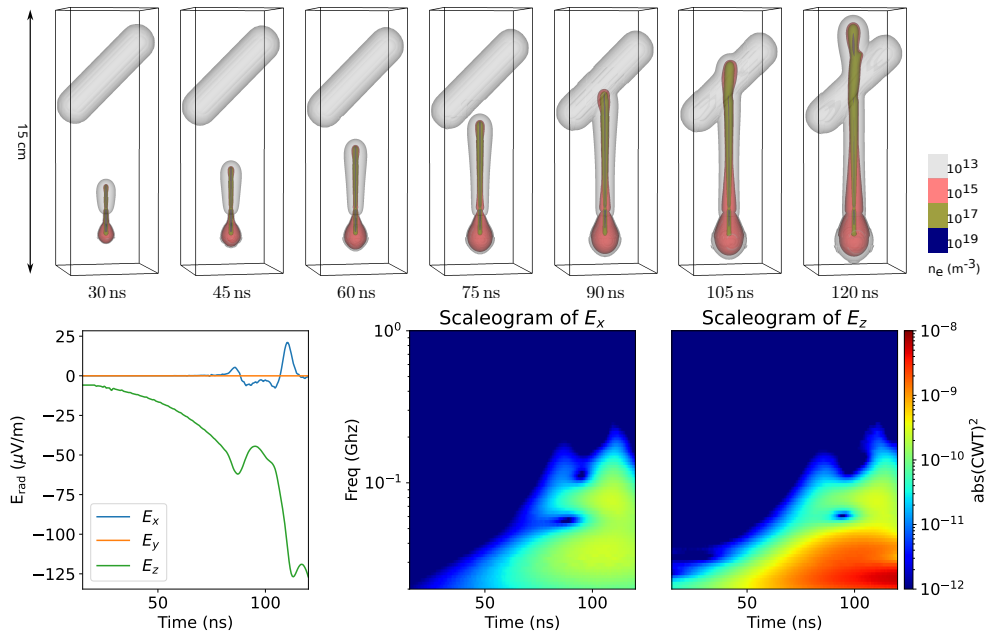


Figure 5.8: Results for a streamer interacting with a preionized channel in which the electron density is $n_0 = 10^{15} \text{ m}^{-3}$, in a background electric field of 6 kV/cm . Top: electron density contours, bottom: radiated electric field.

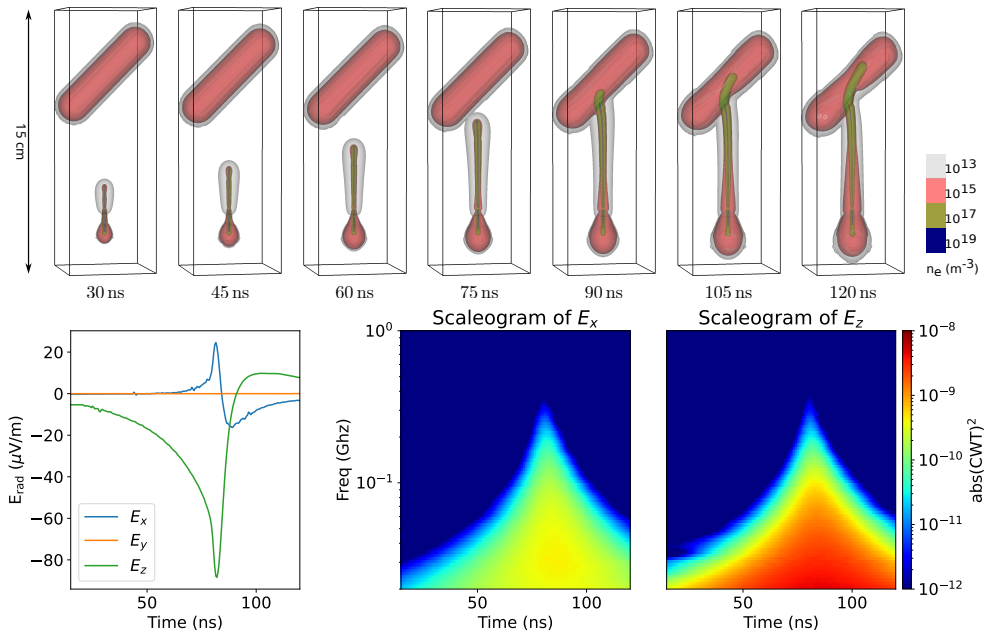


Figure 5.9: Results analogous to figure 5.8, but with a higher electron density in the channel of $n_0 = 10^{16} \text{ m}^{-3}$. The streamer is now strongly deviated by the channel.

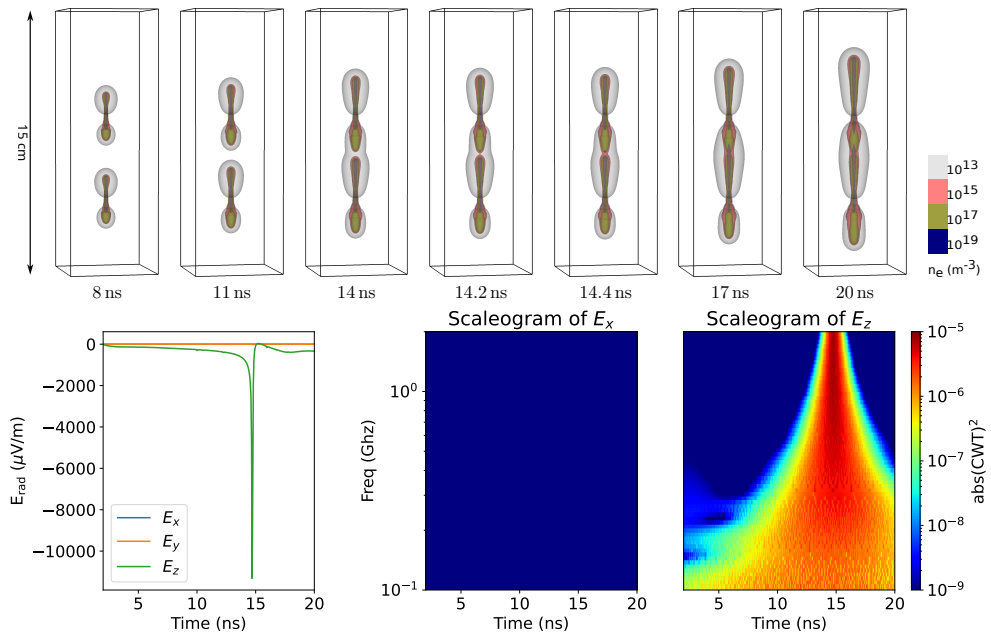


Figure 5.10: Results for an encounter between a positive streamer propagating upwards and a negative streamer propagating downwards, in a background electric field of 10 kV/cm. Note that two double-headed streamers form. Top: electron density contours, bottom: radiated electric field.

Table 5.3: Total radiated energy per unit area for each case, at a distance of 1 km in the $+y$ direction. The total energy deposited in the discharge and the simulation end time are also listed.

Description	E_{bg}	$Q_{\text{rad}} (\text{J}/\text{m}^2)$	$\varepsilon_{\text{tot}} (\text{J})$	$t_{\text{end}} (\text{ns})$
Single streamer - Helmholtz	6 kV/cm	9.3×10^{-19}	6.3×10^{-4}	120
Single streamer - Monte Carlo	6 kV/cm	8.4×10^{-19}	6.3×10^{-4}	120
Preionized channel 10^{15} m^{-3}	6 kV/cm	7.5×10^{-19}	6.1×10^{-4}	120
Preionized channel 10^{16} m^{-3}	6 kV/cm	2.2×10^{-19}	5.2×10^{-4}	120
Guided streamer branching	8 kV/cm	3.5×10^{-18}	6.8×10^{-4}	60
Single streamer - Helmholtz	10 kV/cm	3.1×10^{-17}	1.1×10^{-3}	36
Streamer collision	10 kV/cm	3.4×10^{-17}	4.8×10^{-4}	20

5.3.6 Radiated energy

To compare how much energy is radiated in these different cases, we have computed the time integral of the Poynting flux of radiated energy

$$Q_{\text{rad}}(\mathbf{r}_{\text{obs}}) = \int_{t_0}^{t_1} \frac{\mathbf{E} \times \mathbf{B}}{\mu_0} \cdot \hat{\mathbf{r}}_{\text{obs}} dt = \int_{t_0}^{t_1} c \varepsilon_0 |\mathbf{E}(\mathbf{r}_{\text{obs}})|^2 dt \quad (5.14)$$

at the observation location $\mathbf{r}_{\text{obs}} = (0, 1 \text{ km}, 0)$, where we have used the identity (5.19) from 5.6 that is valid for planar, but not necessarily monochromatic waves. Q_{rad} has units of energy per unit area and t_0 and t_1 correspond to the time range shown in the respective plots of \mathbf{E}_{rad} . In table 5.3, Q_{rad} is given for each case. The amount of radiated energy seems to primarily depend on the background electric field. Considerably more energy is radiated for the double-headed streamer case and the streamer collision case, which both took place in a background electric field of 10 kV/cm. For comparison, we have also listed the total energy dissipated in each discharge in table 5.3, which was computed by integrating the Joule heating term over space and time:

$$\varepsilon_{\text{tot}} = \int_{t_0}^{t_1} \left[\int_V \mathbf{j} \cdot \mathbf{E} d^3\mathbf{r} \right] dt. \quad (5.15)$$

The variation in the deposited energy is rather small, which can be explained by the fact that the discharges grow to comparable sizes in all test cases. From these results, we can furthermore conclude that the fraction of energy that is radiated is significantly larger in a higher background electric field, with the streamer collision being the most ‘efficient’ process.

5.4 Conclusions

In this chapter we have studied radio emissions from vertically moving positive streamers in air at 500 mbar using 3D simulations. The electric field radiated by

the charge and current densities was computed at 1 km distance in the horizontal direction by numerically evaluating Jefimenko's equations. To illustrate the temporal evolution of the emission spectrum, we computed so-called scaleograms using wavelet analysis methods.

We first considered single positive streamers and compared results with two photoionization methods: the Helmholtz approximation and a Monte Carlo method using discrete photons. With the Helmholtz approximation our simulated streamers grow and accelerate smoothly. The resulting power spectrum of the radio emissions exhibits a characteristic decay, with the emission shifted to higher frequencies in higher background fields. With the Monte Carlo approach the overall streamer evolution was highly similar, but small stochastic fluctuations during the streamers propagation led to substantially more radio emission at frequencies of 100 MHz and above.

The Monte Carlo approach is the most realistic approximation of photoionization, as it reproduces the stochastic fluctuations in the electron density ahead of a streamer that should physically be present. How strongly these fluctuations affect streamer propagation in a thunderstorm will to a large degree depend on the background electric field. In a higher background electric field, streamer channels generally produce more photoionization per unit length, so that stochastic fluctuations become less important, as shown by [228]. Furthermore, at higher altitudes, the amount of photoionization will increase (relatively) due to a reduction in the collisional quenching of photon-emitting molecules.

For the smoothly developing case with Helmholtz photoionization, we presented an approximation for the maximal current along the channel and a fit formula for the current moment as a function of streamer properties. A double-headed streamer in a higher background electric field was also simulated. As expected, the faster growth rate of this discharge led to an increase in both the magnitude and the frequency of radio emissions.

One of the main reasons for performing this study was to understand how much radio emission would be generated by streamer branching, since this process happens very frequently in most streamer discharges. We simulated branching with the Monte Carlo photoionization method, and we included a small amount of preionization along to trigger the branching process. We did not observe a strong signal during or after the branching process, which was also confirmed by lab experiments. This indicates that the current inside a streamer discharges evolves approximately continuously during branching.

Another process that could frequently occur in lightning discharges is the interaction of streamers with some residual ionization, for example from a previous streamer channel. We simulated such interactions with preionized channels containing an ionization density of 10^{15} m^{-3} and 10^{16} m^{-3} . When encountering such pre-ionization, the streamer current and direction can rapidly change, which leads to increased emission at frequencies above 100 MHz.

Finally, we also simulated the encounter between a positive and a negative

streamer. In agreement with previous findings, the channels “connect” to each other on a sub-ns time scale, resulting in a sharp peak in the radio emission, with emission at frequencies above a GHz. This process emitted the highest amount of radiated energy, but only slightly more than the double-headed streamer in the same background electric field. We therefore conclude that the amount of radiated energy primarily depends on the background electric field and to a lesser extent on the type of streamer process taking place. The streamer collision process was the most efficient in terms of converting “discharge energy” (the integral over $\mathbf{J} \cdot \mathbf{E}$) into radiated energy.

5.5 Appendix

5.5.1 Experimental results on possible radio emission from streamer branching

Experimental methods

To investigate whether the current shows an apparent peak during streamer branching, we have performed current measurements synchronized with stroboscopic images of streamer discharges in air within a protrusion-to-plane gap. The experiment setup we used is similar to the one that is described in [229], but with some slight differences. The high voltage was pulsed at a frequency of 20 Hz, while the CCD operated at 2 frames per second (fps), enabling us to capture one in every ten discharges. Figure 5.11(a) illustrates the typical waveforms of the current and the 50 MHz camera gating signal that is used for stroboscopic imaging. The current was measured by a 50 Ω shunt resistor which connects the bottom plate and the ground. Due to the inherent noise in the current measured by the shunt resistor and the presence of damped oscillations from capacitive current in the subsequent waveform, we subtracted the current without discharge (I_0) from the measured discharge current (I_1). Additionally, we applied a Savitzky-Golay filter to smooth the current waveforms.

In order to establish the relation between image timing and current trace timing, the intensifier gating was set-up to skip one pulse in the 50 MHz pulse train. As a result, the captured image will display a missing dot, corresponding to the skipped pulse, which is shown in figure 5.11(b). In this way, the timing of every dot on the captured image is known with an accuracy of about 8 ns, which is the open time of the camera gating.

Current change during streamer branching

In order to visualize the current change during the streamer branching, we shift the current timescale such that the branching deduced from the images occurs at $t = 0$. Ten examples of current waveforms during branching and the corresponding discharge images are shown in figure 5.12. For cases that branch more than

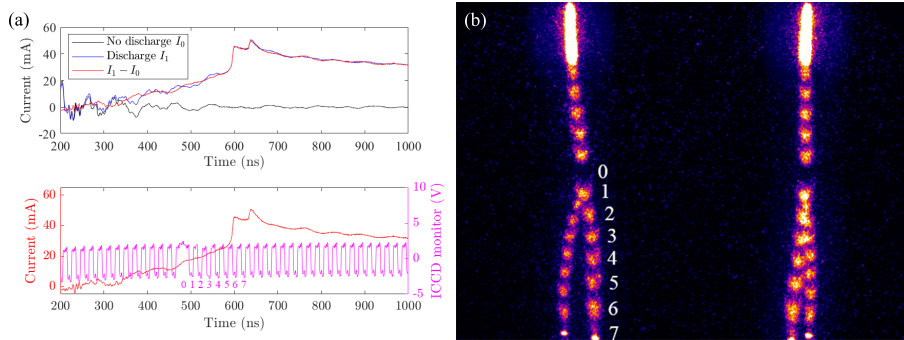


Figure 5.11: (a) Current waveform and camera gating; (b) Corresponding image.

two times, the corresponding current waveforms are both shown, *e.g.*, waveforms 4-5 and 9-10. From the figure, we can conclude that no significant change of current can be detected around the streamer branching moment.

Furthermore, taking curve No.1 from figure 5.12 as an example, upon closer examination of the current waveform shown in figure 5.13, it is found that there are still some ripples on the order of 0.2 mA present from the inherent noise associated with the setup and which cannot be systematically correlated to branching events. Since the real branching may occur within adjacent camera gating, and the current change within this period is around 4 mA, this means that the minimal detectable current step is below 5% of the average current. From these results, we conclude that the current change during streamer branching is too small to detect with our current equipment. We should note that the streamers give a very clear current jump and peak effect at the moment they have crossed the gap, which is clearly visible in figure 5.11.

Radio emission during streamer branching

Besides current measurements, we have performed radio emission measurements of streamer discharges by using a homemade dipole antenna with a total length of 200 mm and two commercial antennas (Pulse Electronics NMO150/450/758, a 450 mm long tri-band monopole antenna and Larid Connectivity EFF6060A3S-10MHF1, a $130 \times 3 \times 0.3$ mm adhesive antenna). During the experiment, each antenna was mounted on the quartz window (with a horizontal distance of about 320 mm to the discharge region) of the vessel horizontally and vertically, respectively, in order to detect the variation of electromagnetic field caused by streamer branching from two orthogonal directions. The streamer discharge and the background electric field in the vessel are primarily in the vertical direction. Again, all measurements were synchronized with stroboscopic images to show the timing of the branching events.

As little difference was found between the results from the six different an-

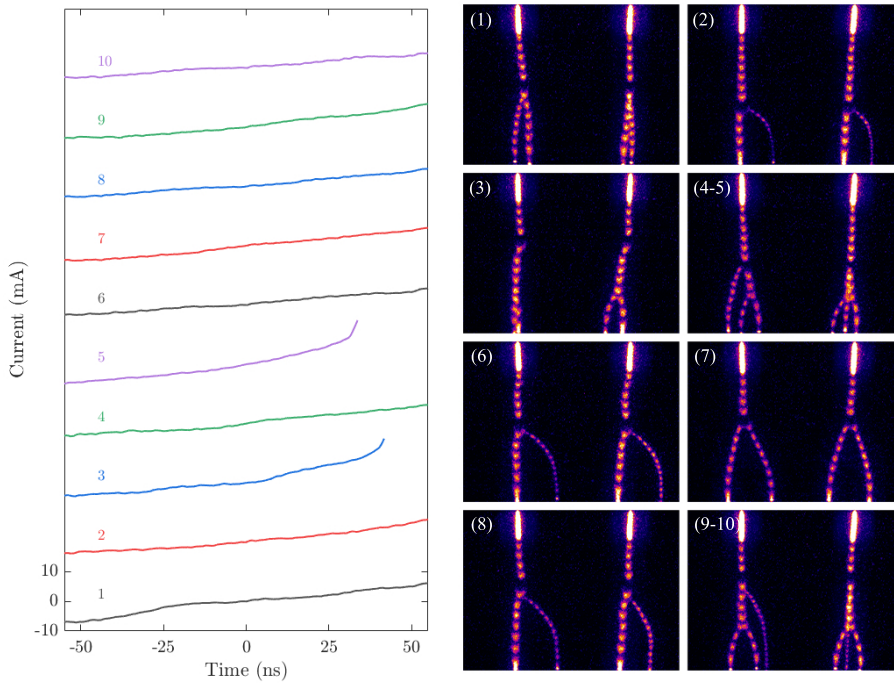


Figure 5.12: (a) Current waveforms during branching events. The vertical position of each current curve is offset to avoid overlapping and $t = 0$ corresponds with the estimated time of branching; (b) Corresponding discharge image.

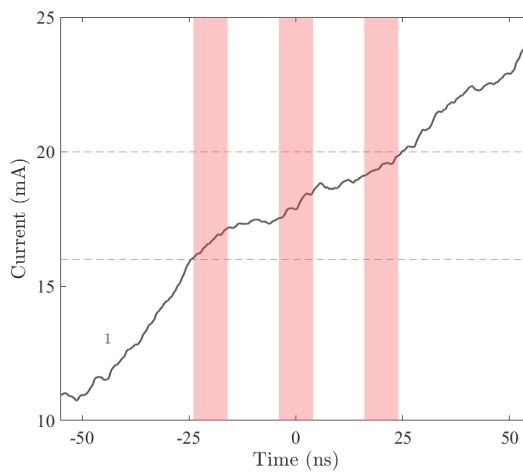


Figure 5.13: Zoom in view of current waveform No. 1 taken from figure 5.12, with the camera gating indicated by shadow in red

tenna configurations, here we only show the results of the horizontally mounted homemade dipole antenna. The response of the antenna was tested by applying standard sinusoidal and pulsed waveforms (with frequency up to 60 MHz) from a function generator (Keysight 33600A) to the same gas gap. The final signals are subtracted by the signal without discharge to eliminate the strong interference produced by the high voltage pulses. Figure 5.14 shows the current waveforms, the signals of the antenna, and the corresponding discharge images for three different representative cases, namely, a streamer with a single channel, a streamer with two equal branches, and a streamer with two unequal branches. For two unequal branches, their velocities, but also their times of arrival are quite distinct, as can be seen by the two peaks at 800 and 880 ns in figure 5.14(c). It should be noted that the real branching event may occur within adjacent camera gating cycles, which can be seen in the discharge image of figure 5.14(b) and (c). Nevertheless, no significant difference can be seen between the signals of the dipole antenna for the three different cases. Furthermore, no signal is found when streamers connect the gap, even the current change is much larger than that of branching, implying that the emitted signal is either too small or not in the sensitive range of the antenna. Although there are some slight features visible in the signals for other configurations, they cannot be correlated with branching events.

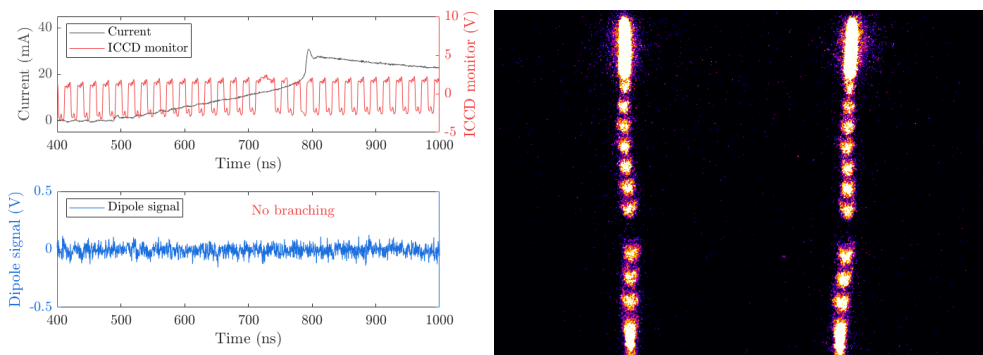
Conclusions

Besides the results shown above, we have also stacked larger numbers of waveforms like shown in figure 5.12(a) for both current measurements and antenna output, but did not find any significant signal.

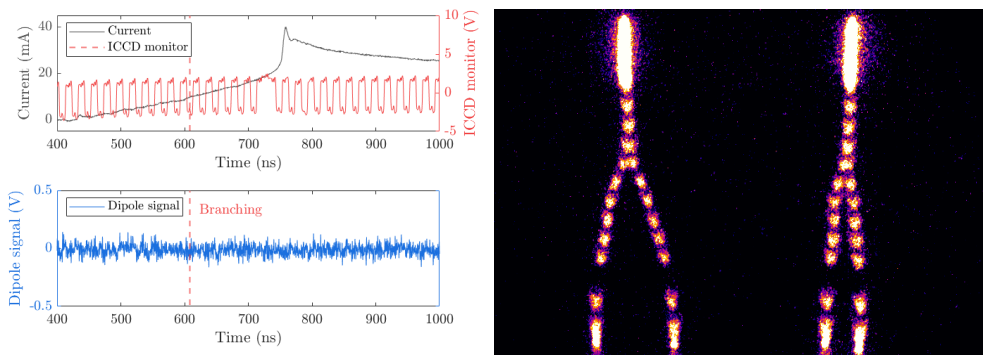
Therefore, we can conclude from our experiments that the current signal and radio emissions streamers do not exhibit any features that we can correlate with streamer branching within our experimental limitations.

5.5.2 Numerically solving Jefimenko's equations on an AMR grid

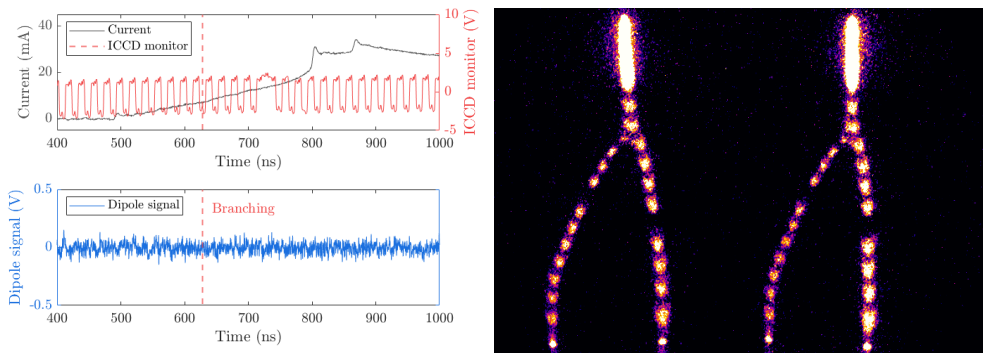
Below we explain how we numerically evaluate the integral of equation (5.4) to obtain the radiated electric field. In our results, we have omitted the first (static) term, which does not correspond to the radiated field and which can be made arbitrarily small by picking a farther away observation location. There are several factor that make the evaluation of the other two terms non-trivial. First, strict charge conservation is required, otherwise there can be a large artificial signal from the $\partial_t \rho$ term. We guarantee this up to the level of machine precision by employing conservative interpolation and coarsening methods in our AMR simulations. Furthermore, we ensure the discharges stay away from the domain boundaries, so that there is no charge flowing in or out of the domain.



(a) Non-branching streamer.



(b) Branching streamer with equal branches



(c) Branching streamer with unequal branches

Figure 5.14: Measurements using a horizontally mounted dipole antenna and the corresponding discharge images for three different discharge morphologies. The red dashed lines indicate the approximate timing of the branching event.

Another challenge is that time derivatives of ρ and \mathbf{J} are required. To obtain these at time t_1 , we use central differencing to obtain

$$\partial_t \rho(\mathbf{r}, t_1) \approx \frac{\rho(\mathbf{r}, t_2) - \rho(\mathbf{r}, t_0)}{2\Delta t}, \quad (5.16)$$

where Δt is the (constant) time step between simulation outputs. This is not enough yet, because the integral requires this derivative at different retarded times, with $t_r = t - \mathcal{R}/c$ having a different value for every grid cell. We therefore compute a second derivative as

$$\partial_t^2 \rho(\mathbf{r}, t_1) \approx \frac{\rho(\mathbf{r}, t_2) - 2\rho(\mathbf{r}, t_1) + \rho(\mathbf{r}, t_0)}{\Delta t^2}. \quad (5.17)$$

We can then account for the variable time retardation by approximating

$$\partial_t \rho(\mathbf{r}, t_1 + h) \approx \partial_t \rho(\mathbf{r}, t_1 + h) + h \partial_t^2 \rho(\mathbf{r}, t_1). \quad (5.18)$$

The same approach is used for each component of the current density \mathbf{J} .

Since the AMR grid changes in time, we have to map all the quantities appearing in equations (5.16)–(5.18) to the same grid. At first, we used a uniform grid for this purpose, which was limited to 128^3 or 256^3 due to memory limitations. However, this did not lead to satisfactory results, because the motion of the streamer was not captured smoothly on such a grid, leading to artificial signals when streamer’s head charge would move from one cell to the next. We therefore decided to instead map $\rho(\mathbf{r}, t_1)$ and $\rho(\mathbf{r}, t_2)$ (and similar for the components of \mathbf{J}) to the AMR grid corresponding to $\rho(\mathbf{r}, t_0)$ in these equations. This was again done in a conservative way. Finally, for computational efficiency, we decided to save the simulation output not up to the finest AMR level used in the discharge simulations, but up to a resolution of about 0.15 mm.

5.6 The far field approximation for electromagnetic waves

Equation (5.9) quotes the approximate relation $E_{\text{rad}} = c B_{\text{rad}}$ between the size of magnetic and electric field in an electromagnetic wave far from the source. Here we discuss the range of validity of this approximation.

The textbook by Griffiths [221] (as well as many other sources) contains the derivation of the relation

$$\mathbf{B} = \frac{\hat{\mathbf{k}} \times \mathbf{E}}{c} \quad (5.19)$$

for a monochromatic plane wave $\mathbf{E}(\mathbf{r}, t) = \mathbf{E} e^{i(\mathbf{k} \cdot \mathbf{r} - \omega t)}$ in vacuum. Here \mathbf{k} is the wave vector, and $\hat{\mathbf{k}} = \mathbf{k}/|\mathbf{k}|$ is the unit vector parallel to the wave vector. \mathbf{E} is

orthogonal to \mathbf{k} by construction, so $\mathbf{k} \cdot \mathbf{E} = 0$ and $|\hat{\mathbf{k}} \times \mathbf{E}| = |\mathbf{E}|$, which means that

$$|\mathbf{E}| = c|\mathbf{B}| \quad (5.20)$$

in this particular case. But is this relation also valid more generally, in particular for an arbitrary superposition of Fourier modes?

An answer can be found by superposing two Fourier modes with different wave vectors \mathbf{k}_1 and \mathbf{k}_2 , so that $\mathbf{E} = \mathbf{E}_1 + \mathbf{E}_2$ and $\mathbf{B} = (\hat{\mathbf{k}}_1 \times \mathbf{E}_1 + \hat{\mathbf{k}}_2 \times \mathbf{E}_2)/c$. It then follows that

$$|\mathbf{E}|^2 - c^2|\mathbf{B}|^2 = 2\left(\mathbf{E}_1 \cdot \mathbf{E}_2 - (\hat{\mathbf{k}}_1 \times \mathbf{E}_1) \cdot (\hat{\mathbf{k}}_2 \times \mathbf{E}_2)\right), \quad (5.21)$$

which is zero when $\hat{\mathbf{k}}_1 = \hat{\mathbf{k}}_2$, but not in general. We can conclude that equation (5.19) is applicable to a superposition of planar Fourier modes propagating in the same direction $\hat{\mathbf{k}}$, but not to modes propagating at arbitrary directions to each other. The equation can be applied in the far field approximation, i.e., if the distance to the radiating object is much larger than the object size and the wave length.

Additionally, it can be tested whether magnetic and electric field are still orthogonal in the superposition of the two modes. Using the relation (5.19) for the magnetic fields, the orthogonality relations of the fields in the Fourier modes and standard vector algebra, one finds in a few steps of calculation that

$$\mathbf{E} \cdot c\mathbf{B} = (\hat{\mathbf{k}}_1 - \hat{\mathbf{k}}_2) \cdot (\mathbf{E}_1 \times \mathbf{E}_2). \quad (5.22)$$

This means that electric and magnetic field in the superposition wave are orthogonal to each other, if the wave vectors of the two Fourier modes point in the same direction, $\hat{\mathbf{k}}_1 = \hat{\mathbf{k}}_2$, but not in general. This criterion is sufficient for the orthogonality of \mathbf{E} and \mathbf{B} , and it is the same as for the validity of equations (5.19) and (5.20): the electromagnetic wave is planar, but not necessarily monochromatic. In other words: the wave can consist of an arbitrary superposition of Fourier modes, if all wave vectors are pointing in the same direction.

Chapter 6

Conclusions and outlook

6.1 Summary and conclusions

In this thesis, we studied three different topics pertaining to the field of streamer discharges in air and air-like mixtures using a computations. First, we looked at the behaviour of positive streamers under repetitive pulsed conditions in Chapters 2 and 4. We looked at how the second-pulse streamer was affected by the first-pulse streamer for varying interpulse times (Chapter 2). Then we examined how the Joule heating affected streamer properties under repetitive pulsing (Chapter 4). Second, we studied variations in streamer properties in air-water mixtures when using different H₂O collision cross-sections, chemical reaction sets, and photoionization coefficients from different authors (Chapter 3). Finally, we estimated the electromagnetic radiation in the radio frequency range from different simulated streamer scenarios commonly occurring in lightning discharges (Chapter 5). All our simulations were performed in air and air-like mixtures using a drift-diffusion-reaction type fluid model under the local field approximation. Below, we now summarize the most important conclusions from the individual Chapters:

- **Chapter 2:** Increasing the interpulse times in our double-pulse simulations resulted in the second-pulse streamer transitioning between three regimes: continuation, inhibition, and repetition. In the streamer continuation regime, a new streamer emerges from the tip of the previous one. In the inhibited regime, the previous channel is partially re-ionized, but there is considerably less field enhancement and almost no light emission. Finally, for the longest interpulse times, a new streamer forms that is similar to the first one. The criterion for streamer continuation depends on the channel conductivity at the start of the second pulse, background field and the pulse duration. Furthermore, for interpulse times above 100 ns several electron detachment reactions significantly slow down the electron density decay in the streamer channel.

- **Chapter 4:** The successive energy deposition of repetitive streamer discharges results in an increase in the neutral gas temperature which naturally leads to a decrease in the gas number density inside the streamer channel. This causes the streamer length to eventually increase. The energy deposited per pulse depends on the pulse repetition frequency, the background electric field and on the streamer length.
- **Chapter 3:** The choice of cross-sections, reaction sets and photoionization model affect the results of positive streamer simulations in dry and humid air. H_2O cross section sets from different authors give different electron transport coefficients in humid air. Photoionization is smaller in humid air than in dry air due to photoabsorption by H_2O molecules. Irrespective of the model used, photoionization reduced by humidity leads to thinner and faster simulated streamers. At STP in humid air, for relatively short timescales, streamer properties are affected by electron-attachment and ion recombination reactions taking place inside the streamer channel. Chemistry sets that differ in these reactions, especially electron-ion recombination reactions with positive-ion water clusters give rise to different streamer properties.
- **Chapter 5:** Stochastic fluctuations associated with photoionization in the streamer evolution strongly increase radio emissions above 100 MHz. In higher background fields, a streamer grows faster which results in radio emission of higher magnitude and frequency. Streamer branching does not lead to strong fluctuations in the streamer current, so this phenomenon produces only a weak radio signal. When encountering preionized regions, the streamer current magnitude and direction change which causes significant radio emissions. Collisions between opposite-polarity streamers occur on a sub-nanosecond time scale, which leads to a distinct peak in the radio emission across frequencies exceeding one gigahertz. Finally, the maximal current in a streamer channel can be approximated by a simple expression that depends on the streamer velocity, radius and its maximal electric field.

6.2 Outlook

- **Improved boundary conditions:** In the repetitive-pulse simulations performed in Chapters 2 and 4, the electrode polarity reversed whenever the voltage fell to zero. Whenever this occurs, a cathode sheath with a high local field forms around the electrode [97, 98], which was not modeled in this work. Accurately resolving such a sheath requires a really fine grid and a small time step which makes such simulations computationally not feasible. Developing efficient computational approaches to resolve this sheath is needed, for example, approximating the electron dynamics inside

the sheath.

- **3D simulations of repetitive streamers:** Branching and asymmetric streamers commonly occur under repetitive pulsed conditions. However, due to the ‘long’ time between pulses, it is currently computationally too costly to simulate such phenomena with a full 3D model. Therefore computational approaches to accelerate 3D simulations are required.
- **Reliable chemistry data:** As demonstrated in Chapter 3 and in [87], simulated streamer properties vary depending on the input data used. In order to be able to simulate streamer discharges in a broad range of operating conditions we need (i) accurate and complete collision cross-sections, and (ii) reliable reaction sets for various gas compositions. Additionally, developing standardized tools to identify the most important chemical processes and to automatically simplify complex chemistries will be a vital next step.
- **Development of macroscopic/reduced models:** These models do not resolve the smallest spatial and temporal scales but instead provide a more macroscopic description of the evolution of a streamer channel. They can therefore be computationally much cheaper than conventional particle or fluid models. One such model is proposed in [230] for a positive streamer propagating in a constant background field.
 - **Modeling repetitive pulsed streamers:** We have motivated the importance of studying streamer discharges under repetitive pulsed conditions in sections 2.1 and 4.1. However, performing such simulations over long timescales is computationally expensive. Developing macroscopic models which incorporate detailed plasma chemistry, effects of Joule heating and previous discharges, etc., could be useful to understand the streamer-to-leader/spark transition.
 - **Calculating radio frequency emissions:** Streamers occurring in lightning discharges tend to be several meters long. Simulating such streamers in 3D is computationally not (yet) possible. Reduced models could be used to obtain the current density of such large discharges, which can then be used to compute the radiated electric field.

Bibliography

- [1] Vernon Cooray. *The lightning flash*. 34. IET, 2003.
- [2] Yuri P Raizer. *Gas Discharge Physics*. Springer Berlin Heidelberg, 1991.
- [3] Michael A Lieberman and Allan J Lichtenberg. “Principles of plasma discharges and materials processing”. In: *MRS Bulletin* 30.12 (1994).
- [4] The Slow Mo Guys. *Lightning Strike at 103,000 Fps*. <https://www.youtube.com/watch?v=qQKhIK4pvYo>. Accessed: January 4, 2024.
- [5] UC Berkeley. *Plasma pen*. <https://catalyst.berkeley.edu/2017/05/01/treating-disease-with-atmospheric-plasmas/>. Accessed: March 6, 2024. 2017.
- [6] Francisco J Gordillo-Vázquez and Francisco J Pérez-Invernón. “A review of the impact of transient luminous events on the atmospheric chemistry: Past, present, and future”. In: *Atmospheric Research* 252 (2021).
- [7] Loucas G Christophorou et al. “Sulfur hexafluoride and the electric power industry”. In: *IEEE Electrical Insulation Magazine* 13.5 (1997).
- [8] Valérie Masson-Delmotte et al. “Climate change 2021: the physical science basis”. In: *Contribution of working group I to the sixth assessment report of the intergovernmental panel on climate change 2* (2021).
- [9] Mohamed Rabie and Christian M Franck. “Assessment of eco-friendly gases for electrical insulation to replace the most potent industrial greenhouse gas SF₆”. In: *Environmental science & technology* 52.2 (2018).
- [10] Patrick C. Stoller et al. “CO₂ as an Arc Interruption Medium in Gas Circuit Breakers”. In: *IEEE Transactions on Plasma Science* 41.8 (Aug. 2013).
- [11] Housseem Eddine Nechmi et al. “Fluoronitriles/CO₂ gas mixture as promising substitute to SF₆ for insulation in high voltage applications”. In: *IEEE Transactions on Dielectrics and Electrical Insulation* 23.5 (2016).
- [12] Siddharth Kumar et al. “Electrical Breakdown Study in CO₂ and CO₂-O₂ Mixtures in AC, DC and Pulsed Electric Fields at 0.1–1 MPa Pressure”. In: *IEEE Transactions on Dielectrics and Electrical Insulation* 28.1 (2021).
- [13] Ravi Patel et al. “Low-temperature filamentary plasma for ignition-stabilized combustion”. In: *Combustion and Flame* 247 (2023).
- [14] Svetlana Starikovskaia et al. “Non-equilibrium plasma for ignition and combustion enhancement”. In: *The European Physical Journal D* 75.8 (2021).

- [15] Thijs Hazenberg et al. “Consistent thermodynamics for plasma-assisted combustion”. In: *Proceedings of the Combustion Institute* 39.4 (2023).
- [16] L Cheng et al. “Plasma assisted combustion of methane-air mixtures: Validation and reduction”. In: *Combustion and Flame* 240 (2022).
- [17] Lars Boeckmann et al. “Synergistic effect of cold gas plasma and experimental drug exposure exhibits skin cancer toxicity in vitro and in vivo”. In: *Journal of Advanced Research* (2023).
- [18] Mounir Laroussi. “Cold plasma in medicine and healthcare: The new frontier in low temperature plasma applications”. In: *Frontiers in Physics* 8 (2020).
- [19] Thomas von Woedtke et al. “Perspectives on cold atmospheric plasma (CAP) applications in medicine”. In: *Physics of Plasmas* 27.7 (2020).
- [20] Ruben Verloy et al. “Cold Atmospheric Plasma Treatment for Pancreatic Cancer—The Importance of Pancreatic Stellate Cells”. In: *Cancers* 12.10 (2020).
- [21] Pietro Ranieri et al. “Plasma agriculture: Review from the perspective of the plant and its ecosystem”. In: *Plasma Processes and Polymers* 18.1 (2021).
- [22] Corina Bradu et al. “Reactive nitrogen species in plasma-activated water: Generation, chemistry and application in agriculture”. In: *Journal of Physics D: Applied Physics* 53.22 (2020).
- [23] Milan Šimek and Tomáš Homola. “Plasma-assisted agriculture: History, presence, and prospects—A review”. In: *The European Physical Journal D* 75 (2021).
- [24] A Yu Starikovskiy and NL Aleksandrov. “Gasdynamic flow control by ultrafast local heating in a strongly nonequilibrium pulsed plasma”. In: *Plasma Physics Reports* 47 (2021).
- [25] Chris Rethmel et al. “Flow separation control using nanosecond pulse driven DBD plasma actuators.” In: *International Journal of Flow Control* 3.4 (2011).
- [26] Yifei Zhu et al. “Nanosecond-pulsed dielectric barrier discharge-based plasma-assisted anti-icing: modeling and mechanism analysis”. In: *Journal of Physics D: Applied Physics* 53.14 (2020).
- [27] Jinsheng Cai et al. “An experimental study of icing control using DBD plasma actuator”. In: *Experiments in Fluids* 58 (2017).
- [28] Igor Adamovich et al. “The 2022 Plasma Roadmap: low temperature plasma science and technology”. In: *Journal of Physics D: Applied Physics* 55.37 (2022).
- [29] Sander Nijdam. “Experimental investigations on the physics of streamers”. PhD thesis. Technische Universiteit Eindhoven, 2011.
- [30] H Raether. “The electron avalanche and its development”. In: *Applied Scientific Research, Section B* 5.1 (1956).
- [31] Sander Nijdam et al. “The physics of streamer discharge phenomena”. In: *Plasma Sources Sci. Technol.* 29.10 (2020). Publisher: IOP Publishing.
- [32] Stephen Hummel. *Photographs from McDonald Observatory by Stephen Hummel*. <https://www.theweathernetwork.com/en/news/weather/forecasts/spectacular-jellyfish-sprite-captured-what-causes-these-strange-events>. Accessed: February 4, 2024.

-
- [33] Siebe Dijcks. “Diagnostic Imaging of Streamers: Deducing key properties of positive streamers in air, nitrogen and carbon dioxide”. PhD thesis. Technische Universiteit Eindhoven, 2023.
- [34] Sergey Pancheshnyi. “Role of electronegative gas admixtures in streamer start, propagation and branching phenomena”. In: *Plasma Sources Science and Technology* 14.4 (2005).
- [35] M. B. Zheleznyak et al. “Photoionization of nitrogen and oxygen mixtures by radiation from a gas discharge”. In: *High Temperature Science* 20.3 (Nov. 1982).
- [36] DD Sentman et al. “Plasma chemistry of sprite streamers”. In: *Journal of Geophysical Research: Atmospheres* 113.D11 (2008).
- [37] Ute Ebert et al. “Review of recent results on streamer discharges and discussion of their relevance for sprites and lightning”. In: *Journal of Geophysical Research: Space Physics* 115.A7 (2010).
- [38] Ute Ebert and Davis D Sentman. “Streamers, sprites, leaders, lightning: from micro-to macroscales”. In: *Journal of Physics D: Applied Physics* 41.23 (2008).
- [39] Raymond A Minzner et al. *Defining constants, equations, and abbreviated tables of the 1975 US Standard Atmosphere*. Tech. rep. 1976.
- [40] Pavlo O Kochkin et al. “Experimental study of the spatio-temporal development of metre-scale negative discharge in air”. In: *Journal of Physics D: Applied Physics* 47.14 (2014).
- [41] Arturo Popoli et al. “A Boltzmann Electron Drift Diffusion Model for Atmospheric Pressure Non-Thermal Plasma Simulations”. In: *Plasma* 6.3 (2023).
- [42] M Stankov et al. “Influence of surface parameters on dielectric-barrier discharges in argon at subatmospheric pressure”. In: *Plasma Sources Science and Technology* 29.12 (2020).
- [43] J-P Boeuf. “A two-dimensional model of dc glow discharges”. In: *Journal of applied physics* 63.5 (1988).
- [44] Jannis Teunissen and Ute Ebert. “Simulating streamer discharges in 3D with the parallel adaptive Afivo framework”. In: *Journal of Physics D: Applied Physics* 50.47 (2017).
- [45] Jannis Teunissen and Ute Ebert. “Afivo: A Framework for Quadtree/Octree AMR with Shared-Memory Parallelization and Geometric Multigrid Methods”. In: *Computer Physics Communications* 233 (Dec. 2018).
- [46] Leonardo Dagum and Ramesh Menon. “OpenMP: an industry standard API for shared-memory programming”. In: *IEEE computational science and engineering* 5.1 (1998).
- [47] B Bagheri et al. “Comparison of Six Simulation Codes for Positive Streamers in Air”. In: *Plasma Sources Science and Technology* 27.9 (2018).
- [48] Xiaoran Li et al. “A computational study of steady and stagnating positive streamers in N₂-O₂ mixtures”. In: *Plasma Sources Science and Technology* 31.6 (2022).
- [49] Zhen Wang et al. “Quantitative modeling of streamer discharge branching in air”. In: *Plasma Sources Science and Technology* 32.8 (2023).

- [50] Zhen Wang et al. “A Comparison of Particle and Fluid Models for Positive Streamer Discharges in Air”. In: *Plasma Sources Science and Technology* 31.1 (2022).
- [51] Behnaz Bagheri and Jannis Teunissen. “The effect of the stochasticity of photoionization on 3D streamer simulations”. In: *Plasma Sources Science and Technology* 28.4 (2019).
- [52] Jannis Teunissen and Francesca Schiavello. “Geometric Multigrid Method for Solving Poisson’s Equation on Octree Grids with Irregular Boundaries”. In: *Computer Physics Communications* 286 (2023).
- [53] G. J. M. Hagelaar and L. C. Pitchford. “Solving the Boltzmann equation to obtain electron transport coefficients and rate coefficients for fluid models”. In: 14.4 (Oct. 2005).
- [54] Antonio Tejero-del-Caz et al. “The LisbOn KInetics Boltzmann solver”. In: *Plasma Sources Science and Technology* 28.4 (2019).
- [55] Tiago C Dias et al. “The LisbOn KInetics Monte Carlo solver”. In: *Computer Physics Communications* 282 (2023).
- [56] Mohamed Rabie and Christian M Franck. “METHES: A Monte Carlo collision code for the simulation of electron transport in low temperature plasmas”. In: *Computer Physics Communications* 203 (2016).
- [57] *LXCat*, www.lxcat.net.
- [58] Fumiyoshi Tochikubo and Hideyuki Arai. “Numerical simulation of streamer propagation and radical reactions in positive corona discharge in N_2/NO and $N_2/O_2/NO$ ”. In: *Japanese journal of applied physics* 41.2R (2002).
- [59] Randall J LeVeque. *Finite volume methods for hyperbolic problems*. Vol. 31. Cambridge university press, 2002.
- [60] Barry Koren. *A robust upwind discretization method for advection, diffusion and source terms*. Vol. 45. Centrum voor Wiskunde en Informatica Amsterdam, 1993.
- [61] Ulrich Trottenberg et al. *Multigrid*. Elsevier, 2000.
- [62] Uri M Ascher and Linda R Petzold. *Computer methods for ordinary differential equations and differential-algebraic equations*. Vol. 61. Siam, 1998.
- [63] Richard Courant et al. “On the partial difference equations of mathematical physics”. In: *IBM journal of Research and Development* 11.2 (1967).
- [64] H Malla et al. “Double-pulse streamer simulations for varying interpulse times in air”. In: *Plasma Sources Science and Technology* 32.9 (2023).
- [65] PA Vitello et al. “Simulation of negative-streamer dynamics in nitrogen”. In: *Physical Review E* 49.6 (1994).
- [66] David B. Graves. “Low temperature plasma biomedicine: A tutorial review”. In: *Physics of Plasmas* 21.8 (2014). Publisher: American Institute of Physics.
- [67] Mounir Laroussi. “From Killing Bacteria to Destroying Cancer Cells: 20 Years of Plasma Medicine”. In: *Plasma Processes and Polymers* 11.12 (2014).
- [68] Pietro Ranieri et al. “Plasma agriculture: Review from the perspective of the plant and its ecosystem”. In: *Plasma Processes and Polymers* 18.1 (2021).

-
- [69] Ladislav Bárδος and Hana Baránková. “Cold atmospheric plasma: Sources, processes, and applications”. In: *Thin solid films* 518.23 (2010).
- [70] Svetlana M Starikovskaia. “Plasma assisted ignition and combustion”. In: *Journal of Physics D: Applied Physics* 39.16 (2006).
- [71] S Nijdam et al. “Investigation of positive streamers by double-pulse experiments, effects of repetition rate and gas mixture”. en. In: *Plasma Sources Sci. Technol.* 23.2 (2014).
- [72] Yuan Li et al. “Positive double-pulse streamers: how pulse-to-pulse delay influences initiation and propagation of subsequent discharges”. In: *Plasma Sources Science and Technology* 27.12 (2018).
- [73] S Mirpour et al. “Distribution of inception times in repetitive pulsed discharges in synthetic air”. In: *Plasma Sources Science and Technology* 29.11 (2020).
- [74] David Z Pai et al. “Transitions between corona, glow, and spark regimes of nanosecond repetitively pulsed discharges in air at atmospheric pressure”. In: *Journal of Applied Physics* 107.9 (2010).
- [75] Fabien Tholin and Anne Bourdon. “Simulation of the stable ‘quasi-periodic’ glow regime of a nanosecond repetitively pulsed discharge in air at atmospheric pressure”. In: *Plasma Sources Science and Technology* 22.4 (2013).
- [76] XinPei Lu and Kostya Ostrikov. “Guided ionization waves: The physics of repeatability”. In: *Applied Physics Reviews* 5.3 (2018).
- [77] L Chang et al. “The effect of seed electrons on the repeatability of atmospheric pressure plasma plume propagation. II. Modeling”. In: *Physics of Plasmas* 23.12 (2016).
- [78] Natalia Yu Babaeva et al. “Evolution of ionization waves in a multi-pulsed plasma jet: the role of memory charges”. In: *Plasma Science and Technology* (2022).
- [79] H Höft et al. “The bidirectional character of O₂ concentration in pulsed dielectric barrier discharges in O₂/N₂ gas mixtures”. In: *Journal of Physics D: Applied Physics* 47.45 (2014).
- [80] H Höft et al. “Breakdown characteristics in pulsed-driven dielectric barrier discharges: influence of the pre-breakdown phase due to volume memory effects”. In: *Journal of Physics D: Applied Physics* 47.46 (2014).
- [81] Z Zhao et al. “Volume and Surface Memory Effects on Evolution of Streamer Dynamics along Gas/Solid Interface in High-Pressure Nitrogen under Long-Term Repetitive Nanosecond Pulses”. In: *Plasma Sources Science and Technology* 29.1 (2020).
- [82] Zheng Zhao et al. “Streamer Dynamics and Periodical Discharge Regime Transitions under Repetitive Nanosecond Pulses with Airflow”. In: *Plasma Sources Science and Technology* 32.1 (2023).
- [83] Zheng Zhao and Jiangtao Li. “Repetitively Pulsed Gas Discharges: Memory Effect and Discharge Mode Transition”. In: *High Voltage* 5.5 (2020).
- [84] S. Nijdam et al. “Streamer discharges can move perpendicularly to the electric field”. In: *New J. Phys.* 16.10 (2014).

- [85] S Nijdam et al. “The Role of Free Electrons in the Guiding of Positive Streamers”. In: *Plasma Sources Science and Technology* 25.4 (2016).
- [86] GV Naidis. “Modelling of plasma bullet propagation along a helium jet in ambient air”. In: *Journal of Physics D: Applied Physics* 44.21 (2011).
- [87] Xiaoran Li et al. “Comparing simulations and experiments of positive streamers in air: steps toward model validation”. In: *Plasma Sources Science and Technology* 30.9 (2021).
- [88] *Phelps database, www.lxcat.net, retrieved on August 19, 2021.*
- [89] Baohong Guo and Jannis Teunissen. “A Computational Study on the Energy Efficiency of Species Production by Single-Pulse Streamers in Air”. In: *Plasma Sources Science and Technology* 32.2 (2023).
- [90] I A Kossyi et al. “Kinetic scheme of the non-equilibrium discharge in nitrogen-oxygen mixtures”. In: *Plasma Sources Sci. Technol.* 1.3 (1992).
- [91] Ryo Ono and Atsushi Komuro. “Generation of the Single-Filament Pulsed Positive Streamer Discharge in Atmospheric-Pressure Air and Its Comparison with Two-Dimensional Simulation”. In: *Journal of Physics D: Applied Physics* 53.3 (2020).
- [92] S. Pancheshnyi et al. “Development of a cathode-directed streamer discharge in air at different pressures: Experiment and comparison with direct numerical simulation”. In: *Phys. Rev. E* 71.1 ().
- [93] Eric W Hansen and Phaih-Lan Law. “Recursive methods for computing the Abel transform and its inverse”. In: *JOSA A* 2.4 (1985).
- [94] N L Aleksandrov and E M Bazelyan. “Ionization processes in spark discharge plasmas”. In: *Plasma Sources Science and Technology* 8.2 (1999).
- [95] Sergey Pancheshnyi. “Effective ionization rate in nitrogen–oxygen mixtures”. In: *Journal of Physics D: Applied Physics* 46.15 (2013).
- [96] *BOLSIG+ (Linux)*. Dec. 2019.
- [97] Igor Odrobina and Mirko Černák. “Numerical Simulation of Streamer–Cathode Interaction”. In: *Journal of Applied Physics* 78.6 (1995).
- [98] Natalia Yu Babaeva. “Hot Secondary Electrons in Dielectric Barrier Discharges Treated with Monte Carlo Simulation: Implication for Fluxes to Surfaces”. In: *Plasma Sources Science and Technology* 24.3 (2015).
- [99] Wen Yan et al. “Two-Dimensional Modeling of the Cathode Sheath Formation during the Streamer–Cathode Interaction”. In: *Physics of Plasmas* 21.1 (2014).
- [100] Aleksandar P Jovanović et al. “Streamer–surface interaction in an atmospheric pressure dielectric barrier discharge in argon”. In: *Plasma Sources Science and Technology* 31.4 (2022).
- [101] Sander Nijdam et al. “The Physics of Streamer Discharge Phenomena”. In: *Plasma Sources Science and Technology* 29.10 (2020).
- [102] Eduard M Bazelyan and Yuri P Raizer. *Spark discharge*. CRC press, 1997.
- [103] I. Gallimberti. “The mechanism of the long spark formation”. In: *Journal de Physique Colloques*, 40.C7 (1979).

-
- [104] Alejandro Malagón-Romero and Alejandro Luque. “Spontaneous emergence of space stems ahead of negative leaders in lightning and long sparks”. In: *Geophysical Research Letters* 46.7 (2019).
- [105] Leonid Babich et al. “General processes responsible for the space leader birth in streamer coronas of negative leaders”. In: *Plasma Research Express* 3.4 (2021).
- [106] F. J. Gordillo-Vázquez and F. J. Pérez-Invernón. “A review of the impact of transient luminous events on the atmospheric chemistry: Past, present, and future”. In: *Atmospheric Research* 252 (2021).
- [107] R. C. Franz et al. “Television Image of a Large Upward Electrical Discharge Above a Thunderstorm System”. In: *Science* 249 (1990).
- [108] H. C. Stenbaek-Nielsen and M. G. McHarg. “High time-resolution sprite imaging: observations and implications”. In: *J. Phys. D* 41.23 (2008).
- [109] HC Stenbaek-Nielsen et al. “High-speed observations of sprite streamers”. In: *Surveys in Geophysics* 34 (2013).
- [110] E. M. Wescott et al. “Preliminary results from the Sprites94 aircraft campaign: 2. Blue jets”. In: *Geophys. Res. Lett.* 22 (1995).
- [111] Y. P. Raizer et al. “Streamer- and leader-like processes in the upper atmosphere: Models of red sprites and blue jets”. In: *J. Geophys. Res. (Space Phys)* 115 (2010), A00E42.
- [112] N. A. Popov et al. “Similarity analysis of the streamer zone of Blue jets”. In: *J. Atm. Sol.-Terr. Phys.* 147 (2016).
- [113] W. Rison et al. “Observations of narrow bipolar events reveal how lightning is initiated in thunderstorms”. In: *Nature Communications* 7 (2016).
- [114] Ningyu Liu et al. “Understanding the Radio Spectrum of Thunderstorm Narrow Bipolar Events”. In: *Journal of Geophysical Research (Atmospheres)* 124.10134 (2019).
- [115] Dongshuai Li et al. “Blue Flashes as Counterparts to Narrow Bipolar Events: The Optical Signal of Shallow In-Cloud Discharges”. In: *J. Geophys. Res. (Atmos.)* 126.13 (2021).
- [116] S. Soler et al. “Blue Optical Observations of Narrow Bipolar Events by ASIM Suggest Corona Streamer Activity in Thunderstorms”. In: *Journal of Geophysical Research (Atmospheres)* 125.16 (2020).
- [117] Gregory Fridman et al. “Applied Plasma Medicine”. In: *Plasma Processes and Polymers* 5.6 (2008).
- [118] David B. Graves. “Low Temperature Plasma Biomedicine: A Tutorial Review”. In: *Physics of Plasmas* 21.8 (2014).
- [119] L. Bárdos and H. Baránková. “Cold Atmospheric Plasma: Sources, Processes, and Applications”. In: *Thin Solid Films* 518.23 (2010).
- [120] Hyun-Ha Kim. “Nonthermal Plasma Processing for Air-Pollution Control: A Historical Review, Current Issues, and Future Prospects”. In: *Plasma Processes and Polymers* 1.2 (2004).

- [121] E J M van Heesch et al. “Evaluation of Pulsed Streamer Corona Experiments to Determine the O^* Radical Yield”. In: *Journal of Physics D: Applied Physics* 41.23 (2008), p. 234015.
- [122] Pankaj Attri et al. “Plasma agriculture from laboratory to farm: A review”. In: *Processes* 8.8 (2020).
- [123] S M Starikovskaia. “Plasma-Assisted Ignition and Combustion: Nanosecond Discharges and Development of Kinetic Mechanisms”. In: *Journal of Physics D: Applied Physics* 47.35 (Sept. 2014).
- [124] N A Popov. “Kinetics of Plasma-Assisted Combustion: Effect of Non-Equilibrium Excitation on the Ignition and Oxidation of Combustible Mixtures”. In: *Plasma Sources Science and Technology* 25.4 (Aug. 2016).
- [125] Yiguang Ju and Wenting Sun. “Plasma assisted combustion: Dynamics and chemistry”. In: *Progress in Energy and Combustion Science* 48 (2015).
- [126] Mengzhe Li et al. “Advances in plasma-assisted ignition and combustion for combustors of aerospace engines”. In: *Aerospace Science and Technology* 117 (2021).
- [127] Eric Moreau. “Airflow control by non-thermal plasma actuators”. In: *Journal of physics D: applied physics* 40.3 (2007).
- [128] Thomas C Corke et al. “Dielectric barrier discharge plasma actuators for flow control”. In: *Annual review of fluid mechanics* 42 (2010).
- [129] S Nijdam et al. “Investigation of positive streamers by double-pulse experiments, effects of repetition rate and gas mixture”. In: *Plasma Sources Science and Technology* 23.2 (2014).
- [130] Baohong Guo et al. “3D modeling of positive streamers in air with inhomogeneous density”. In: *Plasma Sources Science and Technology* 32.9 (2023).
- [131] Behnaz Bagheri et al. “Simulation of Positive Streamers in CO_2 and in Air: The Role of Photoionization or Other Electron Sources”. In: *Plasma Sources Science and Technology* 29.12 (2020).
- [132] Dennis Bouwman et al. “3D Particle Simulations of Positive Air–Methane Streamers for Combustion”. In: *Plasma Sources Science and Technology* 31.4 (2022), p. 045023.
- [133] RF Griffiths and CT Phelps. “The effects of air pressure and water vapour content on the propagation of positive corona streamers, and their implications to lightning initiation”. In: *Quarterly Journal of the Royal Meteorological Society* 102.432 (1976).
- [134] Les Renardières group. “Positive discharges in long air gaps at Les Renardières, 1975 results and conclusions”. In: *Elektra* 53 (1978).
- [135] Les Renardières group. “Negative discharges in long air gaps at Les Renardières”. In: *Elektra* 74 (1978).
- [136] Alejandro Malagón-Romero and Alejandro Luque. “Streamer Propagation in Humid Air”. In: *Plasma Sources Science and Technology* 31.10 (2022).
- [137] A Yu Starikovskiy et al. “The Influence of Humidity on Positive Streamer Propagation in Long Air Gap”. In: *Plasma Sources Science and Technology* 31.11 (2022).

-
- [138] Phelps database (N₂, O₂) www.lxcat.net (retrieved 13 October 2023).
- [139] A. V. Phelps and L. C. Pitchford. “Anisotropic scattering of electrons by N₂ and its effect on electron transport”. In: *Physical Review A* 31.5 (1985).
- [140] S. A. Lawton and A. V. Phelps. “Excitation of the b¹Σ_g⁺ State of O₂ by Low Energy Electrons”. In: *The Journal of Chemical Physics* 69.3 (1978).
- [141] Maik Budde et al. “Electron-Neutral Collision Cross Sections for H₂O: I. Complete and Consistent Set”. In: *Journal of Physics D: Applied Physics* 55.44 (2022).
- [142] J. De Urquijo et al. “Electron Drift Velocities in He and Water Mixtures: Measurements and an Assessment of the Water Vapour Cross-Section Sets”. In: *The Journal of Chemical Physics* 141.1 (2014).
- [143] M. Yousfi and M. D. Benabdessadok. “Boltzmann Equation Analysis of Electron-Molecule Collision Cross Sections in Water Vapor and Ammonia”. In: *Journal of Applied Physics* 80.12 (1996).
- [144] K. F. Ness et al. “Transport Coefficients and Cross Sections for Electrons in Water Vapour: Comparison of Cross Section Sets Using an Improved Boltzmann Equation Solution”. In: *The Journal of Chemical Physics* 136.2 (2012).
- [145] Satoru Kawaguchi et al. “Electron Transport Analysis in Water Vapor”. In: *Japanese Journal of Applied Physics* 55.7S2 (2016).
- [146] Yukikazu Itikawa and Nigel Mason. “Cross Sections for Electron Collisions with Water Molecules”. In: *Journal of Physical and Chemical Reference Data* 34.1 (2005).
- [147] “LXCat: An Open-Access, Web-Based Platform for Data Needed for Modeling Low Temperature Plasmas”. In: *Plasma Processes and Polymers* 14.1-2 (2017), p. 1600098.
- [148] Morgan database (H₂O) www.lxcat.net (retrieved 13 October 2023).
- [149] Phelps database (H₂O) www.lxcat.net (retrieved 13 October 2023).
- [150] W.L. Morgan and B.M. Penetrante. “ELENDF: A Time-Dependent Boltzmann Solver for Partially Ionized Plasmas”. In: *Computer Physics Communications* 58.1-2 (1990).
- [151] Trinit database (H₂O) www.lxcat.net (retrieved 13 October 2023).
- [152] N.A. Dyatko et al. *EEDF: the software package for calculations of the electron energy distribution function in gas mixtures*. <http://www.lxcat.net/software/EEDF/>. Accessed: 2024-01-30. 2011.
- [153] Itikawa database (H₂O) www.lxcat.net (retrieved 13 October 2023).
- [154] Mi-Young Song et al. “Cross Sections for Electron Collisions with H₂O”. In: *Journal of Physical and Chemical Reference Data* 50.2 (2021).
- [155] G J M Hagelaar and L C Pitchford. “Solving the Boltzmann Equation to Obtain Electron Transport Coefficients and Rate Coefficients for Fluid Models”. In: *Plasma Sources Science and Technology* 14.4 (2005).
- [156] J Stephens et al. “Photoionization Capable, Extreme and Vacuum Ultraviolet Emission in Developing Low Temperature Plasmas in Air”. In: *Plasma Sources Science and Technology* 25.2 (2016).

- [157] B Bagheri and J Teunissen. “The Effect of the Stochasticity of Photoionization on 3D Streamer Simulations”. In: *Plasma Sources Science and Technology* 28.4 (2019).
- [158] Zhen Wang et al. “Quantitative Modeling of Streamer Discharge Branching in Air”. In: *Plasma Sources Science and Technology* 32.8 (2023).
- [159] G V Naidis. “On Photoionization Produced by Discharges in Air”. In: *Plasma Sources Science and Technology* 15.2 (2006).
- [160] Märt Aints et al. “Absorption of Photo-Ionizing Radiation of Corona Discharges in Air”. In: *Plasma Processes and Polymers* 5.7 (2008).
- [161] A Bourdon et al. “Efficient Models for Photoionization Produced by Non-Thermal Gas Discharges in Air Based on Radiative Transfer and the Helmholtz Equations”. In: *Plasma Sources Science and Technology* 16.3 (2007).
- [162] Alejandro Luque et al. “Photoionization in Negative Streamers: Fast Computations and Two Propagation Modes”. In: *Applied Physics Letters* 90.8 (Feb. 2007).
- [163] Miles M Turner. “Uncertainty and Error in Complex Plasma Chemistry Models”. In: *Plasma Sources Science and Technology* 24.3 (2015).
- [164] Miles M Turner. “Uncertainty and Sensitivity Analysis in Complex Plasma Chemistry Models”. In: *Plasma Sources Science and Technology* 25.1 (2016).
- [165] S. V. Pancheshnyi et al. “Discharge Dynamics and the Production of Active Particles in a Cathode-Directed Streamer”. In: *Plasma Physics Reports* 26.12 (2000).
- [166] Lipeng Liu and Marley Becerra. “Gas Heating Dynamics during Leader Inception in Long Air Gaps at Atmospheric Pressure”. In: *Journal of Physics D: Applied Physics* 50.34 (2017).
- [167] L. Wayne Sieck et al. “Chemical Kinetics Database and Predictive Schemes for Humid Air Plasma Chemistry. Part I: Positive Ion-Molecule Reactions”. In: *Plasma Chemistry and Plasma Processing* 20.2 (2000).
- [168] John T. Herron and David S. Green. “Chemical Kinetics Database and Predictive Schemes for Nonthermal Humid Air Plasma Chemistry. Part II. Neutral Species Reactions”. In: *Plasma Chemistry and Plasma Processing* 21.3 (2001).
- [169] R. Johnsen. “Electron-Temperature Dependence of the Recombination of $\text{H}_3\text{O}^+(\text{H}_2\text{O})_n$ Ions with Electrons”. In: *The Journal of Chemical Physics* 98.7 (1993).
- [170] Atsushi Komuro et al. “Behaviour of OH Radicals in an Atmospheric-Pressure Streamer Discharge Studied by Two-Dimensional Numerical Simulation”. In: *Journal of Physics D: Applied Physics* 46.17 (2013).
- [171] Atsushi Komuro et al. “Simulation of Pulsed Positive Streamer Discharges in Air at High Temperatures”. In: *Plasma Sources Science and Technology* 27.10 (2018).
- [172] Francesca Campolongo et al. “An Effective Screening Design for Sensitivity Analysis of Large Models”. In: *Environmental Modelling & Software* 22.10 (2007).
- [173] Antonin Berthelot and Annemie Bogaerts. “Modeling of CO_2 Plasma: Effect of Uncertainties in the Plasma Chemistry”. In: *Plasma Sources Science and Technology* 26.11 (2017).

-
- [174] Loann Terraz et al. "Sensitivity Analysis in Plasma Chemistry: Application to Oxygen Cold Plasmas and the LoKI Simulation Tool". In: *The Journal of Physical Chemistry A* 124.22 (2020).
- [175] Zhenyu Wei et al. "The Influence of Individual Evaluation of Electron-impact Ionization, Attachment, and Photoionization Rates on Positive Streamer Propagation". In: *Plasma Processes and Polymers* (2023).
- [176] N L Aleksandrov and E M Bazelyan. "Ionization Processes in Spark Discharge Plasmas". In: *Plasma Sources Science and Technology* 8.2 (1999).
- [177] S. Pancheshnyi et al. "Development of a Cathode-Directed Streamer Discharge in Air at Different Pressures: Experiment and Comparison with Direct Numerical Simulation". In: *Physical Review E* 71.1 (2005).
- [178] O. Eichwald et al. "Coupling of Chemical Kinetics, Gas Dynamics, and Charged Particle Kinetics Models for the Analysis of NO Reduction from Flue Gases". In: *Journal of Applied Physics* 82.10 (1997).
- [179] Victor P Pasko et al. "Spatial structure of sprites". In: *Geophysical Research Letters* 25.12 (1998).
- [180] Ningyu Liu and Victor P Pasko. "Effects of photoionization on propagation and branching of positive and negative streamers in sprites". In: *Journal of Geophysical Research: Space Physics* 109.A4 (2004).
- [181] E Marode et al. "A model of the streamer-induced spark formation based on neutral dynamics". In: *Journal of Applied Physics* 50.1 (1979).
- [182] GV Naidis. "Simulation of streamer-to-spark transition in short non-uniform air gaps". In: *Journal of physics D: Applied physics* 32.20 (1999).
- [183] Caitano L Da Silva and Victor P Pasko. "Dynamics of streamer-to-leader transition at reduced air densities and its implications for propagation of lightning leaders and gigantic jets". In: *Journal of Geophysical Research: Atmospheres* 118.24 (2013).
- [184] M Seeger et al. "Streamer parameters and breakdown in CO₂". In: *Journal of Physics D: Applied Physics* 50.1 (2016).
- [185] Asami Hatamoto et al. "Surface temperature characterization of dielectric barrier discharge plasma actuator in quiescent air". In: *Journal of Physics D: Applied Physics* 56.15 (2023).
- [186] NA Popov. "Formation and development of a leader channel in air". In: *Plasma Physics Reports* 29 (2003).
- [187] S Nijdam et al. "Probing background ionization: positive streamers with varying pulse repetition rate and with a radioactive admixture". In: *Journal of Physics D: Applied Physics* 44.45 (2011).
- [188] Steven Adams et al. "The effect of inter-pulse coupling on gas temperature in nanosecond-pulsed high-frequency discharges". In: *Journal of Physics D: Applied Physics* 52.35 (2019).
- [189] Ravi Patel et al. "On pulse-to-pulse coupling in low-temperature filamentary plasma-assisted ignition in methane-air flows". In: *Plasma Sources Science and Technology* 32.6 (2023).

- [190] Benjamin Harris and Erik Wagenaars. “The influence of pulse repetition frequency on reactive oxygen species production in pulsed He+H₂O plasmas at atmospheric pressure”. In: *Journal of Applied Physics* 134.10 (2023).
- [191] Alexander Kurganov and Eitan Tadmor. “New high-resolution central schemes for nonlinear conservation laws and convection–diffusion equations”. In: *Journal of computational physics* 160.1 (2000).
- [192] NA Popov. “Investigation of the mechanism for rapid heating of nitrogen and air in gas discharges”. In: *Plasma physics reports* 27 (2001).
- [193] NA Popov. “Fast gas heating in a nitrogen–oxygen discharge plasma: I. Kinetic mechanism”. In: *Journal of Physics D: Applied Physics* 44.28 (2011).
- [194] Atsushi Komuro and Ryo Ono. “Two-dimensional simulation of fast gas heating in an atmospheric pressure streamer discharge and humidity effects”. In: *Journal of Physics D: Applied Physics* 47.15 (2014).
- [195] A Agnihotri et al. “Modeling heat dominated electric breakdown in air, with adaptivity to electron or ion time scales”. In: *Plasma Sources Science and Technology* 26.9 (2017).
- [196] She Chen et al. “Transition mechanism of negative DC corona modes in atmospheric air: from Trichel pulses to pulseless glow”. In: *Plasma Sources Science and Technology* 28.5 (2019).
- [197] Lipeng Liu and Marley Becerra. “Gas heating dynamics during leader inception in long air gaps at atmospheric pressure”. In: *Journal of Physics D: Applied Physics* 50.34 (2017).
- [198] Jeremy A Rioussset et al. “Air-density-dependent model for analysis of air heating associated with streamers, leaders, and transient luminous events”. In: *Journal of Geophysical Research: Space Physics* 115.A12 (2010).
- [199] Samira Kacem et al. “Simulation of expansion of thermal shock and pressure waves induced by a streamer dynamics in positive dc corona discharges”. In: *IEEE Transactions on Plasma Science* 41.4 (2013).
- [200] Ryo Ono and Tetsuji Oda. “Visualization of streamer channels and shock waves generated by positive pulsed corona discharge using laser schlieren method”. In: *Japanese Journal of Applied Physics* 43.1R (2004).
- [201] Atsushi Komuro et al. “Gas-heating phenomenon in a nanosecond pulse discharge in atmospheric-pressure air and its application for high-speed flow control”. In: *Plasma Sources Science and Technology* 27.10 (2018).
- [202] Hemaditya Malla et al. “Calculating radio emissions of positive streamer phenomena using 3D simulations”. In: *arXiv preprint arXiv:2404.09772* (2024).
- [203] Danyal Petersen and William Beasley. “Microwave radio emissions of negative cloud-to-ground lightning flashes”. In: *Atmospheric research* 135 (2014).
- [204] Vladimir A Rakov and Martin A Uman. *Lightning: physics and effects*. Cambridge university press, 2003.
- [205] BM Hare et al. “LOFAR lightning imaging: Mapping lightning with nanosecond precision”. In: *Journal of Geophysical Research: Atmospheres* 123.5 (2018).
- [206] Ningyu Y Liu et al. “LOFAR observations of lightning initial breakdown pulses”. In: *Geophysical Research Letters* 49.6 (2022).

-
- [207] Marx Brook and N Kitagawa. “Radiation from lightning discharges in the frequency range 400 to 1000 Mc/s”. In: *Journal of Geophysical Research* 69.12 (1964).
- [208] Feng Shi et al. “Properties of relatively long streamers initiated from an isolated hydrometeor”. In: *Journal of Geophysical Research: Atmospheres* 121.12 (2016).
- [209] Martin A Uman et al. “The electromagnetic radiation from a finite antenna”. In: *American Journal of Physics* 43.1 (1975).
- [210] Alejandro Luque. “Radio frequency electromagnetic radiation from streamer collisions”. In: *Journal of Geophysical Research: Atmospheres* 122.19 (2017).
- [211] Feng Shi et al. “VHF and UHF electromagnetic radiation produced by streamers in lightning”. In: *Geophysical Research Letters* 46.1 (2019).
- [212] Jacob Koile et al. “Radio frequency emissions from streamer collisions in sub-breakdown fields”. In: *Geophysical Research Letters* 48.24 (2021).
- [213] MB Garnung et al. “Hf-vhf electromagnetic emissions from collisions of sprite streamers”. In: *Journal of Geophysical Research: Space Physics* 126.6 (2021).
- [214] EV Parkevich et al. “Streamer formation processes trigger intense x-ray and high-frequency radio emissions in a high-voltage discharge”. In: *Physical Review E* 105.5 (2022).
- [215] EV Parkevich et al. “Electromagnetic emissions in the MHz and GHz frequency ranges driven by the streamer formation processes”. In: *Physical Review E* 106.4 (2022).
- [216] ME Gushchin et al. “Nanosecond electromagnetic pulses generated by electric discharges: Observation with clouds of charged water droplets and implications for lightning”. In: *Geophysical Research Letters* 48.7 (2021).
- [217] Yunjiao Pu et al. “VHF Radio Spectrum of a Positive Leader and Implications for Electric Fields”. In: *Geophysical Research Letters* 48.11 (2021).
- [218] Yunjiao Pu et al. “Quantification of Electric Fields in Fast Breakdown During Lightning Initiation From VHF-UHF Power Spectra”. In: *Geophysical Research Letters* 49.5 (2022).
- [219] O. Scholten et al. “Small-Scale Discharges Observed Near the Top of a Thunderstorm”. In: *Geophysical Research Letters* 50.8 (2023).
- [220] Oleg D Jefimenko. *Electricity and Magnetism: An Introduction to the Theory of Electric and Magnetic Fields*. Appleton-Century-Crofts, 1966.
- [221] David J Griffiths. *Introduction to electrodynamics, 4th Edition*. 2017.
- [222] Ningyu Liu et al. “Electromagnetic Radiation Spectrum of a Composite System”. In: *Physical Review Letters* 125.2 (2020).
- [223] Ervin Sejdic et al. “Quantitative performance analysis of scalogram as instantaneous frequency estimator”. In: *IEEE Transactions on Signal Processing* 56.8 (2008).
- [224] Christopher Torrence and Gilbert P Compo. “A practical guide to wavelet analysis”. In: *Bulletin of the American Meteorological society* 79.1 (1998).
- [225] Gregory Lee et al. “PyWavelets: A Python package for wavelet analysis”. In: *Journal of Open Source Software* 4.36 (2019).

- [226] Mallat Stephane. *A wavelet tour of signal processing*. 1999.
- [227] S Nijdam et al. “Reconnection and Merging of Positive Streamers in Air”. In: *Journal of Physics D: Applied Physics* 42.4 (2009), p. 045201.
- [228] Zhen Wang et al. “Quantitative prediction of streamer discharge branching in air”. In: *Plasma Sources Science and Technology* 32.8 (2023).
- [229] Siebe Dijcks et al. “Imaging and reconstruction of positive streamer discharge tree structures”. en. In: *Plasma Sources Science and Technology* 32.4 (2023).
- [230] Dennis Bouwman et al. “Estimating the properties of single positive air streamers from measurable parameters”. In: *Plasma Sources Science and Technology* 32.7 (2023).

Curriculum Vitae

Hemaditya Malla was born on February 4, 1996 in Visakhapatnam, India. After finishing his high school education in mathematics, physics and chemistry (MPC) in the same city, he moved to Goa, India in 2013 to start his bachelor study in Mechanical Engineering. Four years later, in 2017, he obtained his bachelors degree and moved to Eindhoven in the Netherlands to start his masters study. In 2019, he obtained his masters degree in Industrial and applied mathematics at the Eindhoven university of Technology. Later in 2019, he started his PhD on streamer discharge modeling in the Multiscale Dynamics group at Centrum Wiskunde & Informatica, Amsterdam. The results from his PhD project are presented in this dissertation

Selected journal publications

- [1] **H. Malla**, A. Martinez, U. Ebert, and J. Teunissen. Double-pulse streamer simulations for vaying interpulse times in air. *Plasma Sources Sci. Technol.*, Volume 32 (9) 095006, 2023.
- [2] **Hemaditya Malla**, Yihao Guo, Brian.M. Hare, Steven Cummer, Alejandro Malagón-Romero, Ute Ebert, Sander Nijdam, Jannis Teunissen. Calculating radio emissions of positive streamer phenomena using 3D simulations. *Submitted to the Journal of Geophysical Research– Atmospheres*
- [3] B. Guo, **H. Malla**, A. Malagon, U. Ebert and J. Teunissen. Streamer discharge simulations in humid air: uncertainty in input data and sensitivity analysis. *Under preparation to submit to Plasma Sources Sci. Technol.*

Selected conference contributions

- [1] Poster titled, "*Double pulse streamer simulations*" at International Conference on plasmas in ionized gases, July 31, 2023, The Netherlands. **Awarded the best poster prize.**
- [2] Talk titled, "*Streamer simulations for varying humidity in air*" at the International Conference in Plasma Medicine, March 16, 2022, The Netherlands.
- [3] Poster titled, "*Challenges in simulating electrical discharges*" at the Dutch-Flemish society for Scientific Computing Winter meeting, October 2021, The Netherlands.